Friedrich-Alexander-Universität Erlangen-Nürnberg

Institute for Micro- and Nanostructure Research

Epitaxy and Solid-State Dewetting of Au thin films on polar and nonpolar metal-oxide surfaces

Department of Materials Science and Engineering

Institute of Micro- and Nanostructure Research

Prof. Dr. rer. nat. habil. Erdmann Spiecker

Master Thesis

by

Michael Landes

Supervisor: M.Sc. Martin Dierner

Erlangen, 28.03.2022

Abstract

In this thesis, the dewetting behaviour and texture evolution of thin Au films on metal-oxide substrates are investigated. Sapphire wafers have a non-polar surface, because the charged ions are compensated without forming a dipole moment. Au films deposited on (0001) sapphire are studied regarding the influence of the ambient atmosphere on solid-state dewetting and texture evolution during rapid thermal annealing. Samples that are annealed in vacuum and a hydrogen/argon mixture show slower dewetting than in nitrogen, but this is attributed to the heat transfer in the rapid thermal annealing furnace. After annealing the films develope a pronounced (111) out-of plane texture, but are not in an in-plane orientation relation to the sapphire.
Crystals with a wurtzit lattice have two polar surfaces, in the case of zinc oxide (ZnO) one with Zn termination at the (0001) side and one with O termination at the $(000\bar{1})$ side. Gold thin films deposited on these polar ZnO planes show a strong influence on epitaxial grain growth and solid-state dewetting depending on the polarity. On the oxygen side the Au films dewett much faster than on the Zn side. The different dewetting rates can be explained by a larger binding energy of Au to the zinc terminated surface, which lowers the Au/Zn-ZnO interface energy and makes it more resistant to dewetting than the weakly bound oxygen side. The preferred orientation of Au grains on both ZnO sides after deposition at room temperature is $Au(111)[110]|ZnO(0001)[11\bar{2}0]$ (OR2) which has a high misfit, but can relax through misfit dislocations at the interface. During annealing at 800 °C and above the Au film on the zinc side forms large epitaxial grains with an $Au(111)[110]|ZnO(0001)[10\bar{1}0]$ orientation (OR1). The change of the orientation relation is likely aided by reconstruction at the Au/Zn-ZnO interface that is observed in high resolution scanning transmission electron microscopy (HRSTEM).

Contents

List of Figures

List of Abbreviations and Symbols

α	Thermal expansion factor
ΔT	Temperature difference
δ	Lattice misfit of a film and substrate
δ_{CSL}	Misfit of the CSL super cell
$\frac{dr}{dt}$	Grain growth rate
γ_{gb}	Grain boundary energy
γ_i	Interface energy
γ_s	Surface energy
λ	Wavelength
a	Lattice constant
c	Lattice constant
hkl	Miller indices
AFM	Atomic force microscope
Au	Gold
BSE	Back scattered electrons
CSL	Coincidence site lattice
$EBSD$	Electron back scatter detection
FIB	Focused ion beam
$HRSTEM$	High resolution scanning transmission electron microscopy
IPF	Inverse pole figure
Ni	Nickel
$O-ZnO$	The zinc oxide substrates with a $(000\bar{1})$ orientation

$OR1$	The orientation relation $[110]_{film}(111)_{film}\|\|[10\bar{1}0]_{Substrate}(0001)_{Substrate}$
$OR2$	The orientation relation $[110]_{film}(111)_{film}\|\|[11\bar{2}0]_{Substrate}(0001)_{Substrate}$
PF	Pole figure
PVD	Physical vapor deposition
RTA	Rapid thermal annealing
$SAED$	Selected area electron diffraction
SE	Secondary electrons
SEM	Scanning electron microscopy
SSD	Solid state dewetting
TEM	Transmission electron microscopy
XRD	X-ray diffraction
$Zn-ZnO$	The zinc oxide substrates with a (0001) orientation
ZnO	Zinc oxide

Chapter 1

Introduction

The combination of metals and metal oxides is widely used in many technological applications, reaching from aero-space components to catalysis and electronics [1]. An important aspect for these materials is the resistance of the metal to solid-state dewetting and if their is an epitaxial relationship. Solid-state dewetting is the name for the agglomeration of a film into particles at a temperature below the respective melting point [2]. It is relevant for metal films with a thickness at the nanometer scale and can lead to the failure of devices, but can also be used to produce novel nanostructures. Epitaxy means that a substrate has an influence on the orientation of a material growing on it. Many technological process use this phenomenon, because it allows the growth of well defined crystalline layers with improved properties. Most epitaxy is applied to semiconductors, but the process usually needs a low lattice mismatch between the two materials and can therefore also apply to metal oxides and metals [3].
Among the most researched metal oxides are likely sapphire and zinc oxide. They are both part of the hexagonal crystal family, but their c-plane surfaces are fundamentally different. In zinc oxide the charges of anions and cations result in a polar surface, while sapphire is non polar. The polar nature of zinc oxide is known to affect some properties of the material, but the influence on solid-state dewetting and gold films at elevated temperatures is not well studied.
In this thesis thin gold films on the (0001) surface of sapphire and the (0001) and $(000\bar{1})$ surfaces of ZnO are created by electron beam physical vapor deposition and heated in a rapid thermal annealing furnace. The orientation and therefore the polarity of the ZnO substrates was confirmed by convergent beam electron diffraction and HRSTEM. Further characterization of as-deposited and annealed samples is done with scanning electron microscopy and transmission electron microscopy. For the observation of the dewetting rate simple SEM imaging is sufficient. Quantitative texture analysis is determined by electron back scatter diffraction, which scans a sample area and gives a map with the orientation at each point and from this grain and particle orientation is available. For the two most common orientation relations of Au and ZnO high resolution STEM is used to further study the interface in cross-sections to reveal the atomic structure.

Chapter 2

Fundamentals

2.1 Metal-Ceramic Interfaces

Metals are usually ductile, have a low melting point and conduct electricity well. Ceramics are the opposite, they are brittle, have a high heat and electrical resistance. Despite or rather because of the great difference in material properties combinations of metallic and ceramic materials are of great importance for many technological applications and a focus of research. For applications that range from electronics, to catalysts and aero-space components. Of special interest are the interfaces, because they determine the adhesion and the orientation relationship of metal and ceramic which in turn can influence the usage parameters and efficiency of devices [4, 5].

An important factor for metal-ceramic interfaces is epitaxy, which means that the orientation of a crystal is determined by the substrate its growing on. This is influenced by chemical properties such as bonding strength and physical properties like the lattice spacing. In principle epitaxy works best for similar lattices, but most combinations of materials have different lattice spacing of the film d_{Film} and the substrate d_{Sub} and therefore a lattice misfit δ:

$$\delta = \frac{d_{Film} - d_{Sub}}{d_{Film}} \tag{2.1}$$

Depending on the misfit and the resulting strain different interfaces may form (Figure 2.1). Interfaces with a low misfit can form a coherent interface. If the strain in the interface gets too large a semi-coherent interface forms where regular dislocations form at the interface. The spacing S between misfit dislocations depends on the lattice misfit δ and the burgers vector b [6]:

$$S = \frac{|b|}{\delta} \tag{2.2}$$

For a strain over $\sim$10% the strain field of the misfit dislocations overlaps to much for a semi-coherent interface and instead a incoherent interface is formed. This view on interfaces is of course simplified. In reality the atoms close to the interface can deviate slightly from the bulk unit cell into a energetically favorable position and form a new periodic cell [5]. The formation of the new interface lattice works similar to surface reconstruction and is often given in the Wood

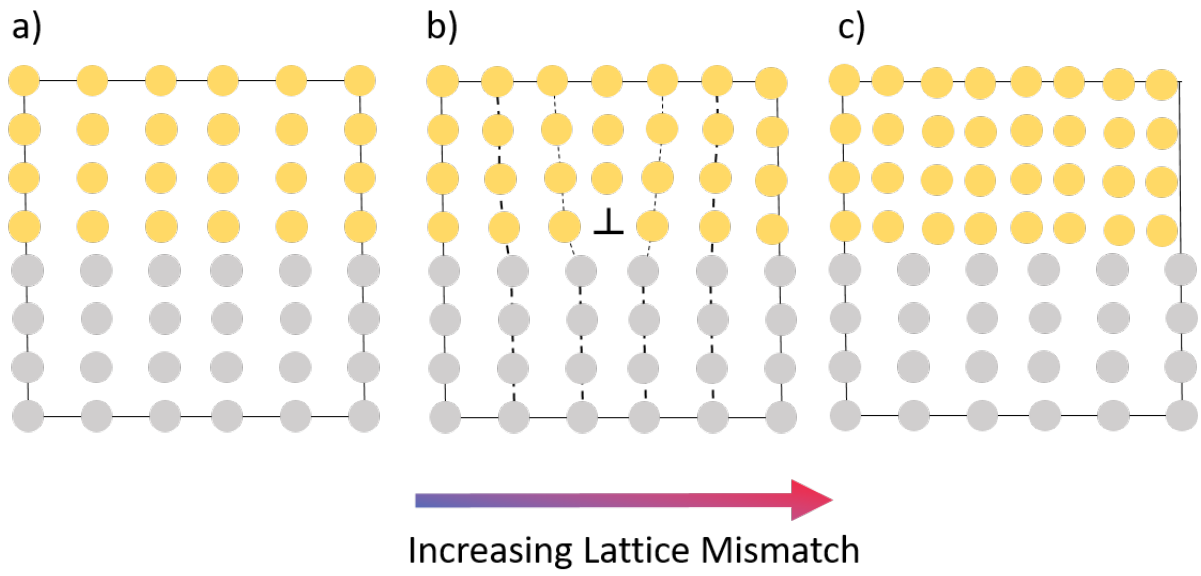

Figure 2.1: Schematic representation of the different interface types that form due to lattice mismatch a) coherent interface b) semi-coherent interface with a misfit dislocation and c) a incoherent interface. (Adapted from Ernst 1995 [4])

notation [7]:

$$X(hkl)x \times y - R\phi \tag{2.3}$$

where a plane (hkl) of the material X changes the length of one direction by the factor x and the other by y. The letter R states that a rotation ϕ is present. For example the Ni/sapphire interface reconstruction has a 30° rotation and is written as: $2.5\sqrt{3}$ x $2.5\sqrt{3}$R30 [5].
This interface reconstruction typically only appears in the first few atomic layers, but can affect the orientation of the film to the substrate.

2.1.1 Orientation Relation of a Film and Substrate

For two crystalline materials some relative orientations of a film on a substrate might appear more often. An explanation of why certain orientations are preferred is given by the "Lock-In"-model from Fecht and Gleiter [8]. This model proposes that the atom rows of the particle or film want to maximize the contact area to the valleys between the substrate atoms. The closer the lattices of both materials match in a certain orientation relation the more rows and valleys fit together and the more pronounced this epitaxial relation will be. This however fails to explain why some OR, with a high lattice misfit and therefore an expected incoherent metal-ceramic interfaces are preferred. Some examples include Pd/ZnO [9], Ag/ZnO [10], GaN/GaAs [11]. An explanation for this given in literature is that the coincidence site lattice (CSL) of the atoms in the film and the substrate forms a super cell with a very low residual strain. The misfit of the CSL δ_{CSL} can be calculated by modifying Equation 2.1 to include the number of atoms for the

film m and the substrate n between two positions of coincidence [11]. Which results in:

$$\delta_{CSL} = \frac{n \cdot d_{Film} - m \cdot d_{Sub}}{n \cdot d_{Film}} \tag{2.4}$$

The Au/ZnO (Figure 2.2) and the Au/sapphire systems have two orientations with a lattice misfit that is observed in other systems. The lower misfit orientation relation (OR1) for both is: $Au(111)[110]|Substrate(0001)[10\bar{1}0]$ at 2.6 % for ZnO and 3.8 % for sapphire. A higher misfit orientation relation (OR2) is found for: $Au(111)[110]|Substrate(0001)[11\bar{2}0]$ at −12.4 % for ZnO and 16.6 % for sapphire.

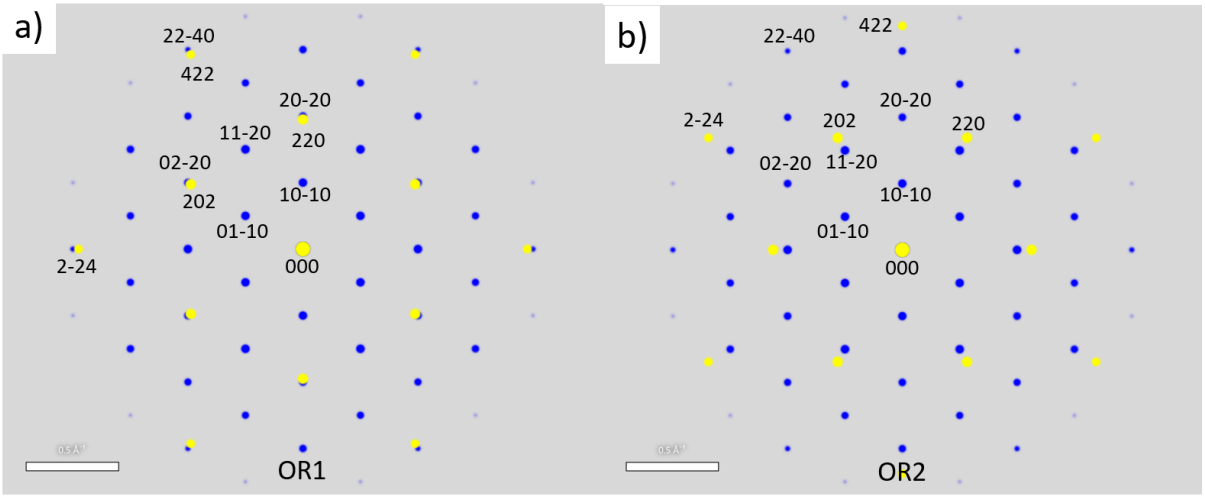

Figure 2.2: SAED simulations of Au (yellow) on ZnO (blue) in a) the orientation relation 1 and b) in the orientation relation 2

2.2 Polar surfaces

Some ionic crystals have a lattice plane that is polar (Figure 2.3), which means the charges from the anions and cations result in a dipole moment. This polarity is for example present in the zinc-blend and wurtzite crystal structure and in these type 3 lattice the dipole moment builds up for each added crystal plane, which would result in a very large surface energy. Usually crystals like this show a reconstruction of the surface atoms to compensate the high energy. In a type 2 crystal individual lattice planes are also charged, but due to their centro-symmetry these charges are immediately compensated by the neighboring planes [12]. The two different lattice types are illustrated in Figure 2.3.

Depending on the surface polarity, the chemical and physical properties such as etching and electrical conductivity can change [14]. This difference in behavior is not only important for applications, but especially the shape of etching pits [15] is often used to confirm the orientation of the crystal. Other methods to confirm the crystal surface polarity are convergent beam electron diffraction [16] and x-ray diffraction [15].

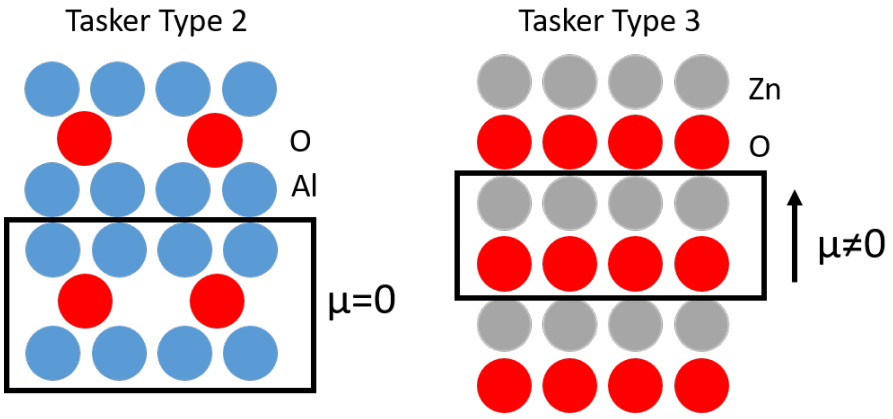

Figure 2.3: Schematic ionic crystal surface classification of Tasker. The crystal lattice of Sapphire (Tasker Type 2) does not result in a dipole moment μ while the wurtzite structure of Zinc oxide (Tasker Type 3) does. Modified from Consonni [13]

2.3 Thin Films

In this chapter some basics phenomena of metal thin films in response to heat treatment are covered. First grain growth is discussed, in thin films this works similar to bulk materials, but the influence of the substrate is more important. This is followed by solid-state dewetting, which is especially important for very thin films.

2.3.1 Grain growth

The grain size is an important value for thin films as well as bulk materials. Smaller grains have in general a higher mechanical strength due to the Hall-Petch relationship. However grain boundaries are points of higher chemical reactivity and they increase the electrical resistance. Controlling the grain size is therefore an important aspect in material design and one of the largest influences is the temperature. An increased temperature allows the grain boundaries to move and the grains to grow, thereby removing high energy boundaries.
In thin films produced by PVD, several factors can influence the as-deposited grain orientation and size. Among the most important are whether there is an epitaxial relationship with the substrate, the growth mechanism and temperature. Directly after deposition the grain size of a thin film depends on the deposition temperature, with smaller grains at lower temperatures. The grain growth of a nanometer scale film on a substrate is divided into two phases, a normal grain growth where all grains grow at the same rate and abnormal grain growth where certain grains with a preferred orientation grow much faster than the rest. For very small grains the normal grain growth can start at low temperatures, but usually only continues until the grains reach a size that is comparable to the film thickness. Abnormal grain growth (also called secondary grain growth) starts at grains that have a preferred orientation due to a low surface and interface energy. These grains will quickly spread while consuming other grains until only the abnormal grains with a favorable energy remain. The growth rate $\frac{dr}{dt}$ of a specific grain r in the film on a

crystalline substrate during abnormal grain growth can be described with this equation [17]:

$$\frac{dr}{dt} = M\left[\frac{\gamma_s^* - \gamma_s}{h} + \frac{\gamma_i^* - \gamma_i}{h} + \gamma_{gb}\left(\frac{1}{r^*} - \frac{1}{r}\right)\right] \tag{2.5}$$

Here the mobility of the grain boundary M is modified by γ_s the surface energy of the grain, γ_i the interface energy of grain and substrate, with γ_s^* and γ_i^* being the average energies of the grains in the rest of the film. The film thickness is h, the average grain radius is r^* and the grain boundary energy is γ_{gb}.
From equation 2.5 it can be concluded that large grains grow faster and that the best orientation is a combination of low interface and surface energy and not necessarily the lowest for both.

2.3.2 Solid-State Dewetting

Solid-state dewetting (SSD) is a phenomenon that describes a process in which thin films agglomerate into particles (Figure 2.4) through diffusion, while the temperature is below the melting point. Dewetting has gathered attention because it can easily destroy microelectronic devices, but also for its potential in producing novel nanometer scale structures [2].

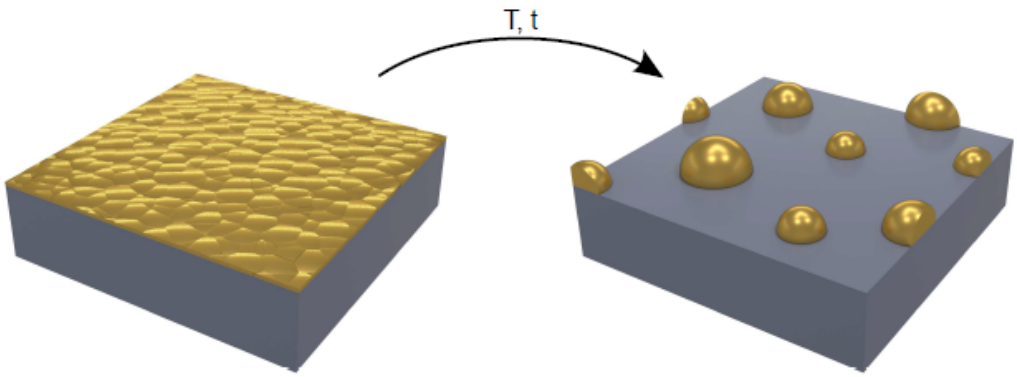

Figure 2.4: A thin gold film agglomerates into particles when heated. When the temperature is below the melting point it is called solid state dewetting (adapted from Niekiel [18])

From a thermodynamic point of view the dewetting process allows a high energy film to transform into energetically more favorable particle by decreasing the surface area. Therefore films with a high surface energy or a low interface energy to the substrate have a higher driving force to agglomerate. In addition there are kinetic factors that influence dewetting, like the initial film thickness, where thinner films dewett faster and the temperature, which is generally tied directly to the surface diffusion rate. The dewetting process itself is divided into several steps: Hole formation, hole growth and the separation of individual islands which in the end results in individual particles. Holes can start at grain boundaries and other defects and continue to grow if they are above a critical hole radius R_c [19]:

$$R > R_c = \frac{h\gamma_{fv}}{\gamma_{fv} + \gamma_{fs} - \gamma_{sv}} = \frac{h}{1 - \cos\theta} \tag{2.6}$$

with the film thickness h, the interface energy of the film and substrate γ_{fs}, the surface energy of the film γ_{fv}, the surface energy of the substrate γ_{sv} and the contact angle of the film or particle and the substrate θ.

After the formation of holes the remaining film recedes and forms a rim with a steadily deepening valley behind, until it reaches the substrate and the so-called pinch-off occurs. The remaining material is often in the shape of a wire or finger. These wires are unstable and break up due to Rayleigh like instabilities, which further decrease the surface to volume ratio and particles are formed. The only way for the particles to further decrease their energy is to form facets with a low surface energy. The resulting particle cross section is predicted by the Wulff construction [20] for free floating particles and the Winterbottom construction [21] (Figure2.5) when they are in contact with a substrate. In a fully equilibrated particle the Winterbottom shape can be used to determine the interface energy γ_i of the particle and substrate [22]. For this an image of the cross-section and the surface energies γ_s of the contacting planes for both materials is needed. Then the interface energy can be calculated with:

$$\frac{R_1}{R_2} = \frac{\gamma_i - \gamma_{s,substrate}}{\gamma_{s,particle}} \tag{2.7}$$

where R_1 and R_2 are the distances in the particle as shown in the schematic Winterbottom construction (Figure 2.5)

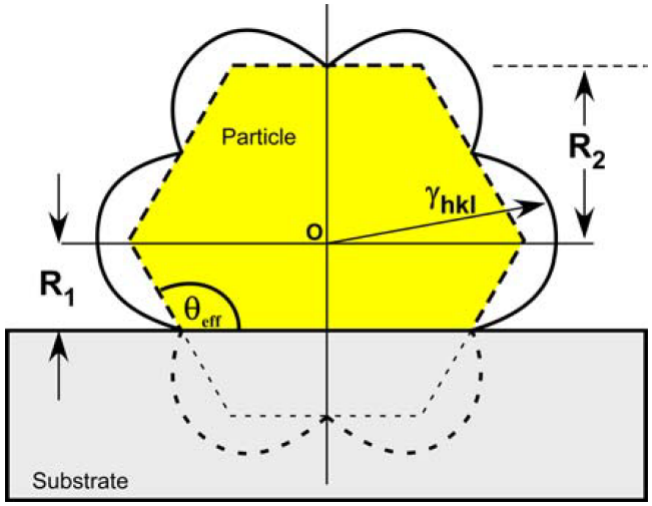

Figure 2.5: A schematic of the Winterbottom construction of a particle on a substrate (adapted from Sadan [22])

The dewetting process can be influenced by a variety of factors which can be used to control the particle size or significantly reduce the kinetics of SSD to keep the film continuous. Larger film thickness slow down the dewetting speed and result in larger particles. Elements with a lower melting point start dewetting earlier and a combination of a film with high surface energy and a substrate to which the interface energy is low hinders dewetting.

Chapter 3

Materials and Methods

3.1 Physical Vapor Deposition

Physical vapor deposition (PVD) methods are generally subdivided in two classes, sputtering and evaporation. During sputtering an ionized gas, often argon, is directed at a target with the desired film material. The gas ions knock out atoms from the target, allowing them to deposit on the substrate and form a film offer time. The film quality can vary widely depending of factors such as gas pressure and ionization rate. Evaporation is a straightforward approach to deposition, the source material is simply heated past its evaporation or sublimation point and the vapor condensates on the substrate thereby coating it. The heating is done with a variety of methods some of which include passing a current through a crucible, a rapidly changing magnetic field or a laser. Another method heats by directing an electron beam from a tungsten filament on the center of the source material (Figure 3.1). This way the crucible receives less heat compared to for example resistance heating, which lowers the chance for contamination [23].

The basic set-up of an electron beam evaporator consists of a vacuum chamber, a holder for high melting point crucibles and a substrate holder above the crucible. Furthermore, a tungsten coil as an electron source with magnets to direct the electrons on the target material and a high voltage power supply is needed. For a high precision of the deposited layer thickness, a calibrated Quartz Crystal Microbalance (QCM) is used. This is a thin quartz crystal which vibrates at its resonance frequency when a voltage is applied due to the piezo electric effect. The crystal changes its resonance frequency due to the increasing weight when material is deposited on it [24] which can be read out in real time to calculate and then adjust the deposition rate. QCMs are calibrated by depositing a film with a desired thickness and then calculating the ratio to the actual value, which can be measured with a variety of methods such as an atomic force microscope (AFM). The suitable materials for evaporation span a wide range and include metals, semiconductors, some ceramics and other multi-element compounds that have a stable gas phase [23].

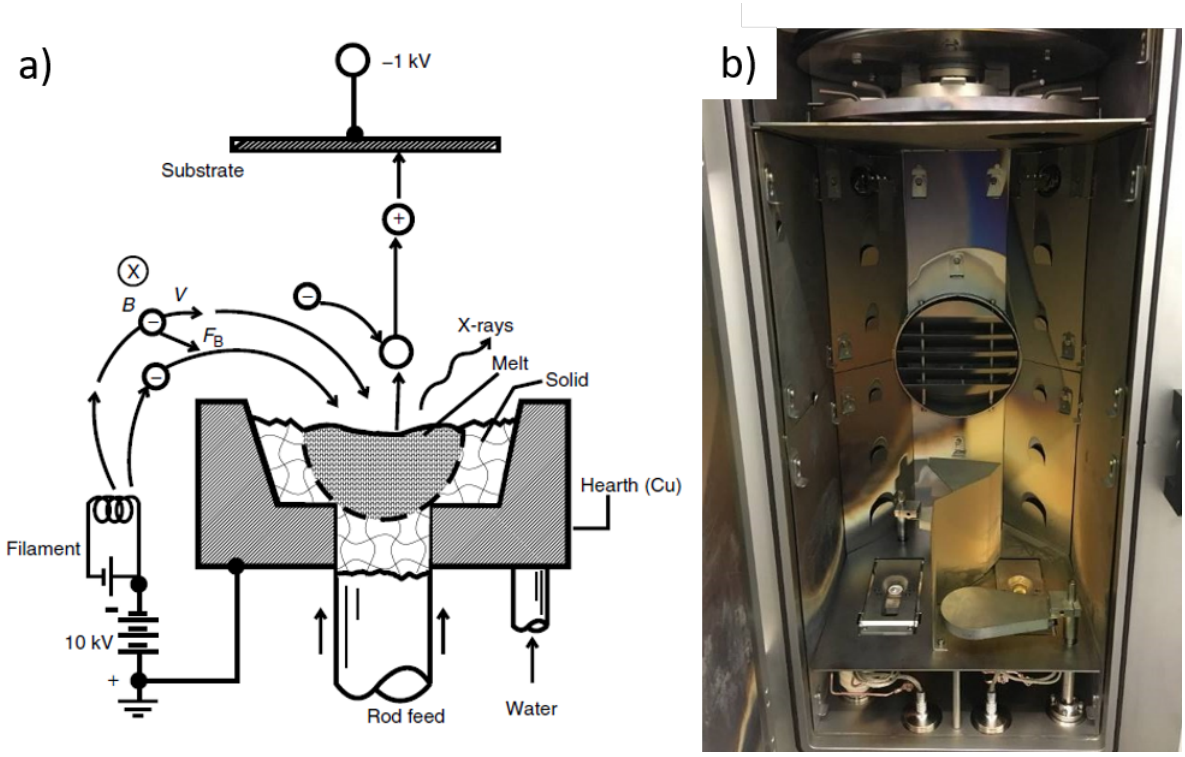

Figure 3.1: a) Scheme of an electron beam evaporator [23] b) Picture of an electron beam evaporator with two sources, which makes deposition of mixed films possible

3.2 Electron Microscopy

Electron microscopes use the interaction of electrons with a sample to create images with a magnification that easily surpass light microscopes. In addition they often are equipped to detect elemental compositions and crystal structures of materials. Nowadays electron microscopy is a valuable tool in material science, biology and even forensics. This section only gives an short overview of the general structure of electron microscopes, electron-sample interaction and some of the ways images are created. A more complete picture is given by the books from Goldstein et al. [25] for Scanning Electron Microscopy (SEM) and Williams and Carter [26] for Transmission Electron Microscopes (TEM).

3.2.1 Scanning Electron Microscopy

In a SEM the electron beam scans over the sample surface and an image is created from the electron-sample interactions. Electrons for imaging can stem from from a cold field emission gun, where a strong electric field pulls out electrons from a narrow tungsten tip. An electron beam from this source has little variation in the energy of the electrons and a high brightness. This means it emits many electrons on the target area and image acquisition is faster. An alternative is a Schottky-emitter, which in addition to the applied electric field, heats the electron source and thereby lowers the required field strength. The performance of a Schottky-emitter is not as good as a cold field emission gun but it has the advantage of not needing as good of a vacuum.

Purely thermionic emitters are rarely used nowadays because they have a higher energy spread and are not suitable for high resolution imaging.
After the electrons leave the source, they are focused by magnetic field lenses and then get directed at the sample. The electrons are accelerated with an energy of up to 30 keV and as low as 0.5 keV and focused to a small spot on the sample. Due to the relatively low energies and the thick samples, the electrons can penetrate deep in the material and scatter elastic and inelastic with an interaction volume of several μm. The electrons that are created by inelastic scattering are called secondary electrons (SE), they have a low energy and only leave the sample when they are created close to the surface. If the interaction volume is larger than the imaged structure, a lot of SEs can leave the sample and give a great topographic contrast. Electrons that mostly scatter elastically and leave the sample with a high energy are called back scattered electrons (BSE). The scattering angle depends on the mass of the atoms with heavier elements scattering more and giving a larger BSE signal, which results in a contrast depending on the atomic number Z of the sample atoms.
A measurement of the precise elemental composition is not possible with BSEs, for this x-rays are usually used. The specific x-rays are created when an electron from an outer shell falls towards the core and releases the energy difference as a photon. With energy dispersive x-ray spectroscopy (EDX or EDS) the photons and their energy are detected and the intensity is correlated to the presence of elements in the sample. For a quantitative elemental composition some other factors need to be taken into account, among them are the different x-ray generation abilities and the absorption of different elements [25].

3.2.1.1 Focused Ion Beam

A Focused Ion Beam (FIB) is often used in an SEM for the preparation of micro and nano scale samples by precise removal or deposition of materials. Furthermore the electrons and particles that result from the interaction of the ion beam with the sample can be used for imaging. The ions most commonly used in a Dual-beam SEM/FIB are from a gallium source, because its low melting point allows the formation of a very small tip of liquid metal, from which ions are extracted with an electric field. This narrow tip aids in the formation of a nano meter size ion-probe on the sample. The ion beam is focused and directed with a similar setup as the electrons, with one major exception being the electrostatic lenses, which are used instead of the electromagnetic ones. This is done because the electromagnetic force is inversely proportional to mass, which means that the heavy Ga ions are much more efficiently directed with a electrostatic lens [27].
A common usage for a FIB is the preparation of TEM cross-section lamellas from a precisely chosen location of a larger sample. The procedure (Figure 3.2) usually starts with the deposition of a protective carbon or platinum layer by cracking a precursor molecule that leaves the respective elements behind. This is first done slowly with the electron beam to protect the sample from damage and Ga implantation and then continued with ion beam induced deposition (IBID) until several micro meters are deposited. In the next step trenches at three sides and below the

desired sample area are created with the ion beam. During this step partial redeposition of the ablated material occurs, which can be removed with the ion beam. To transport the lift-out to the sample holder a micro-manipulator is moved close to the sample and connected via carbon deposition. Then the last connection to the sample is removed and the lamella is attached at the sample holder with another deposition. In the final step the lift-out is thinned with the ion beam until it reaches a sufficient thickness that is electron transparent. In the last steps of the thinning process the ion beam energy is decreased. This increases the time needed to remove material, but the resulting surface is less damaged [28].

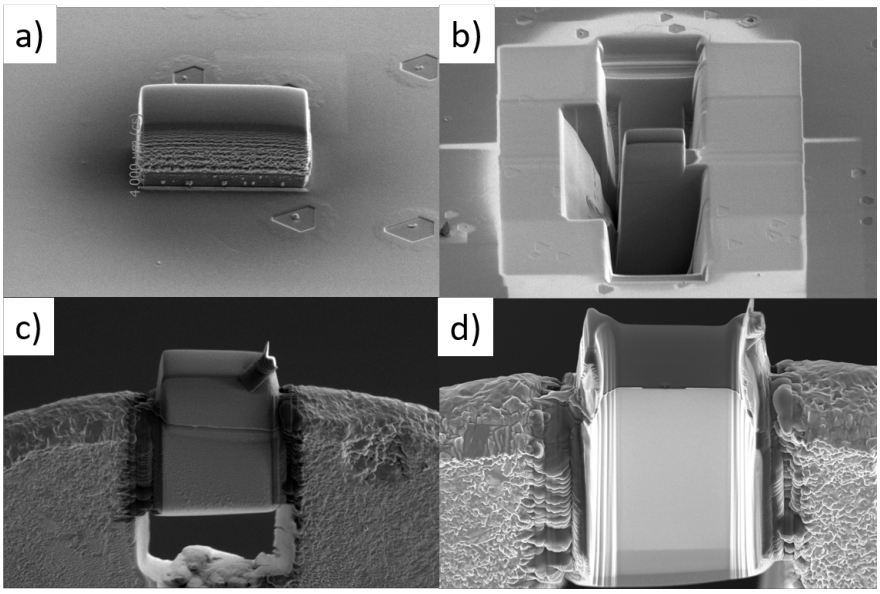

Figure 3.2: a) A carbon layer is deposited on the lift-out area, first with the electron beam and then with a low current ion beam b) ditches are dug around the lift-out and a micro-manipulator is attached (not shown) c) the lamella is reattached to a copper sample holder with carbon deposition d) in the final step the lift-out is thinned to the desired thickness while step wise decreasing the ion beam energy to limit its damaging effect

3.2.2 Transmission Electron Microscopy

In a transmission electron microscope (TEM) the sample needs to be transparent to electrons. This is achieved by a high electron energy that usually ranges between 80 keV and 300 keV and through very thin sample thicknesses. Some samples might get damaged from the high energy electrons, but when the requirements are fulfilled atom scale images with a resolution of up to 0.05 nm [29] can be taken. Based on the small wavelength of the electrons of around 1 pm even better resolutions are physically possible, but in practice it is limited by fluctuations in the electronics and abberations from the electromagnetic lenses. Conventional imaging in the TEM uses a parallel beam that passes through the sample, then bright field and dark field images are generated by using an aperture to block either the diffracted or undiffracted electrons. In the STEM mode the electron beam is focused on the sample and scanned over the imaging area, similar to the SEM. The transmitted electrons are detected according to their scattering angle, which depends on the mass of the atoms and the thickness of the sample. A heavy atom has

a strong scattering effect and would give a low signal on the bright field detector and a strong signal on the dark field detector, with the opposite happening for a light atom. In addition to the good contrast in many material systems the STEM setup has the advantage that there are no lenses behind the sample and therefore no abberations once the electrons interact with the material. Furthermore due to the electron probe being scanned over the sample, EDX mappings can be performed. The principle behind EDX in the TEM is the same as in the SEM, only the correction algorithms are adjusted to the high electron energy and the thin samples [26].

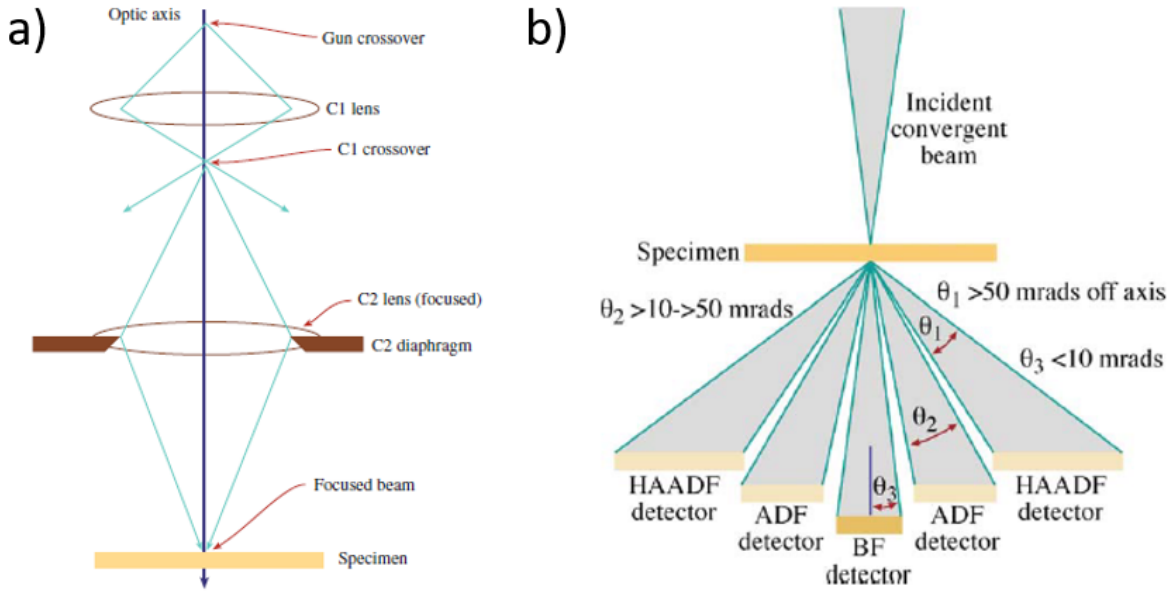

Figure 3.3: a) STEM scheme and b) the detector setup commonly used in STEM (both images are from Williams and Carter [26])

An advantage of STEM over conventional TEM is that high resolution STEM (HRSTEM) is easier to interpret. Interpreting a HRTEM image without accompanying simulations is often difficult, because the phase contrast depends on the sample thickness. For HRSTEM this is easier because the images from the high angle annular dark field (HAADF) detector have an atomic mass depended contrast, that can be directly interpreted [26].

3.3 Diffraction Methods

3.3.1 Electron Back Scatter Diffraction

Among the various scattering methods used to determine grain orientations, electron back scatter diffraction (EBSD) is of great importance, because it can scan over the sample surface. In contrast to the usual scattering methods, that average over a larger volume, EBSD gives local information of single grain orientations. Modern EBSD detectors have a good spatial resolution of better than 20 nm and are mounted in a SEM, so the sample size can be quite large. After hitting the sample, the electrons are diffusely scattered and some of them can fulfill the Bragg condition with the crystal planes of the sample. Electrons close to the surface can exit the

sample without further scattering. When exiting the sample the BSEs are distributed in the form of Kossel cones and the detector intersects them, which leads to Kikuchi bands [25]. These Kikuchi bands can be used to determine the orientation of the scanned area in three dimensions. Electrons that pass into areas deep in the sample will scatter multiple times and will only contribute to background noise. The detector itself is a fluorescent screen that starts glowing in places where electrons hit it, which is then filmed by a CCD or CMOS camera. In a computer software the bands in the Kikuchi pattern are indexed by doing a Hough transformation (Figure 3.4) [30].

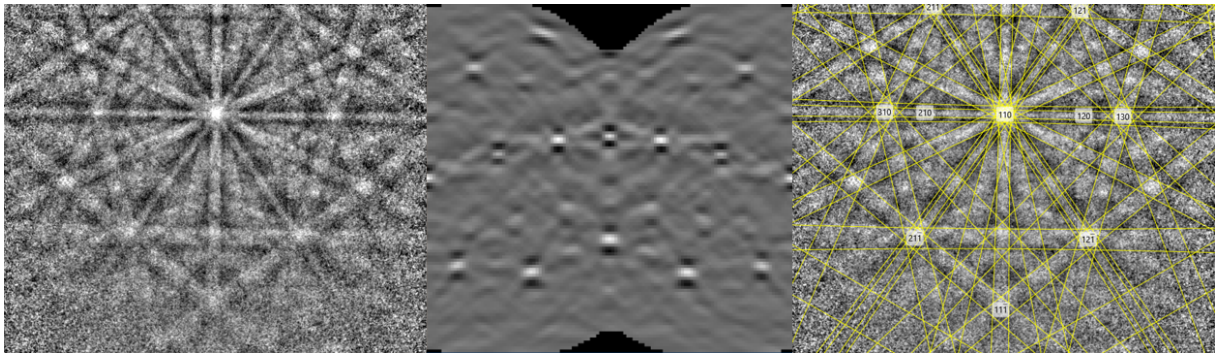

Figure 3.4: From left to right: The raw Kikuchi pattern of a gold grain with a (111) texture. Hough transformation of the Kikuchi pattern. The pattern with all detected bands marked by yellow lines and fully indexed

This makes points out of the bands in the Kikuchi pattern and is easier to process for the program, so that the crystal orientation can be determined for every scan point. The result is a map with different colors for the pixels based on the grain orientations.
Another common display method for the EBSD orientation data are pole figures, these can be understood by imagining a crystal in the center of a sphere (Figure 3.5a). From each surface of a family of planes a line normal to the surface is drawn until it reaches the sphere in the point P. Then a line is drawn from P to the south pole of the sphere and the intersecting point with the spheres equatorial plane is recorded. This process is repeated for each scanned point of the EBSD map and the final equatorial plane with all intersecting points is the pole figure. For most PF a Wulff net is added for better readability, which consists of lines to show a certain angle spacing. The pole figure of a (111) out-of-plane orientated single crystal would show four points for the $\langle 111 \rangle$ planes, one in the center and three at a distance of 70° from the center, with 120° orientation to each other. The same pole figure for a twinned crystal shows an additional three points with a 60° orientation to the previous ones (Figure 3.5b). Another way to display crystal orientations is the inverse pole figure (IPF), which has the advantage to show each scan point only once as a singular point making some textures easier to see. A difference to the PF is that the each IPF is oriented to a certain sample orientation and contains all crystal planes in the same plot. The IPF is often used to color EBSD maps by assigning each corner one of the primary colors (Figure 3.5c) and painting the grains according to their orientation [25].

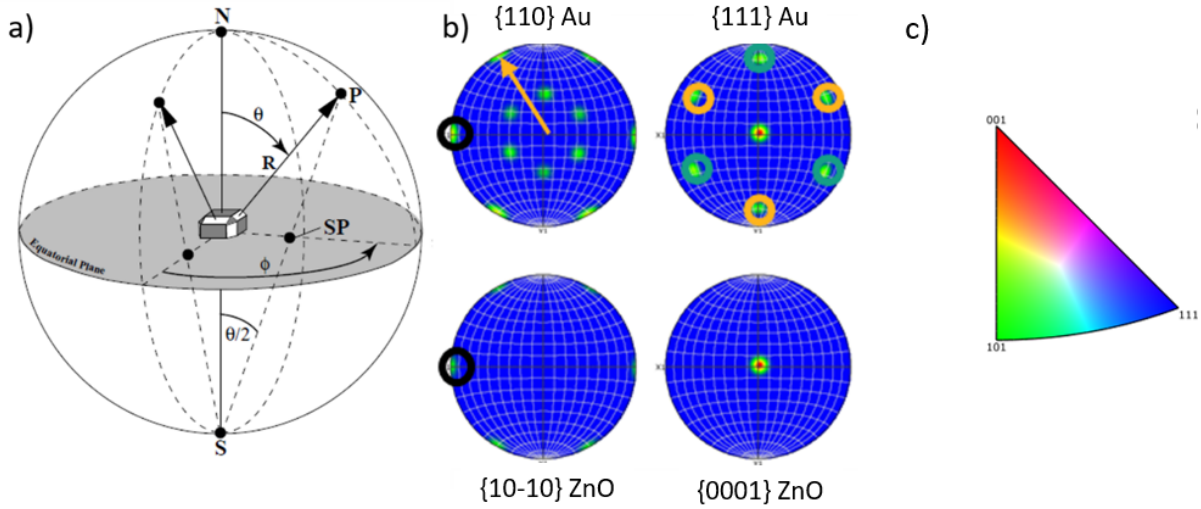

Figure 3.5: a) In the stereographic projection the normal of a crystal plane is projected on a sphere, the point SP where the line between the sphere P and the south pole S meets the center plane is displayed in the pole figure (reprinted from De Graef [31]) b) pole figures of Au and ZnO and a Wulff net with a 10° spacing, the Au{111} has 6 points separated by 60° around the center spot which means that Σ3 twin grains are detected. The Au{110} and the ZnO{10$\bar{1}$0} have overlapping points (marked by black circle), this signifies a parallel orientation relation of the crystals. c) The coloring scheme most commonly used to visualize the orientation of grains in a inverse pole figure map

3.3.2 Selected Area Electron Diffraction

Electrons can be seen as both particles and waves and are therefore susceptible to scattering. When the electrons hit the regular crystal lattice of a sample, they experience constructive and destructive interference, which means regions of high and low intensity are created. In a TEM selected area electron diffraction (SAED) is realized by blocking electrons so that only those from the area of interest can pass to the detector. A lens set-up magnifies the signal from the back focal plane and an image of the diffraction is created. For constructive interference to happen, the Laue condition needs to be fulfilled [26]:

$$\Delta k = k_D - k_I = g \tag{3.1}$$

with k_D, the diffracted wave vector and k_I, the incident wave vector having the length $\frac{1}{\lambda}$. g relates to the real space lattice planes d with $g = \frac{2\pi}{d}$. The SAED pattern of a single crystal usually consists of several bright diffraction spots around the undiffracted zero beam that has not experienced scattering. This diffraction pattern can be understood by the reciprocal lattice of the crystal. When transforming a crystal from the real space to the reciprocal space the length between to atomic planes goes from d to $\frac{1}{d}$ and the directions are perpendicular to the originals. The diffraction with a wave or particle of wavelength λ is visualized in the reciprocal space by the Ewald sphere (Figure 3.6) with a radius $\frac{1}{\lambda}$. Every point that intersects with the Ewald sphere results in a spot in the diffraction pattern. Electrons have a small wavelength and therefore a large radius of the Ewald sphere which causes many diffraction spots.

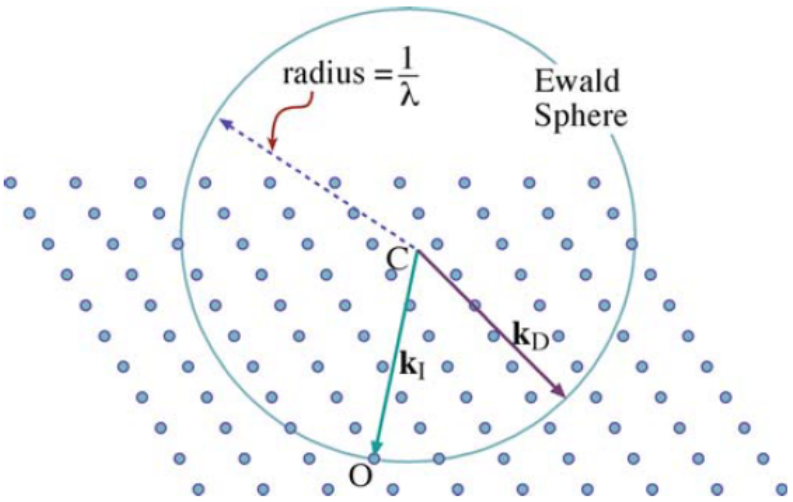

Figure 3.6: Ewald sphere on a reciprocal lattice, the points cut by the sphere result in a diffraction spot in the SAED pattern. From Williams and Carter [26]

While constructive interference in reciprocal space is described by the Laue equation, a more common way to express it in dependence of the d-spacing is Bragg's equation [26]:

$$n\lambda = 2d\sin\theta \tag{3.2}$$

where n is the diffraction order, λ is the wavelength and d is the lattice spacing, that corresponds to the respective scattering angle. The Bragg equation allows a more direct calculation of the scattering angle θ.
The spacing d for a specific lattice directions can be calculated from the geometry of the unit cell. For a fcc crystals it is calculated with [32]:

$$d = \frac{a}{\sqrt{h^2 + k^2 + l^2}} \tag{3.3}$$

and for a hexagonal crystals with [32]:

$$\frac{1}{d^2} = \frac{4}{3}\left(\frac{h^2 + hk + k^2}{a^2}\right) + \frac{l^3}{c^2} \tag{3.4}$$

where a and c are the lattice constants of the respective crystal and h, k, l are the Miller indices for the lattice planes.

Convergent Beam Electron Diffraction

If a convergent beam is used instead of a parallel one the diffraction pattern looks different. The electrons in this convergent beam electron diffraction (CBED) now reach the crystal planes at a range of different angles and are therefore scattered in the form of discs. The discs itself usually contain complex dark and bright contrasts. These can be divided into: dynamical diffraction

fringes, higher order laue zone excess- and deficiency-lines and Kikuchi-lines. The basic principle for all these features is scattering and a full discussion is provided by Williams and Carter [26]. An advantage of CBED over conventional SAED is, that areas below 100 nm can be probed. This technique is able to gather a variety of information about a material. Among them are the sample thickness, information about strain and defects. Furthermore in an asymmetric crystal the discs on opposite site of the zero beam can be different in some sample directions, which is used to determine the orientation of such crystals [26].

3.3.3 X-Ray Diffraction

A diffraction method that does not rely on electrons is x-ray diffraction (XRD). This technique averages over the sample, but can be used for samples that are much too large for SAED. XRD can therefore be employed for correlative work with an TEM. One of the most common techniques of applying XRD is by the Bragg-Brentano geometry (Figure 3.7). In this setup the x-ray source and the detector are either rotated around the stationary sample or the sample moves while source and detector stay still. In this set up a large number of angels θ are scanned and most crystal planes parallel to the sample surface give an intensity. For the x-ray wavelength

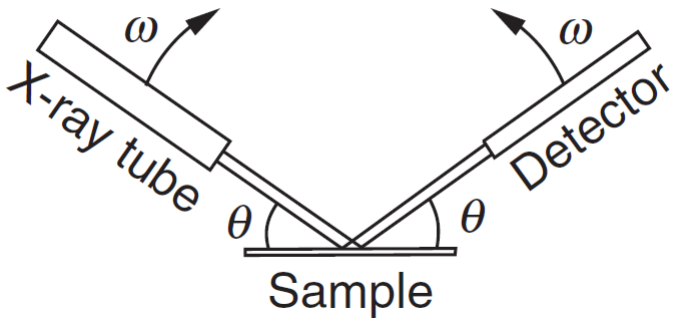

Figure 3.7: The Bragg-Brentano or θ-2θ geometry for x-ray diffraction. From de Graef [33]

Cu Kα1 at 1.5046 Å is commonly used, but other sources are also possible. From the source the x-rays are directed at the sample, where they are diffracted according to Braggs law. At the detector the intensity at each angle is recorded which results in a plot where the peaks can be correlated to specific crystal planes. The equations 3.2, 3.3 and 3.4 apply to all scattering methods and can be directly used for XRD data [33].

3.4 Materials

3.4.1 Zinc oxide

Zinc oxide (ZnO) (Figure 3.8) is under normal conditions a colorless ceramic in the wurtzite structure, which starts to sublimate at around 1300 °C. Among the special properties of ZnO are piezo- and pyro electricity, a color change to yellow at elevated temperatures due to the formation of oxygen vacancies and a high direct band gap of about 3.3 eV. The basic crystal

structure consists of a zinc and oxygen layer, which expands along the (0001) plane. Several of these individual zinc and oxygen stacked on top of each other results in the ZnO crystal. Depending on the orientation, a single-crystalline substrate with a [0001] growth direction can therefore have a surface with either Zn-ZnO (0001) or O-ZnO (000$\bar{1}$), both of which are polar [34, 35]. Some publications state that they have a Zn-terminated surface for both the Zn-ZnO and the O-ZnO side [9, 36], which might be influenced by the oxygen partial pressure during annealing experiments. Zinc oxide is a Tasker type 3 polar crystal (see Chapter 2.2) and this would usually cause surface reconstruction to compensate the positive charges on the Zn and the negative charges on the O side [12]. However in the case of ZnO Low Energy Electron Diffraction (LEED) measurements show a (1x1) surface [37], which means the atoms at the surface are in the same configuration as the bulk unit cell without any reconstruction. The reason for the high surface stability is not fully understood, among the proposed solutions are adsorption of impurities and a missing 25 % of the Zn or O atoms of the terminating atomic layer. Scanning Tunneling Microscopy (STM) reveals triangles in the Zn-ZnO surface and hexagons in O-ZnO. The triangles have a 180° orientation to each other with a step height of c/2 and with O terminated edges in a ratio that fits the 25 % missing surface ratio [38].

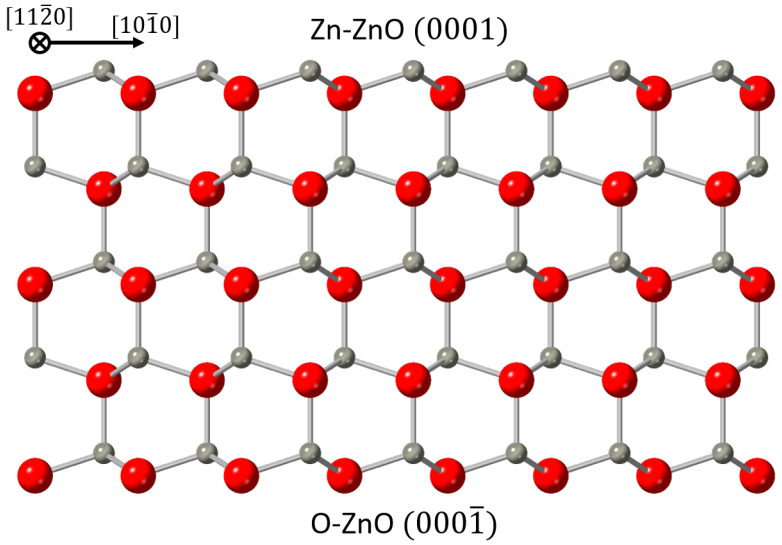

Figure 3.8: ZnO (0001) viewed in the [11$\bar{2}$0] direction (with Zn atoms in grey and O in red) crystal with the Zn(0001) termination on the top and the O(000$\bar{1}$) termination at the bottom

ZnO is widely used in paints, sunscreen and rubber additives, mostly in the form of particles. Some proposed high-tech applications for ZnO include UV LEDs [39], hydrogen sensors [40], spintronic devices [41] and radiation hardened micro controllers [42]. For these applications metal deposition directly on the ZnO surface are often necessary, but can cause degradation when the metal-oxygen bond of the added element is stronger than that to the Zn atoms. This effect is weaker on the Zn-ZnO side due to more favorable metal-metal bonds, but will still happen with sufficiently high temperatures [43, 44]. It is therefore necessary to plan experiments in this direction with the right temperatures and materials.

3.4.2 Sapphire

Sapphire consists of aluminum oxide with the chemical composition Al_2O_3 crystallizes in a hexagonal lattice. The crystal structure is centro-symmetric (Tasker type 2) and therefore all possible surfaces are non-polar. One applications for artificial grown sapphire wafers are as a substrate for hetero epitaxial growth of LED materials, doped sapphire crystals are also used in lasers [45].

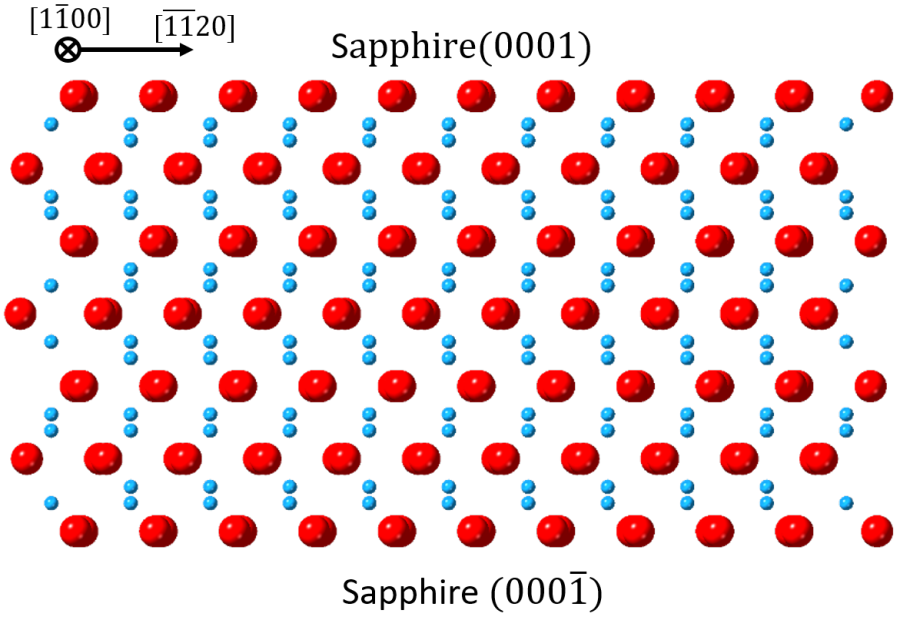

Figure 3.9: The crystal structure of sapphire viewed in the [1$\bar{1}$00] direction, with O in red and Al in blue

Table 3.1: Sapphire material properties [46]

Melting Point	2053 °C
Lattice parameter	a=4.76 Å; c=13.0 Å
Thermal expansion coefficient $\alpha_{Sapphire}$	$5.3 \times 10^{-6}\,K^{-1}$ parallel to c-axis $4.5 \times 10^{-6}\,K^{-1}$ perpendicular to c-axis

3.4.3 Gold

Gold is a noble metal with a face centered cubic (fcc) lattice structure (Figure 3.10) with the lattice parameter of a=4.07 Å[47]. It is well known to be non reactive under standard conditions and often used in electronics as a corrosion resistant contact. Another important application is for catalysis and in chemical reaction, for example in the vapor-liquid-solid growth of Si whiskers [48].

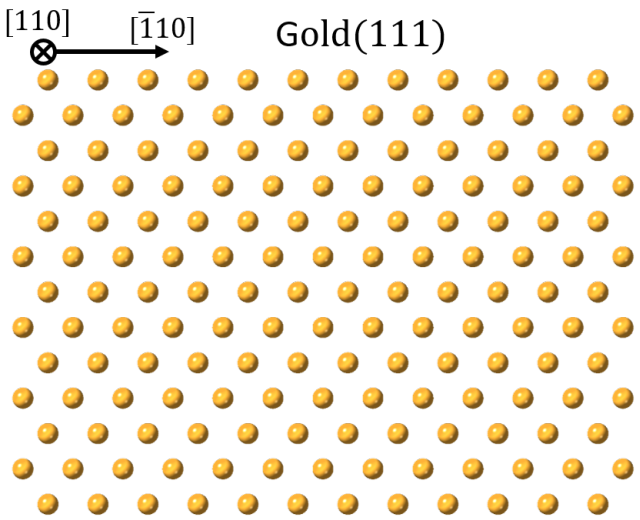

Figure 3.10: The crystal structure of Au viewed in the [110] direction

Table 3.2: Gold material properties

Melting Point	1064 °C [49]
Lattice parameter	4.07 Å [47]
Thermal expansion coefficient α_{Au}	$1.40 \times 10^{-6}\,\mathrm{K}^{-1}$ [50]

3.5 Sample preparation

Sapphire (0001) and hydro thermal grown Zinc oxide substrates with a zinc termination (0001) and a oxygen termination (000$\bar{1}$) (all from supplier *CrysTec*) were cleaned in an ultrasonic acetone bath, rinsed with isopropanol and ethanol and dried in a nitrogen flow. In addition each sample was plasma cleaned for 3 minutes in a 20 % oxygen/argon plasma. The metal films were deposited on the substrate by electron beam evaporation in the Winter Vakumtechnik HVB 130 at 10^{-5} mbar and an deposition rate of $0.5\,\text{Å}\,\mathrm{s}^{-1}$ from 99.99 % (ESG Edelmetall-Service GmbH) pure source material. Films containing nickel were evaporated without breaking the vacuum from 99.995 % (EVOCHEM Advanced Materials GmbH) pure metal. The thermal processing of the samples was performed in the AnealSys rapid thermal annealing (RTA) furnace (Figure 3.11), which heats samples via infrared halogen lamps situated over the sample.
For the annealing, the samples are put on a SiNx coated silicon wafer, that is supported by three quartz pins. When the pins are retracted the wafer falls on a water cooled metal plate, which allows for a high cooling rate of up to several hundreds $^\circ\mathrm{C}\,\mathrm{s}^{-1}$. For the samples prepared in this thesis the heating rate was kept at 100 °C/s and the fast cooling mode is used which reaches about $200\,^\circ\mathrm{C}\,\mathrm{s}^{-1}$. Realizing an low oxygen environment in the chamber was done by first flushing the chamber with argon four times, pumping down to 10^{-4} mbar and then inserting the desired gas. The different atmospheres used were nitrogen at a flow rate of 500 sccm, an argon hydrogen mixture where the chamber was first filled with nitrogen and then a 2000 sccm argon and 100 sccm hydrogen flow was set and for some samples the annealing was down in vacuum

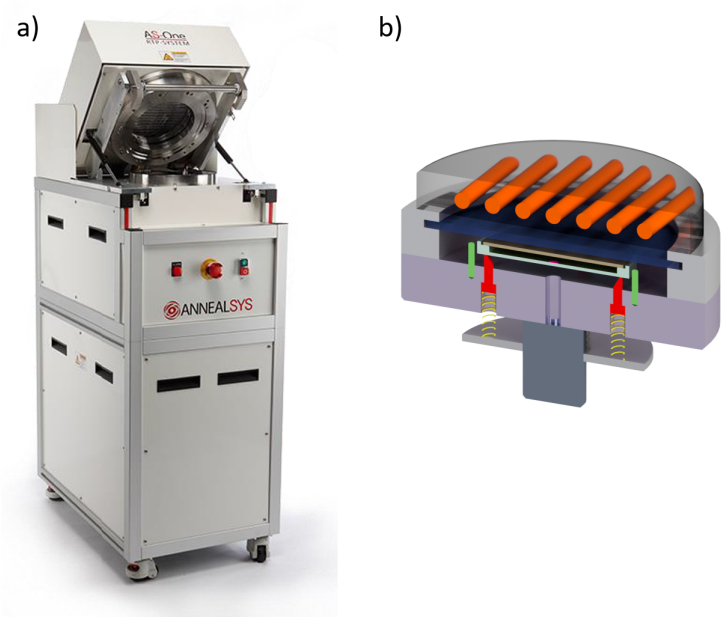

Figure 3.11: a) The rapid thermal annealing furnace AS-One 100 from Annealsys used in this thesis [51] b) A schematic cross-section of the RTA furnace, the infrared heating lamps are shown in orange above the chamber, from which it is separated with a quartz glass

at a pressure of ¡10^{-4} mbar. In the RTA the vacuum pressure is measured with a full range cold cathode pressure gauge and the gas flows are controlled with mass flow controls, that are calibrated for the respective gases.
The microscopic sample characterization was mainly performed by scanning electron microscopy (SEM) in the Phenom ProX Tabletop SEM and the FEI Helios NanoLab 660, the latter was also used for lift-out preparation by focused ion beam as well as EDX and EBSD measurements. Prior to the electron-microscopic investigations all samples are coated with approximately 5 nm of carbon to prevent drifting. The following TEMs are used for the analysis of lift-outs, the FEI Titan Themis^3 300 was used for diffraction, STEM imaging and HRSTEM imaging and the Thermo Fisher Scientific Spectra 200 C-FEG for HRSTEM imaging. For X-ray diffraction (XRD) the Rigaku Smartlab of the Insitute for Crytallography and Structural Physics is used. Some software was used in the analysis and evaluation of images and data, this includes ImageJ and the Atzec packages from Oxford for EBSD and EDX. For TEM images and EDX measurements the software Velox was used and for curve fitting of XRD data LIPRAS [52] is applied.

Chapter 4

Results

4.1 Solid State Dewetting and Texture Evolution of Au on Sapphire

4.1.1 Dewetting

Dewetting of gold on sapphire is relatively well known and acts as a comparison to the Au/ZnO system, with both substrates having a hexagonal lattice, being single crystals and polished on the c-plane. On sapphire the gold is deposited on the (0001) plane, with the parameters described before. From the SEM images of the samples heated under constant nitrogen flow (Figure 4.1) large holes are clearly visible, that means the Au film is already dewetting at temperatures of 800 °C. At longer annealing times and higher temperatures, dewetting progresses further and in the end the film completely transforms into particles. A look at the change in covered area (Figure 4.2) draws a similar picture. The lines are decreasing linear over the measured times until they reach the point where the continuous film is completely transformed into fingers. After this the transformation of fingers into particles results in only a negligible change of covered area and the lines for the different temperatures are slowly tending to the same minimum value of ∼14 %.

In the direct comparison of the nitrogen and hydrogen/argon annealing atmospheres as well as vacuum at 10^{-4} mbar, it is obvious that the dewetting rate is affected. The nitrogen samples have the fasted dewetting progression followed by the Hydrogen/Argon mixture and vacuum is the slowest (Figure 4.3). The covered area plot (Figure 4.4) shows the same dewetting rate quantitatively, with nitrogen being the fastest and vacuum the slowest. To little samples were prepared for an extensive study of hole and particle size distribution, but from the the 850 °C and 900 °C vacuum and the 800 °C and 850 °C hydrogen/argon samples it appears the lower dewetting kinetic of vacuum results in more holes that grow slower.

Of note are the small dark spots in the samples with a mostly intact Au film. They have a much smaller diameter (100 nm) than the bigger holes from advanced dewetting, but have a similar contrast. An AFM scan (Figure 4.5) imaged the large holes that reach to the substrate with a rim of 65 nm and a blister with a height of 320 nm indicating a large strain at the Au/sapphire interface. However the AFM map does not show the smaller dark spots of the BSE image,

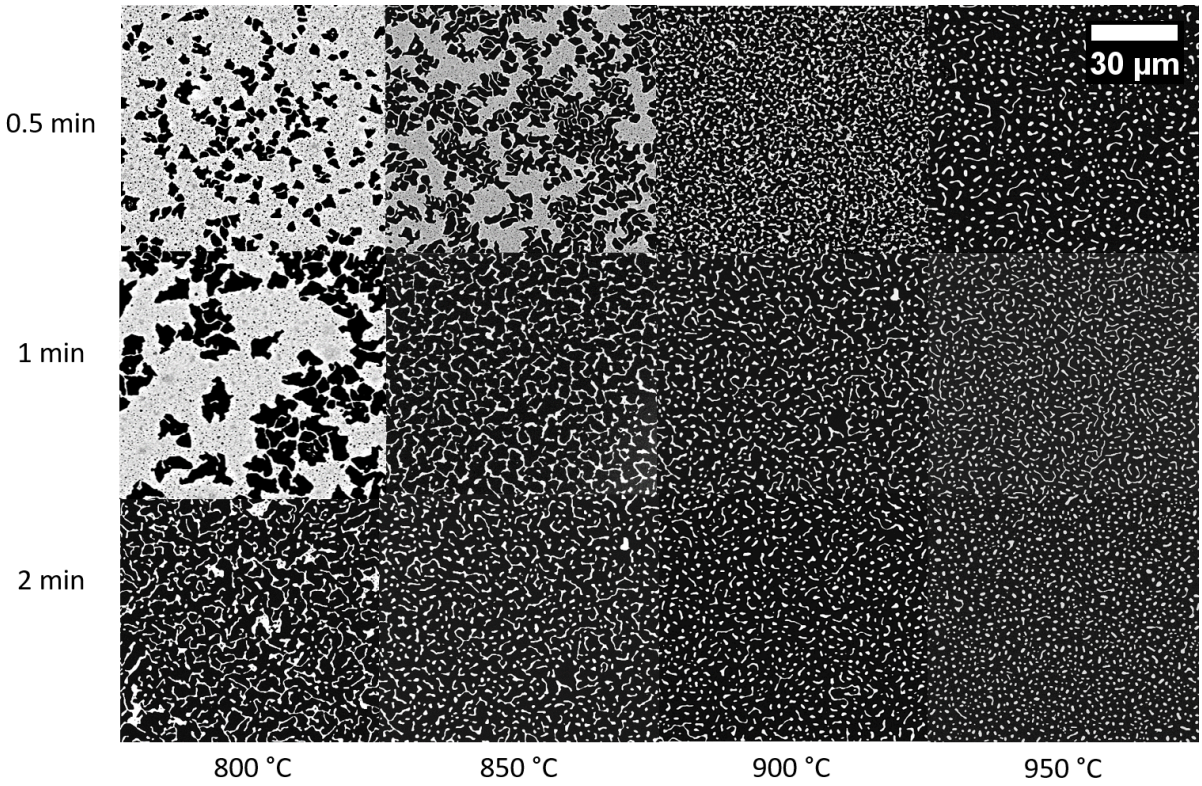

Figure 4.1: Au on c-plane sapphire heated at different times and temperatures with constant nitrogen flow. Samples annealed at higher temperatures and for longer times show further advanced dewetting. In these BSE images the sapphire substrate is black, the gold film and particles on top are white/grey. The scale bar at the top right corner is valid for all images.

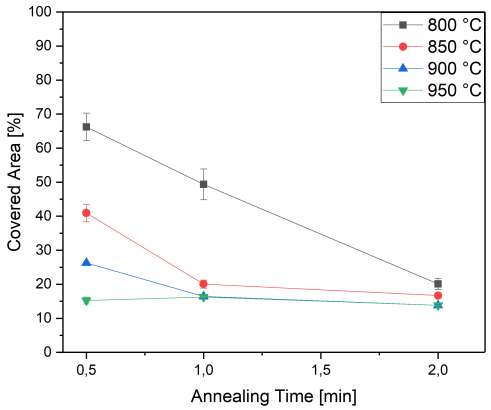

Figure 4.2: The area of the sapphire substrate still covered by gold after dewetting at temperatures between 800 °C and 950 °C in a nitrogen atmosphere. At longer annealing times and at higher temperatures the covered area decreases up to the minimum value of 14 %, where only particles are left.

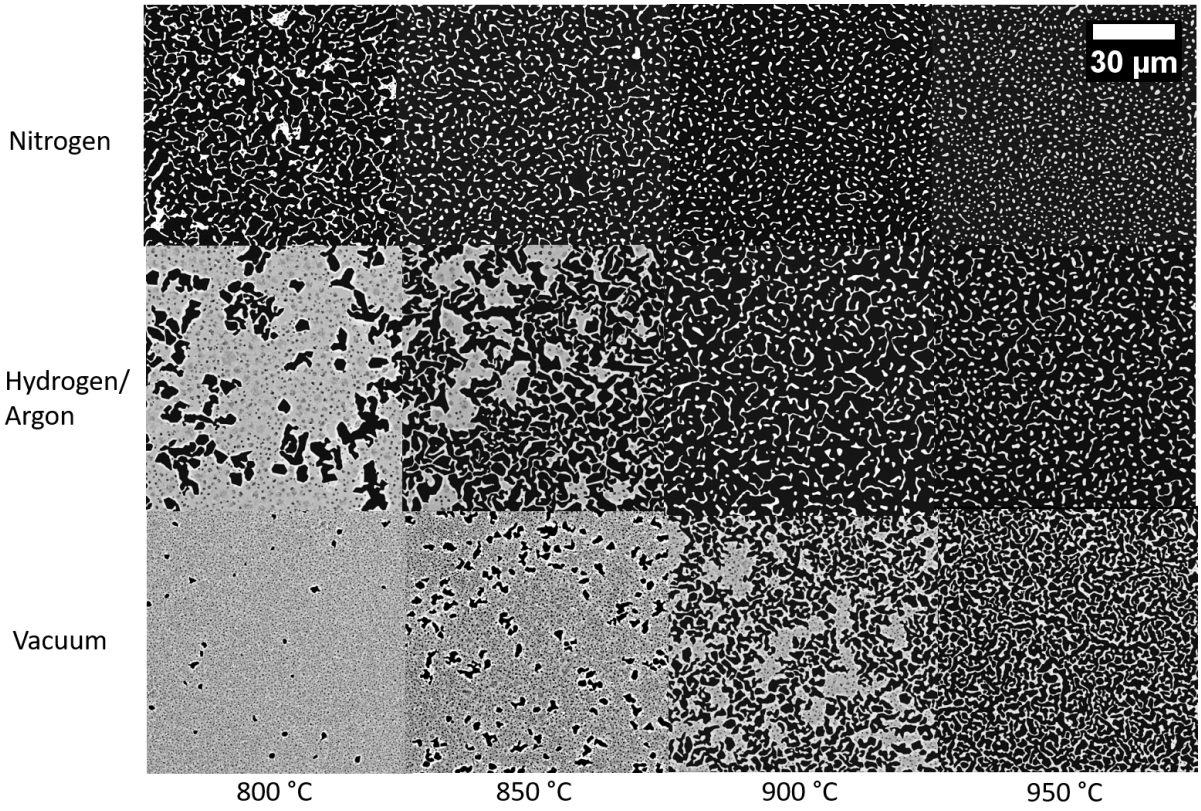

Figure 4.3: Au on sapphire annealed in nitrogen, hydrogen/argon and vacuum atmosphere for 2 minutes at different temperatures. The nitrogen atmosphere causes faster progression of dewetting at the same temperatures, followed by hydrogen/argon and vacuum is the slowest. In this BSE images the sapphire substrate is black and the gold is grey. The scale bar at the top right corner is valid for all images.

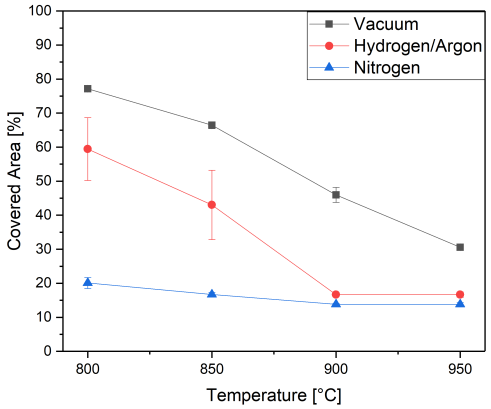

Figure 4.4: The area of the sapphire substrate covered with gold after annealing for 2 minutes in nitrogen, vacuum and a hydrogen/argon mixture. The ambient atmosphere influences the dewetting rate with nitrogen being the fastest, followed by hydrogen/argon and vacuum is the slowest.

instead only a continuous film is seen.

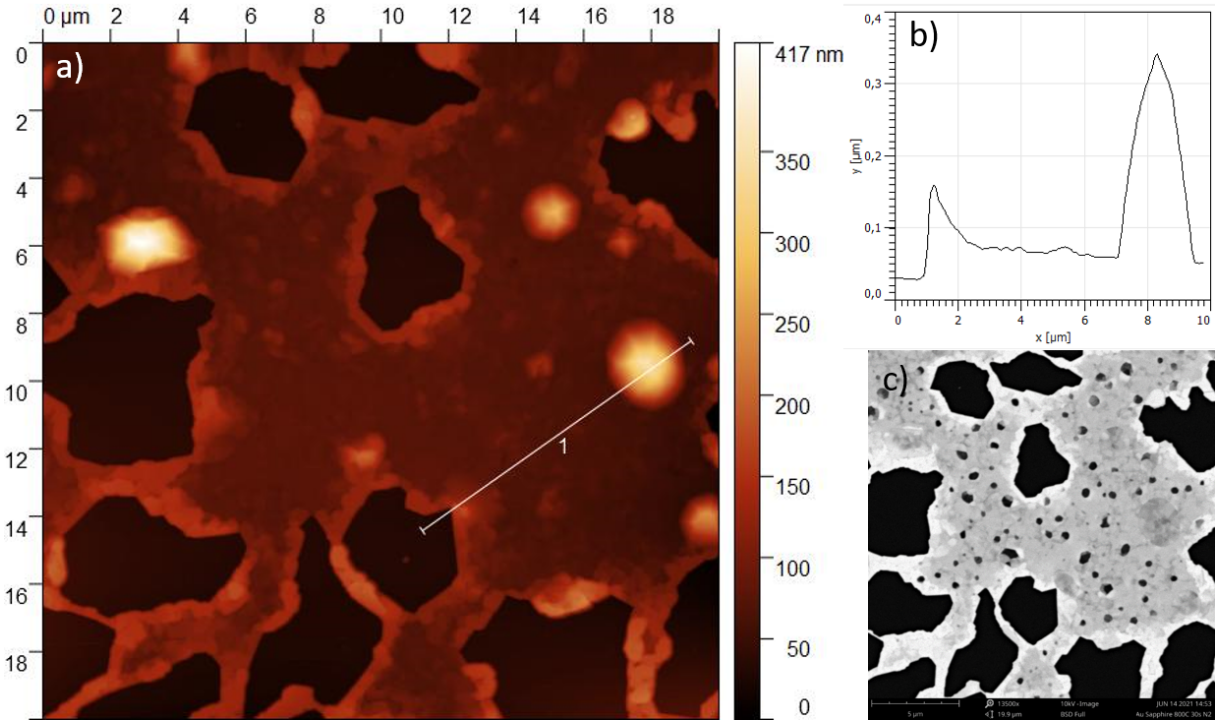

Figure 4.5: a) An AFM image where the the large holes are colored black but the small holes are not distinguishable from the Au film b) the height profile from the marked line of a rim and a blister c) a SEM image of the sample at the same position

4.1.2 Texture Evolution

For Au on sapphire only the orientation of the dewetted particles was studied, because the dewetting progressed too fast to leave a continuous film with grains behind and no additional samples with a higher coverage were created. The EBSD maps (Figure 4.6) show no single dominating orientation for gold and the pole figures (Figure 4.7) for the 111 lattice planes have rings of intensity with an even spacing around the center spots. This means the Au films and particles have a (111) out-of-plane orientation. In addition to the fiber structure, PF of samples heated in nitrogen and hydrogen/argon sometimes show spots with a higher intensity, but they are weak and they are hardly visible in the scatter plots (Figure C.1). These spots could indicate a preferred orientation of Au on sapphire, which would be $Au(111)[110]|Sapphire(0001)[10\bar{1}0]$, but the signal is too weak for a definitive answer.

Complementary to the PF, Figure 4.8 shows the IPFs that make new features in the texture-evolution observable. It shows the EBSD signal from the Au films and particles to split in two distinct curves, that each correspond to one of the $\Sigma 3$ twins. The splitting is caused by a misorientation of the Au [111] axis relative to the normal of the sapphire (0001) plane of $+2°$ for one twin half and $-2°$ of the other. In the nitrogen and the higher temperature hydrogen/argon samples, which showed further progress in dewetting, the splitting disappears again. This x-direction is parallel to the $[10\bar{1}0]$ direction of the sapphire substrate in all displayed IPFs. The

IPFs also show the kinetic differences for the atmospheres, the nitrogen samples are in distinct curves at the lowest temperatures, while hydrogen/argon and vacuum have a higher distribution.

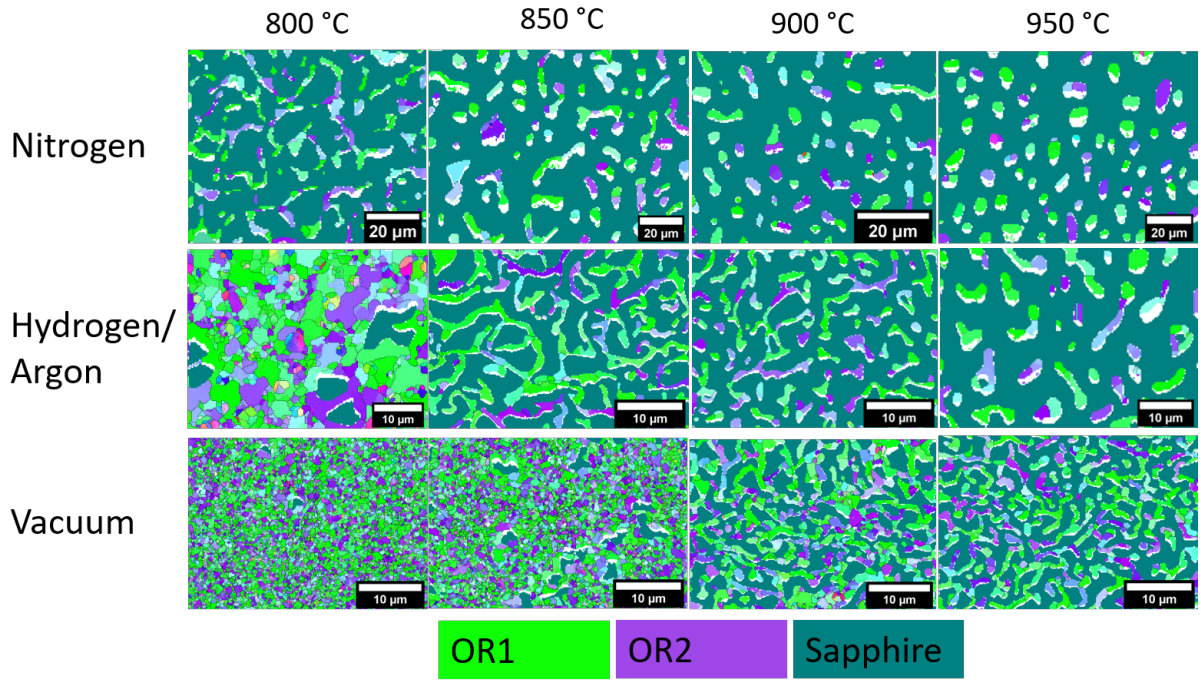

Figure 4.6: Inverse pole figure maps in the x-direction of samples with Au on sapphire that were annealed in different atmospheres for 2 minutes. A tendency towards preferred orientations is visible with OR1 light green, OR2 purple and the sapphire substrate is dark green

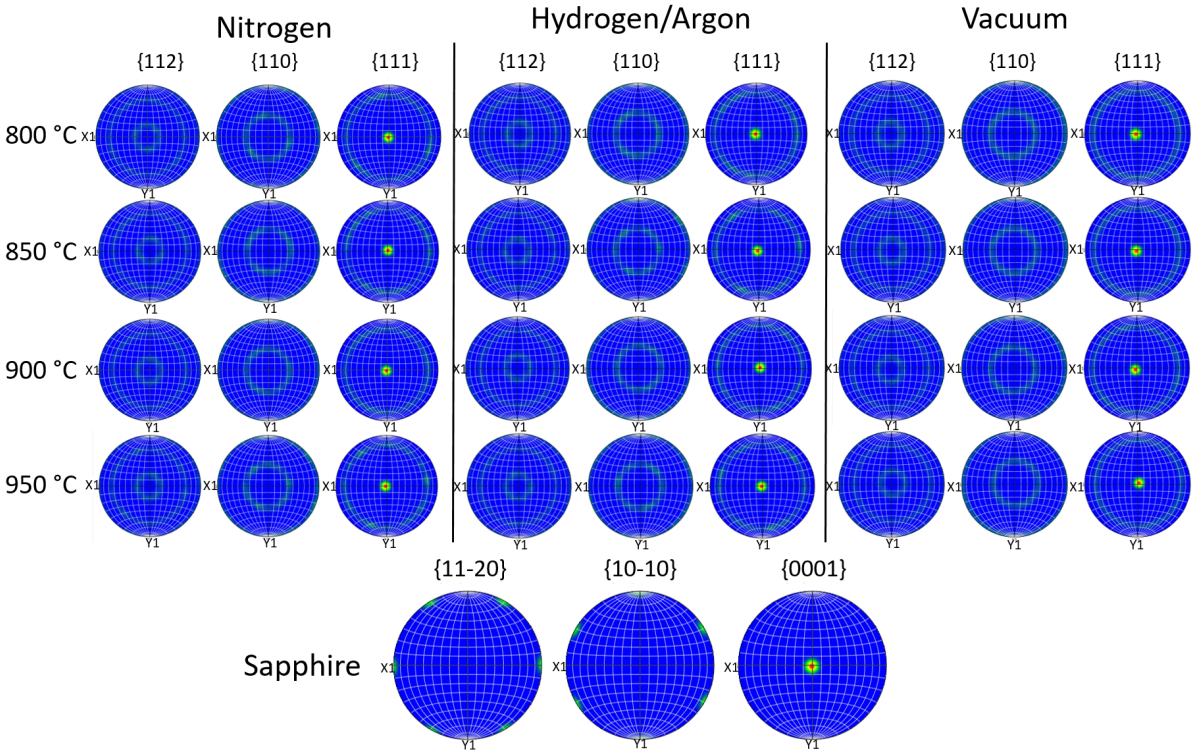

Figure 4.7: Pole figures for samples of Au on sapphire that were annealed in either nitrogen, hydrogen/argon or vacuum for 2 minutes at different temperatures. The bottom PF is of sapphire.

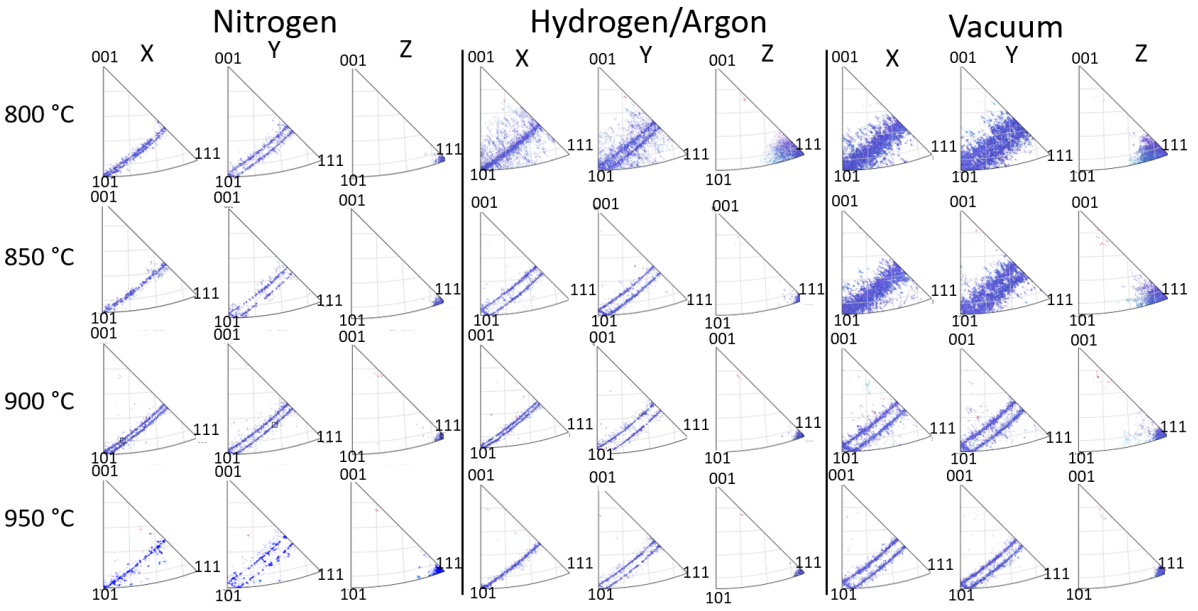

Figure 4.8: Inverse pole figures of Au on sapphire annealed in nitrogen, hydrogen/argon and vacuum. The curve in the x- and y-direction IPF stems from the random in-plane orientation, but a splitting of the signal in two distinct curves suggest a slight misalignment by $\pm 2°$ from the out-of-plane direction of Au(111) to the sapphire (0001) planes for each half of the twinned grains. The splitting in the x-direction, which is parallel to the sapphire $(10\bar{1}0)$ plane, focuses into a single line for samples with a higher degree of dewetting.

4.2 Verifying ZnO properties

The precise material properties of ZnO are important to explain the dewetting behavior and texture evolution phenomena that are discussed in Chapter 5. In addition to values taken from literature, own measurements are performed for the lattice constants and the substrate polarity. The lattice parameters of the ZnO wafer pieces is easy to determine by XRD. An in-plane and an out-of-plane measurement is done with CuKα1 x-rays at a wavelength of 1.5406 Å and the lattice spacing is calculated with equations 3.2 and 3.4 from the peak position of the (0002) crystal plane at 34.42° (Figure 4.9) and (20$\bar{2}$0) at 66.44° (Figure 4.10). The results of a=3.25 Å and c=5.21 Å confirm the lattice parameters supplied by CrysTec. For the Au (220) peak at 64.44° a lattice parameter of a=4.09 Å is calculated with equation 3.3 which is in good agreement with literature values of a=4.07 Å [47]. When the lattice constant is calculated from SAED images (Appendix A) the spacing is very close but slightly underestimated, which might simply stem from insufficient calibration.

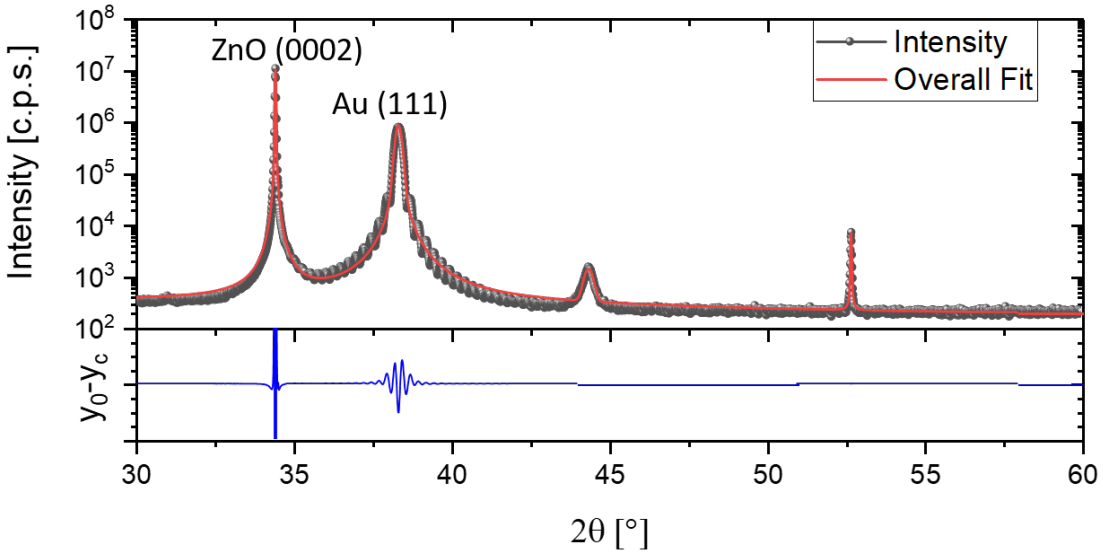

Figure 4.9: XRD θ-2θ plot of a Zn-ZnO substrate and Au on top with the ZnO (0002) peak at 34.42° and the Au (111) peak at 38.32°. The blue curve in the lower section shows the error between the measured intensity and the fit.

In this thesis the most important sample characteristic is the orientation of the ZnO crystal and the position of the polar surfaces. For the Zn-ZnO substrate CBED is performed and the resulting diffraction discs are compared to simulations from the program JEMS. For the Zn-ZnO sample the simulated disc of 70 nm thick ZnO fits very well to the experiment (Figure 4.11) and lines up with the thickness measured during the FIB lift-out. For the O-ZnO substrate the CBED discs were not of suitable quality to determine the polarity, so HRSTEM images (Figure 4.12) with an applied average background subtraction filter [53] are used instead. The contrast is low for the oxygen atoms in the HAADF image, but in the ABF image the zigzag structure of this (11$\bar{2}$0) orientation is visible and the substrate polarity is confirmed with the overlayed

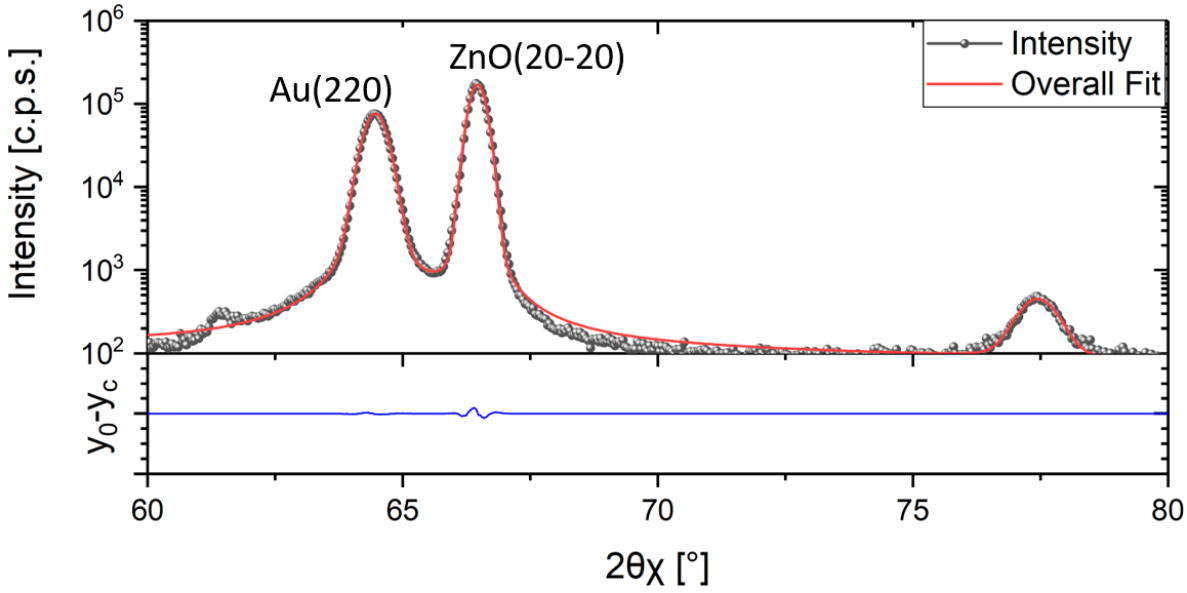

Figure 4.10: XRD θ-$2\theta_\chi$ plot of a Zn-ZnO substrate and Au on top with the ZnO($20\bar{2}0$) peak at 66.44° and the Au(220) peak at 64.44°. The blue curve in the lower section shows the error between the measured intensity and the fit.

ZnO lattice.

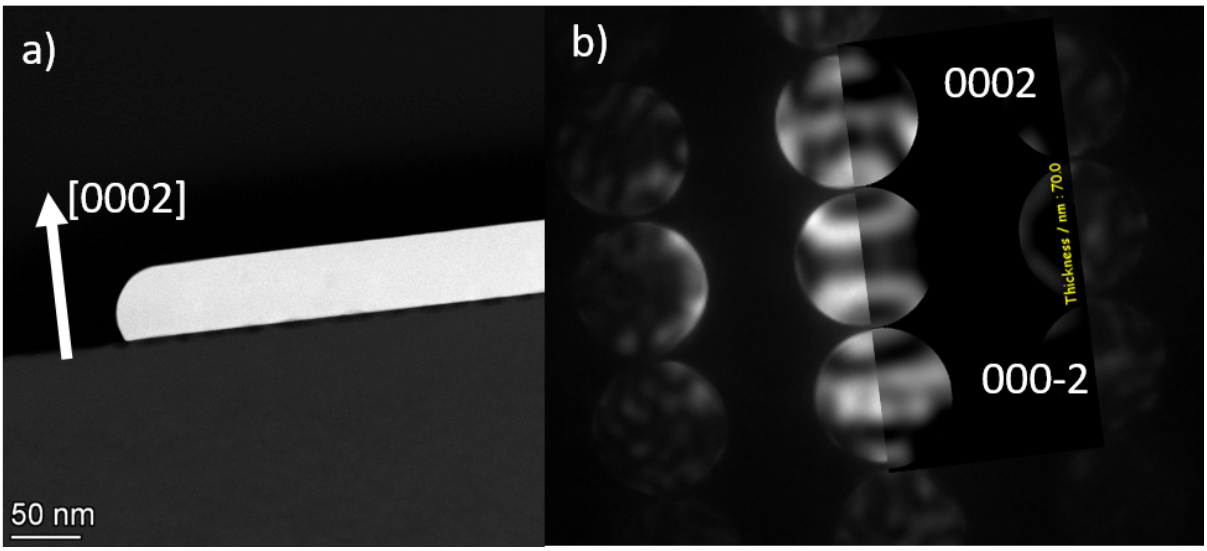

Figure 4.11: a) HAADF image of the Zn-ZnO cross-section with a partly dewetted Au film on top, the arrow shows the ZnO orientation of the substrate as determined by CBED b) CBED diffraction discs of the Zn-ZnO cross-section overlayed with simulated discs

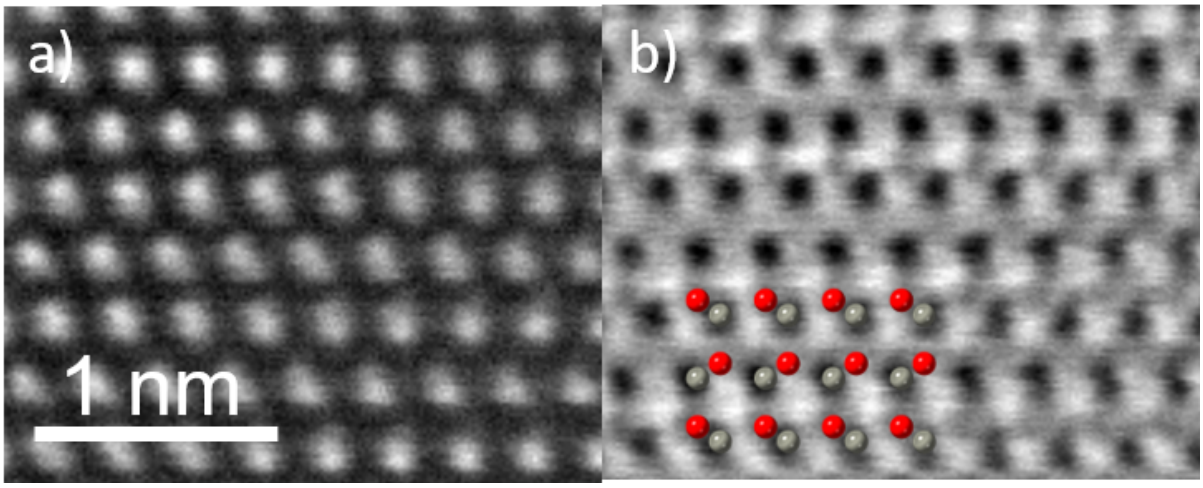

Figure 4.12: a) HAADF image of a O-ZnO substrate, the white spots stem from zinc atoms b) ABF image with zinc atoms appearing dark and oxygen atoms bright. The STEM image is overlayed with a ZnO lattice in the $(11\bar{2}0)$ zone-axis, the oxygen atoms are red and zinc atoms are grey, the scale bar is valid for both images

4.3 ZnO Degradation

As the initial plan called for gold nickel films and particles on ZnO several samples were prepared by the usual ebeam evaporation and annealing. This did not result in the formation of AuNi solid-solution particles with a desired atomically sharp interface between particle and substrate. The reason for this is a reaction of Ni with ZnO which caused a degradation of the substrate surface. This reaction leaves a porous NiZnO surface (Figure 4.13) behind. This is confirmed by EDX maps (Figure 4.14) showing that the dewetted structure only consists of Au signal, while Ni is distributed over the whole wafer.

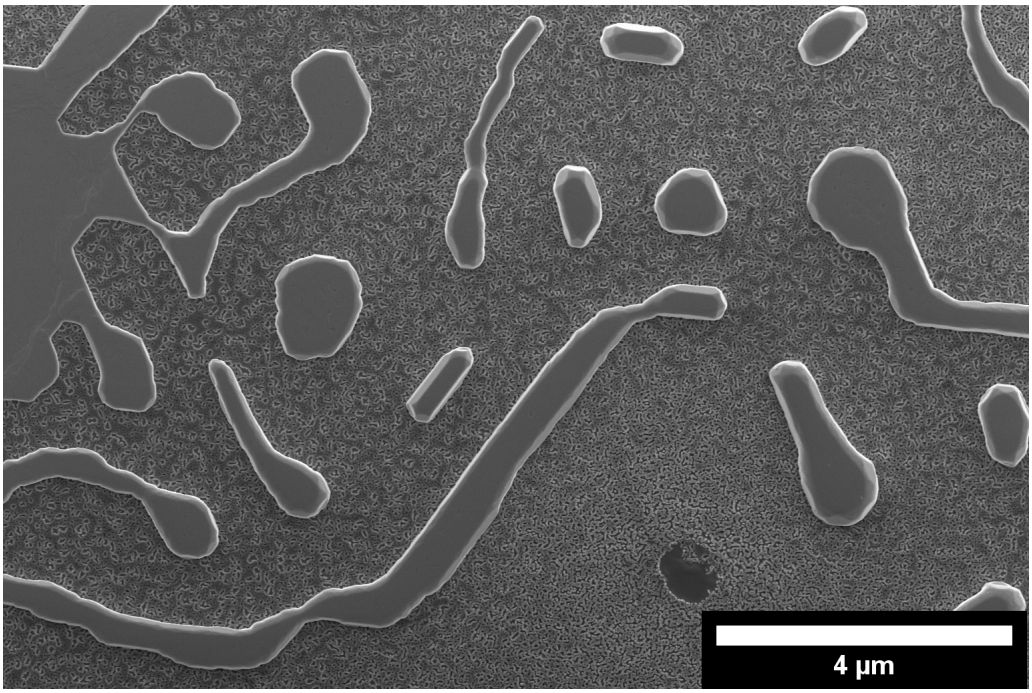

Figure 4.13: Dewetted Au on ZnO that shows degradation from a reaction with Ni, which gives the surface a porous appearance

However the degradation is not only limited to films containing nickel. It was planned to determine the interface energy from the Winterbottom shape of equillibriated Au particles on both ZnO sides. For this 40 nm Au films were annealed at 900 °C for 1 hour. During imaging in the SEM it is immediately clear that the substrate degraded (Figure 4.15), especially around the Au particles, with holes that are several micrometers deep. This degradation behavior is known from the literature [54] and also present in a reduced capacity in the Au on O-ZnO samples heated at 950 °C (Figure 4.16). Luckily this effect is not observed in samples annealed at lower temperatures and short times and there is no mixing detected by EDX for both the Zn-ZnO (Figure 4.17) and the O-ZnO substrate (Figure B.1).

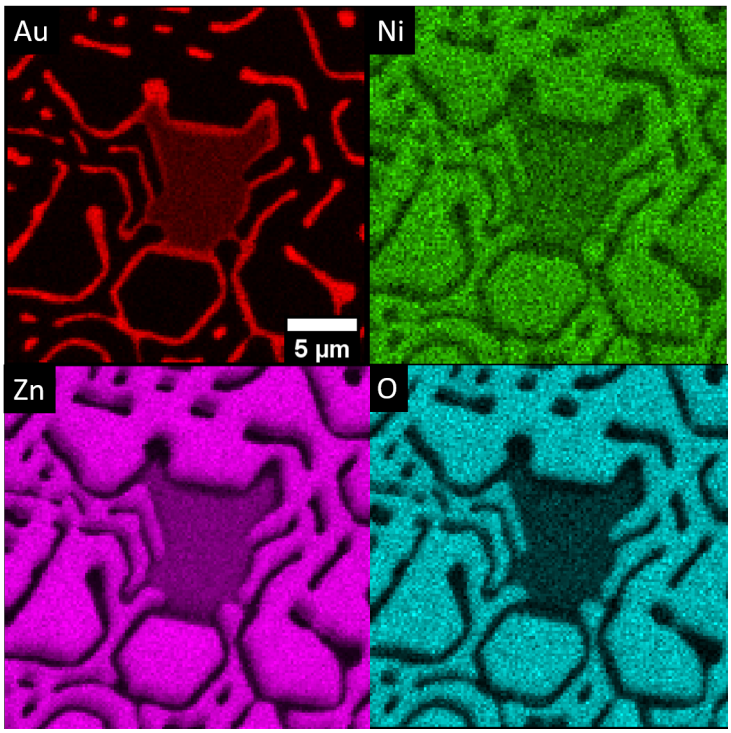

Figure 4.14: EDX map of a 20 %Ni 80 %Au film on ZnO, where the Ni reacted with the ZnO and the Au dewetted

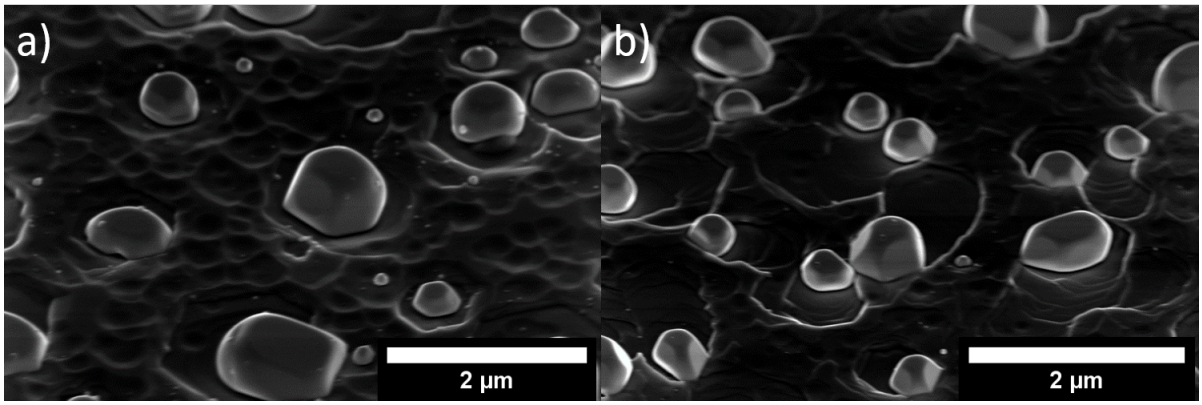

Figure 4.15: Au on a) Zn-ZnO and b) O-ZnO. The samples where annealed at 900 °C for 1 h and both samples show a degraded ZnO substrates, with pits that appear deeper on the O-ZnO wafer.

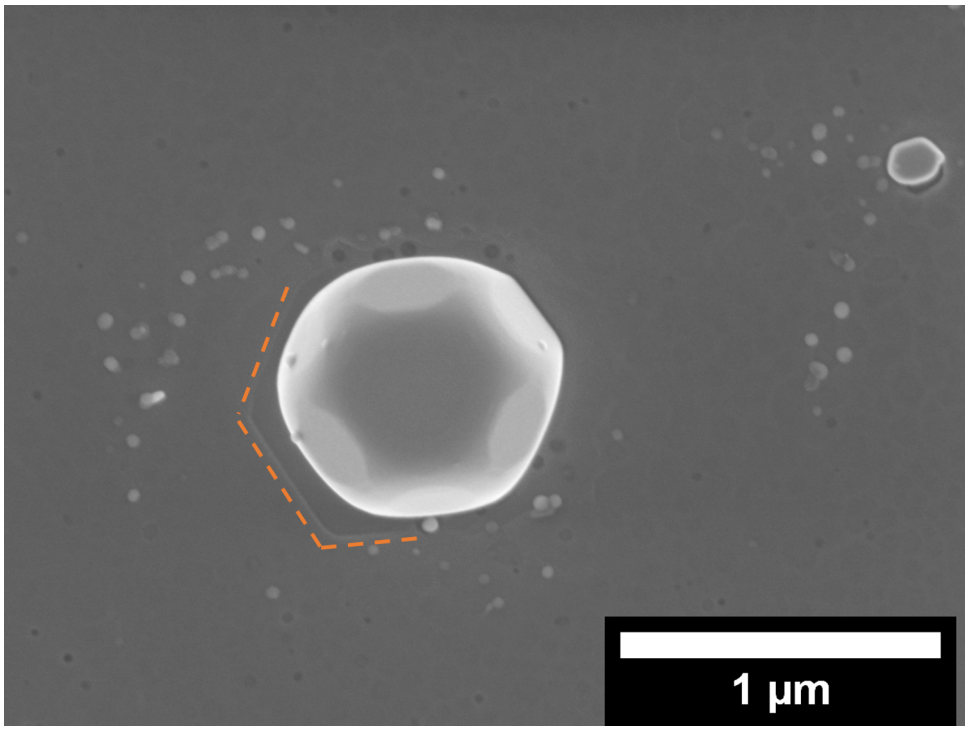

Figure 4.16: An Au particle on O-ZnO after annealing a film at 950 °C for 2 minutes. The particle is not yet in the equilibrium shape and sits in a small pit (marked by orange outlines), which is a sign of ZnO degradation.

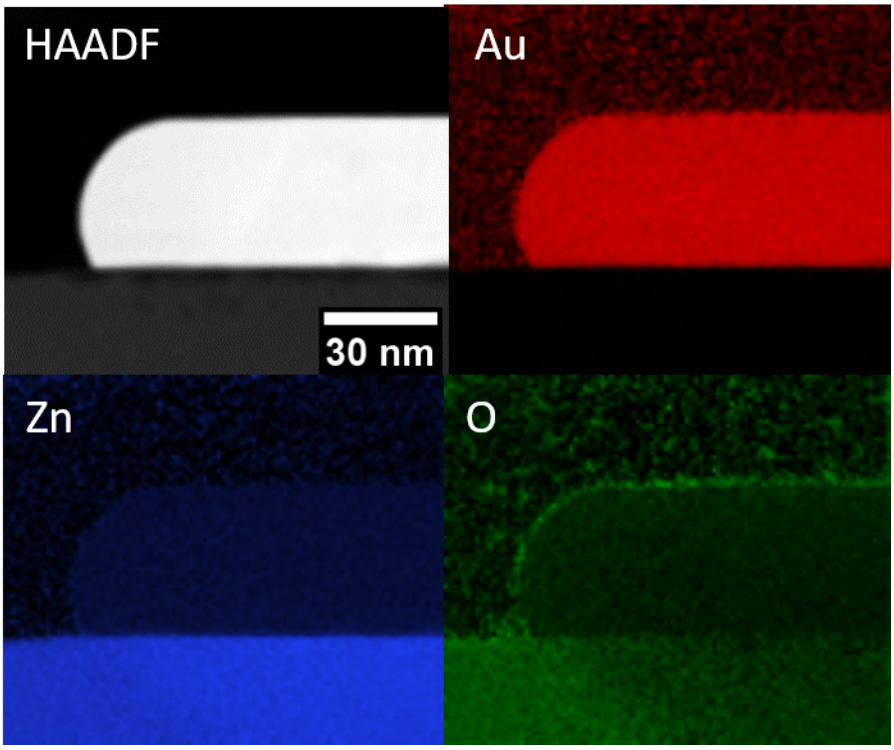

Figure 4.17: STEM EDX of Au on Zn-ZnO annealed at 800 °C for 2 minutes, no mixing of the Au and ZnO is observed. The peaks from outside the Au film and the ZnO substrate stem from random noise.

4.4 Dewetting of gold on ZnO

4.4.1 Early Stages of Dewetting

In this section the early stages of dewetting refers to the time when individual holes in the Au thin film are still distinguishable.
The Au film on Zn-ZnO show a large number of cracks formed along grain boundaries (Figure 4.18), this is likely an artifact of the high cooling rate and the different thermal expansion factors of Au and ZnO. If they would have formed at high temperatures it would probably increase the dewetting rate at these points by a lot, which is not observed and the cracks are therefore neglected in the further analysis.

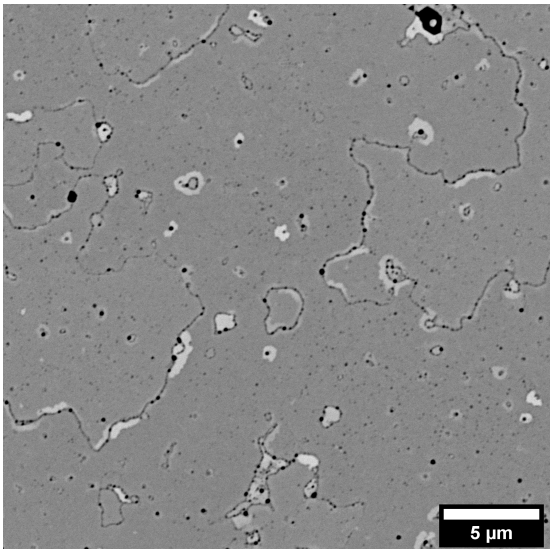

Figure 4.18: Cracks in the Au film along the grain boundaries with small holes at the grains and in the film, the Au/Zn-ZnO sample was annealed at 800 °C for 2 minutes in nitrogen.

In the Zn-ZnO samples annealed in vacuum triangles are observed (Figure 4.19). The triangle edges are along the ⟨110⟩ directions and they are in two opposing orientations. Also from EBSD data it can be seen that the triangle direction depends on the twin grain it is placed in. In the center of the holes a singular Au particle is left behind.

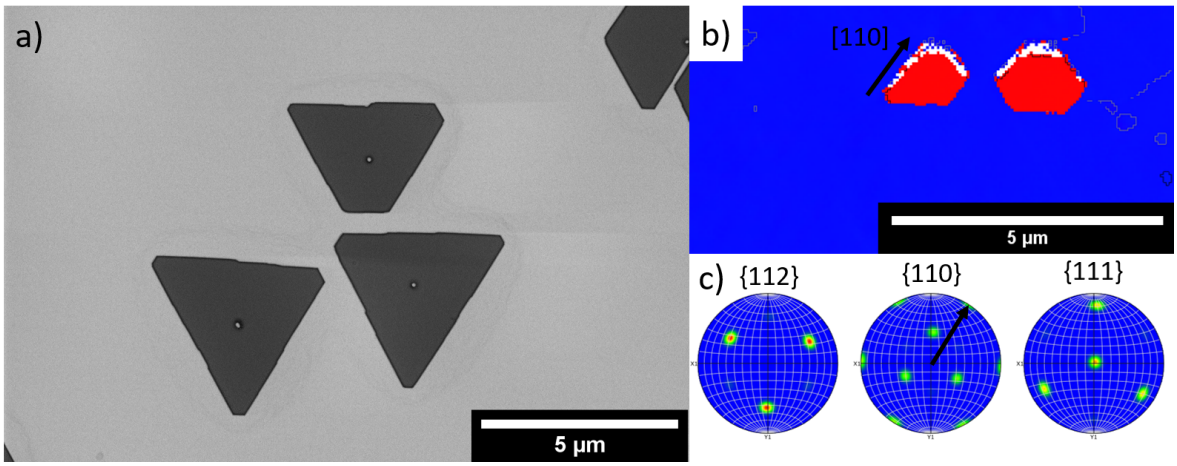

Figure 4.19: a)The Au film on Zn-ZnO shows triangular holes with the same orientation and a Au particle at their centers after annealing at 850 °C for 2 minutes in vacuum. b) An EBSD map of the Au film (blue) on Zn-ZnO (red) reveals the orientation or the triangles and c) the PF confirms that the edges are along the ⟨110⟩ directions.

4.4.2 Dewetting rate

For Au on O-ZnO at the shorter times and lower temperatures a mostly continues film is observed with some smaller holes (Figure 4.20). These steadily grow larger with increasing annealing time and temperature. From the 850 °C to the 900 °C annealing series a sudden shift in the dewetting advancement is obvious from the covered area graph (Figure 4.21) and the images (Figure 4.20). In these samples, only wires and particles are present and at the highest time and temperature only particles are left. At higher magnifications it is determined that the particles from the 950 °C and 2 minutes sample (Figure 4.16) are not yet in their equilibrated state, as they have no developed Winterbottom shape.

Au films on Zn-ZnO show the slowest dewetting behavior of the substrates tested in this thesis. Au fingers remain even at the highest times and temperatures (Figure 4.22) with no visible evidence for particle formation. At the shorter times and low temperatures a mostly continues film with small holes is observed. The analysis of the covered area (Figure 4.23) reveals the gradual progression of dewetting in this annealing series, without the major jumps that were observed in O-ZnO. The distinct triangular shape of the dewetted areas, that rip long channels into the Au film on Zn-ZnO is also very different to the more isotropic hole growth on O-ZnO.

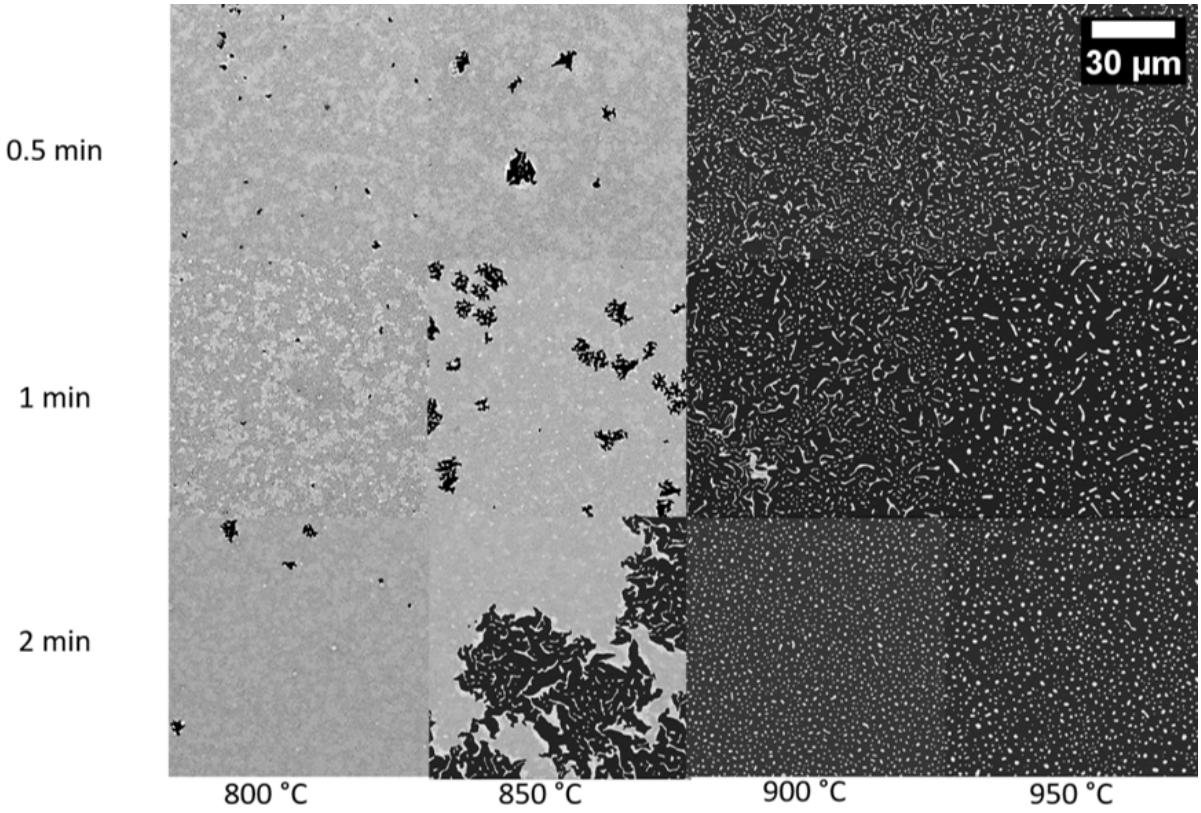

Figure 4.20: Au on O-ZnO heated at different times and temperatures with constant nitrogen flow. At higher temperatures and longer annealing times the dewetting has progressed further. In these BSE images the ZnO substrate is black and the Au shows fluctuations in the grey values, which can stem from different grain orientations.

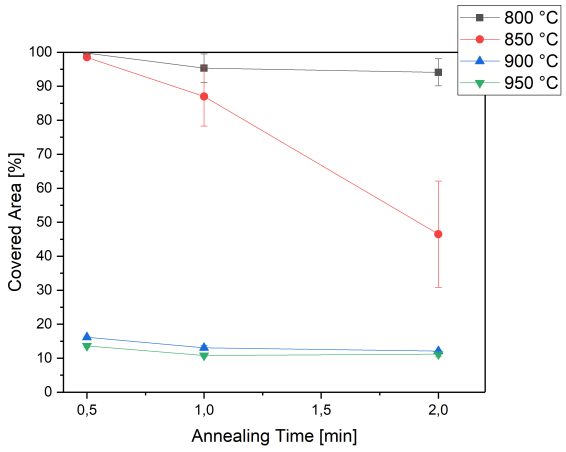

Figure 4.21: The area of the O-ZnO substrate still covered by gold after dewetting at temperatures between 800 °C and 950 °C in constant nitrogen flow. At the higher temperatures the dewetting progresses much faster.

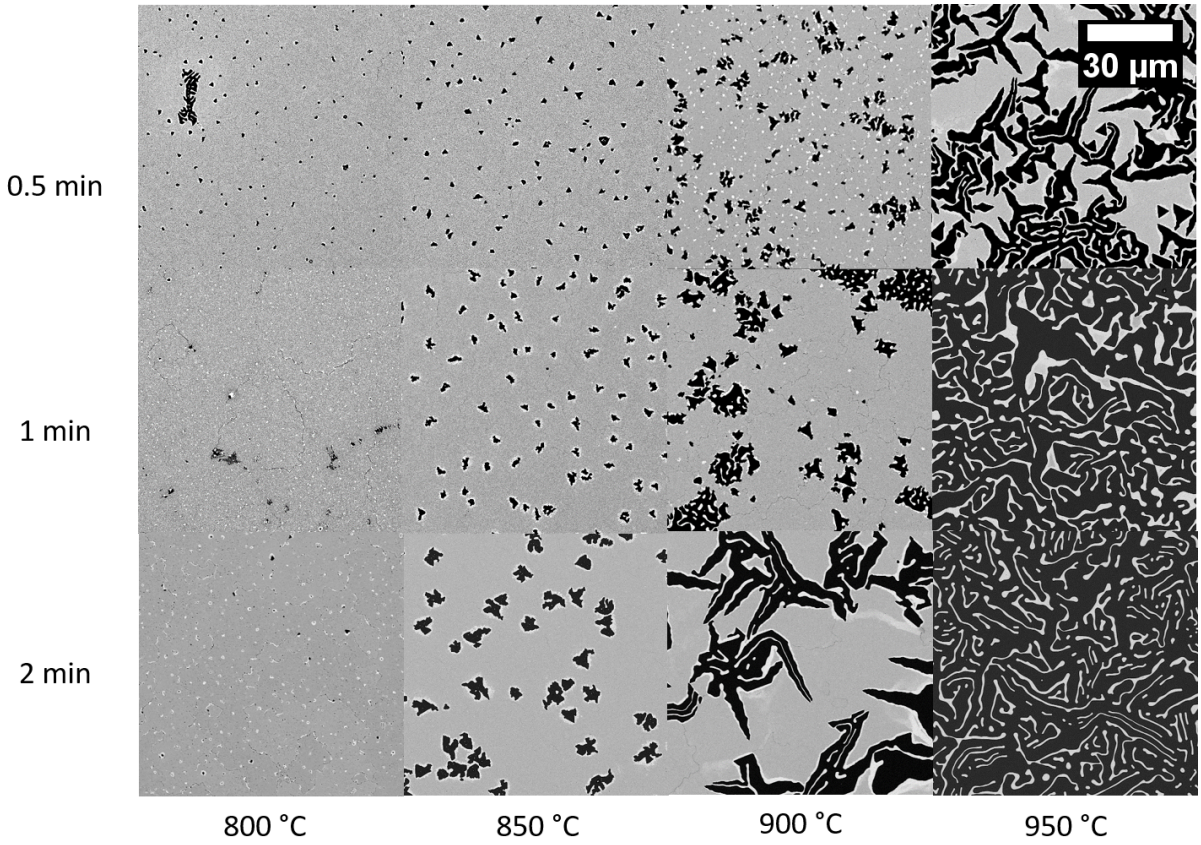

Figure 4.22: Au on Zn-ZnO heated at different times and temperatures with constant nitrogen flow. The larger holes at higher temperatures are a result of the faster dewetting. In these BSE images the ZnO substrate is black, the gold film on top is in grey.

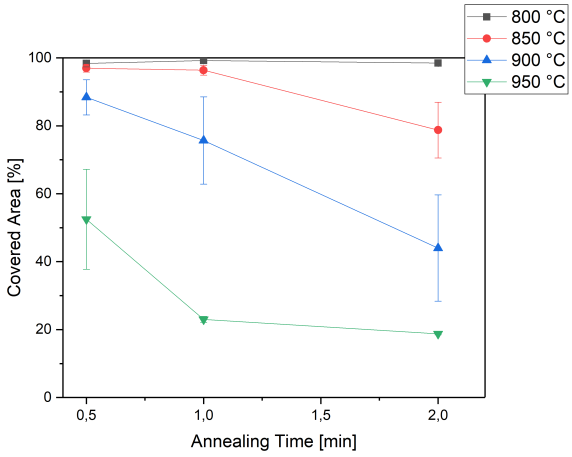

Figure 4.23: The area of the Zn-ZnO substrate still covered by gold after dewetting at temperatures between 800 °C and 950 °C in constant nitrogen flow. At higher temperatures the Au films dewett quicker, but the overall dewetting speed is slower compared to the films on O-ZnO.

4.4.3 Influence of Atmosphere

In this measurement series, Au films on Zn-ZnO and O-ZnO substrates are heated in vacuum and compared to the previous nitrogen annealed samples. The hydrogen/argon mixture used for sapphire is skipped here, because the hydrogen would react with ZnO (chapter 4.3).
Samples annealed in vacuum (p <10^{-4} mbar) show lower dewetting kinetics than in nitrogen atmosphere. On the O-ZnO substrates (Figure 4.24) the hole growth at 850 °C is notably smaller than in vacuum and at 900 °C some small areas with continuous Au film remain. At the 950 °C the samples in vacuum and nitrogen have the same covered area (Figure 4.25), but the vacuum sample has not yet reached a full particle state.

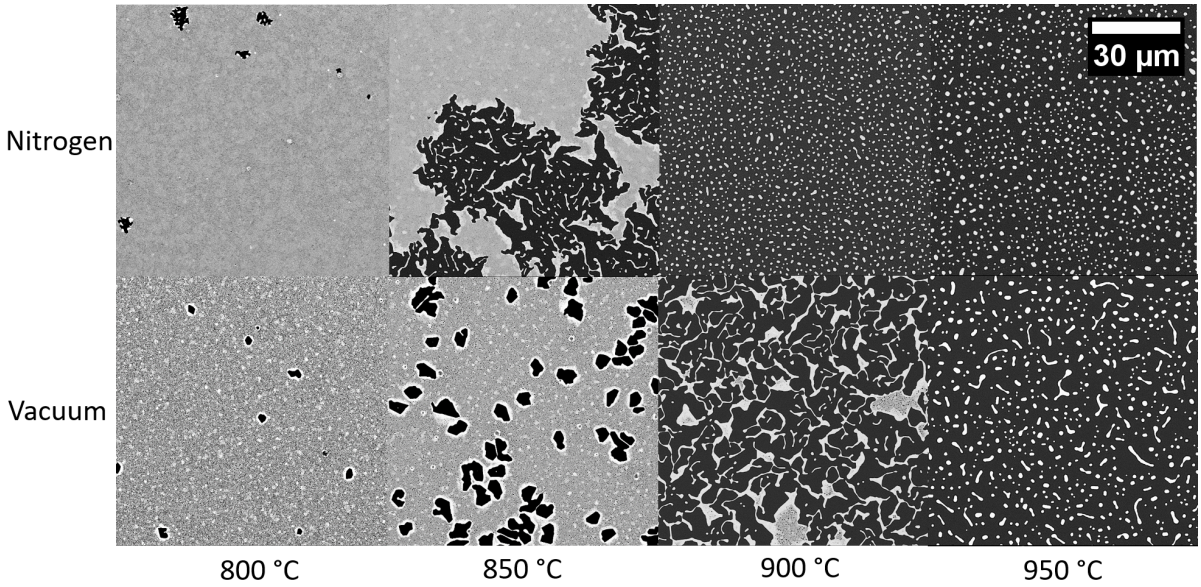

Figure 4.24: Au on O-ZnO annealed in nitrogen and vacuum atmosphere for 2 minutes at different temperatures. In vacuum at the same temperatures the holes in the Au film are smaller and the dewetting progresses slower.

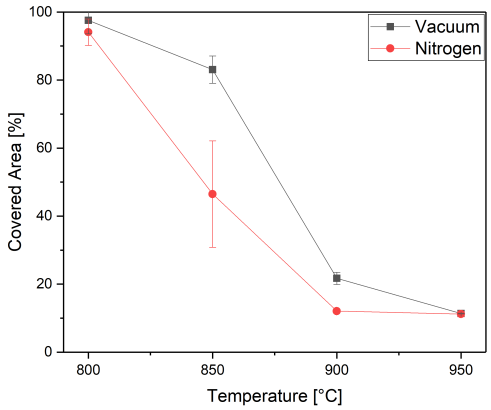

Figure 4.25: The area of the O-ZnO substrate covered with gold after annealing for 2 minutes in nitrogen and vacuum. The dewetting speed in vacuum is slower at the same temperatures.

The Au films on Zn-ZnO have a very similar dewetting rate in both tested ambient conditions

which is reflected by the covered area graph (Figure 4.27) being closely together. In the vacuum annealed films holes with a triangular shape appear (Figure 4.26) at 800 °C and they are also present in the 850 °C sample with a bigger size. At even higher temperatures of 900 °C the holes look the same again in nitrogen and vacuum, with long trenches with a triangular symmetry.

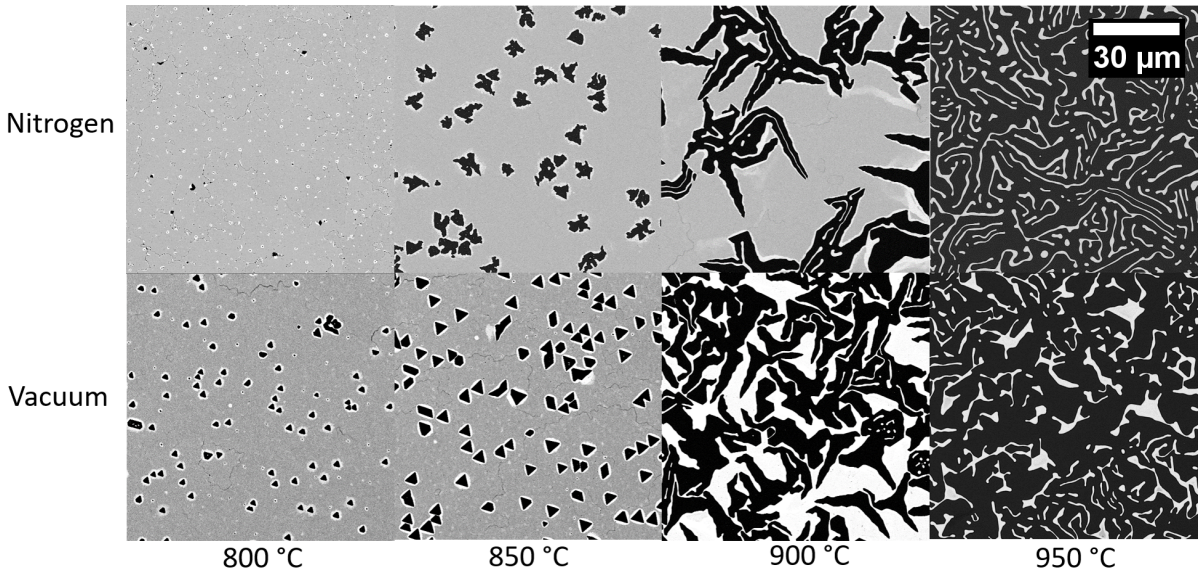

Figure 4.26: Au on Zn-ZnO annealed in nitrogen and vacuum atmosphere for 2 minutes at different temperatures. In vacuum the dewetting is anisotropic and triangular holes form.

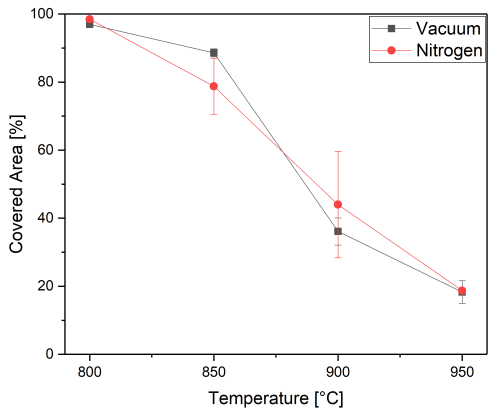

Figure 4.27: The area of the Zn-ZnO substrate covered with gold after annealing for 2 minutes in nitrogen and vacuum. The dewetting rate for both atmospheres is similar.

4.5 Texture- and microstructural evolution of Au on ZnO

4.5.1 Texture evolution on polar ZnO

The orientation of the gold film on both the Zn-ZnO and the O-ZnO side is measured by EBSD mapping at 30 kV acceleration voltage. The as-deposited films on both ZnO sides (Figure 4.28)

have a lot of zero solutions, which can be attributed to small grain sizes that are difficult to index with the resolution of EBSD. The grains that could be indexed show a strong (111) out-of-plane orientation. The in-plane orientation differs much more in the samples. Samples measured in the as-deposited state have a slight tendency to the Au[110] ∥ ZnO[11$\bar{2}$0] orientation relation with the corresponding Σ3 twins at a 60° rotation for both ZnO sides (Figure 4.28), many of the remaining grains have a random in-plane orientation, which can be seen from the signal between the high intensity spots in the pole figures and in the scatter plots (Appendix C.2 and C.3).

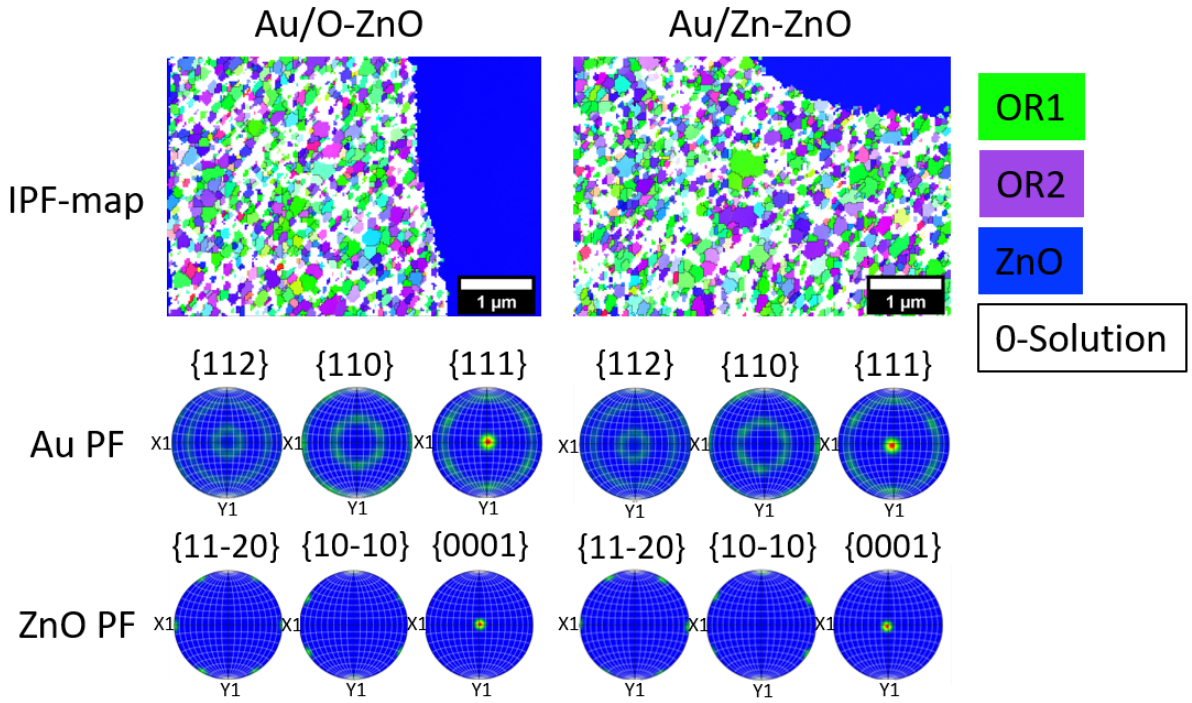

Figure 4.28: The results of EBSD measurements of Au in the as-deposited state on O-ZnO and Zn-ZnO, with a x-direction IPF map with OR1 in green, OR2 in purple and the ZnO substrate in blue and the corresponding pole figures of Au and ZnO. The difference in surface polarity for ZnO is not detected in the EBSD.

Figure 4.29 shows the EBSD maps of the annealed samples on the different ZnO sides. While on both sides the expected out-of-plane orientation of (111) is present, significant differences are found regarding the in-plane orientation. At the 600 °C samples the grain size and orientation relations are relatively similar, with most Au grains being in either OR1 or OR2. At 800 °C the Zn-ZnO shows an Au film with almost exclusive OR1 in the form of large twinned grains. The OR stays the same for the higher temperatures, where dewetting sets in and more of the ZnO substrate is revealed. The quick transformation into a almost purely OR1 oriented film is also observed in the pole figures of the 30 seconds (Figure C.4) and 2 minutes (Figure 4.30) samples. For these samples, the six high intensity points in the {111} PF are due to the twinned grains of one OR.

The Au films on the O-ZnO substrates behave very differently to Zn-ZnO at the temperature of 800 °C and beyond. In the EBSD images (Figure 4.29) it can be seen that, although OR2 is dominating, the small grains are oriented in both ORs even when the film is dewetted enough

to transform into particles. This is also reflected in the {111} PF where a mixture of two ORs with a 30° orientation to each other and their respective twins at 60° are shown.
Figure 4.31 shows the inverse pole figures of the thermal processed samples. At lower temperatures up to 600 °C, a (111) out-of-plane orientation is already emerging, however with a relatively wide dispersion. In addition, due to the continuous line in X- and Y-direction, a so-called fiber texture can be found, which also shows a strong broadening. For the Au on O-ZnO samples (Figure 4.31) a curve can be seen, which would signal a fibre texture, but a tendency towards the preferred orientation can be observed at 800 °C in the Y-direction due to the high concentration of points at the 110 orientation. The splitting starts at the 800 °C sample but only in the Y-direction (parallel to ZnO[11$\bar{2}$0]). The X-direction (parallel to ZnO[10$\bar{1}$0]) stays mostly in one single, albeit spread out line. For the Au on Zn-ZnO the 800 °C sample shows a splitting in both the X- and Y-direction, but at the 850 °C and beyond the X-IPF focuses into a single line. Additionally an in-plane orientation is seen in the IPFs for both ZnO sides.

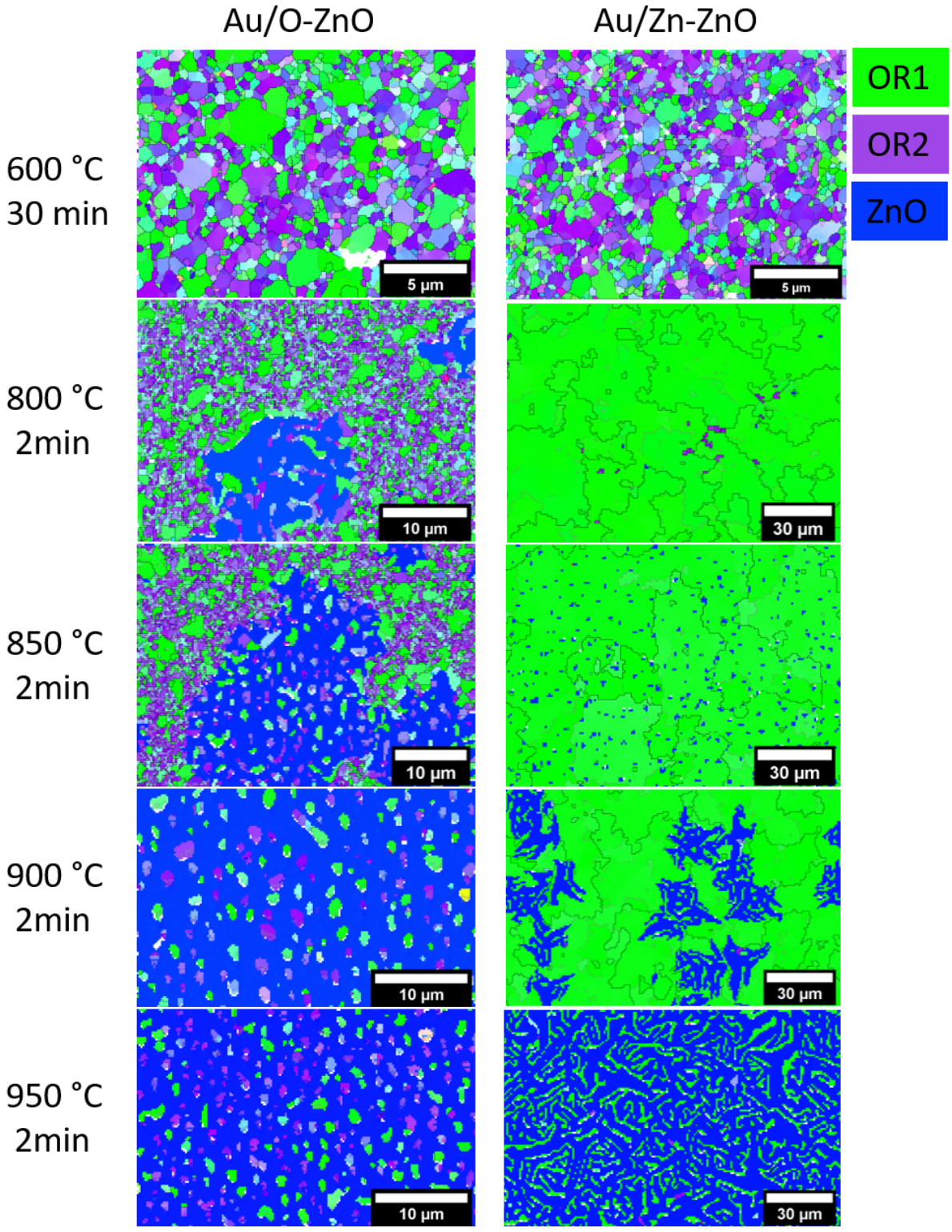

Figure 4.29: X-direction inverse pole figure maps of samples with Au on O-ZnO and Zn-ZnO that were annealed at tempertures from 600 °C to 950 °C, OR1 is in green, OR2 in purple and the ZnO substrates are in blue

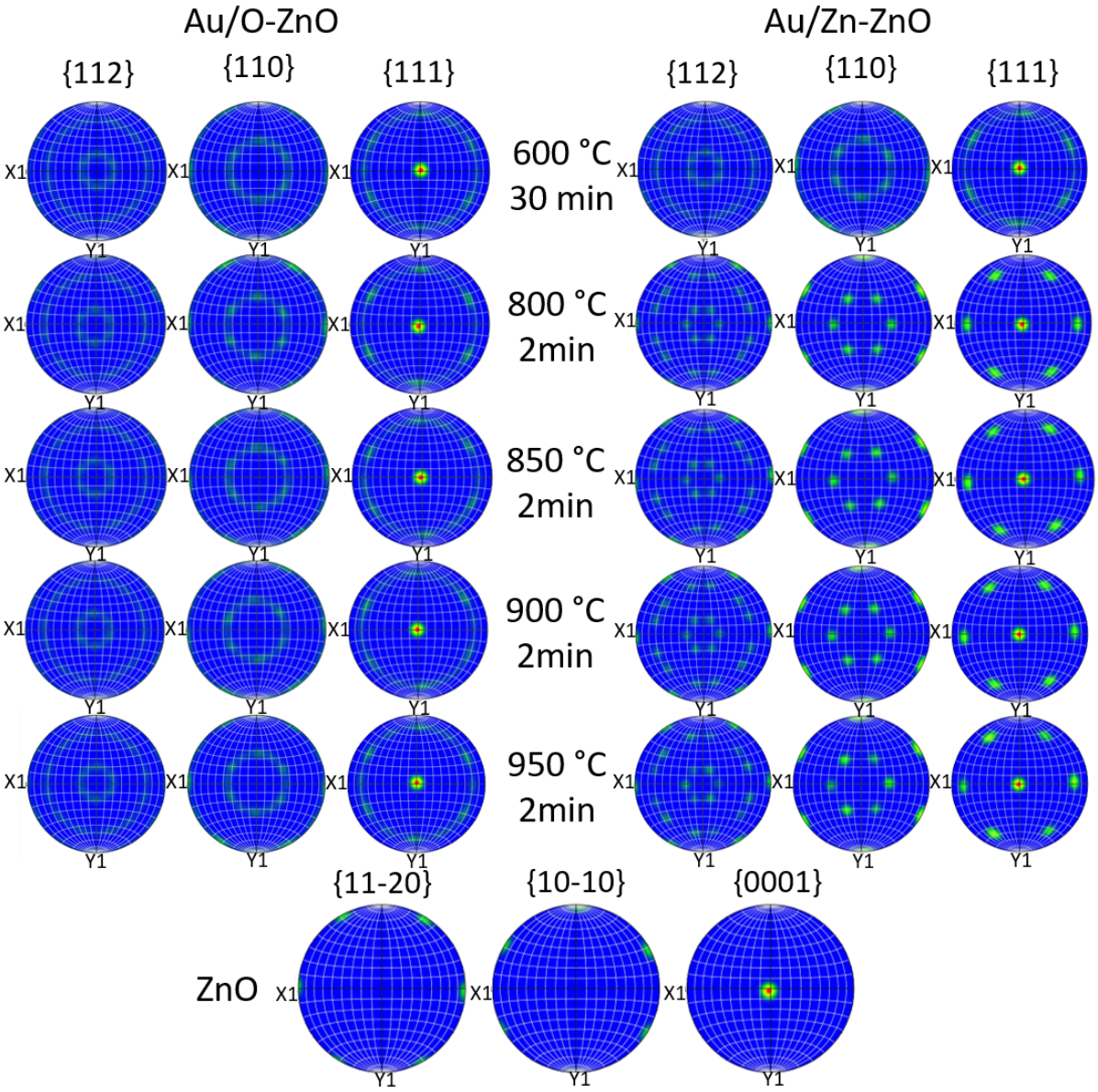

Figure 4.30: Pole figures of Au on O-ZnO and Zn-ZnO annealed at temperatures from 800 °C to 950 °C for 2 minutes

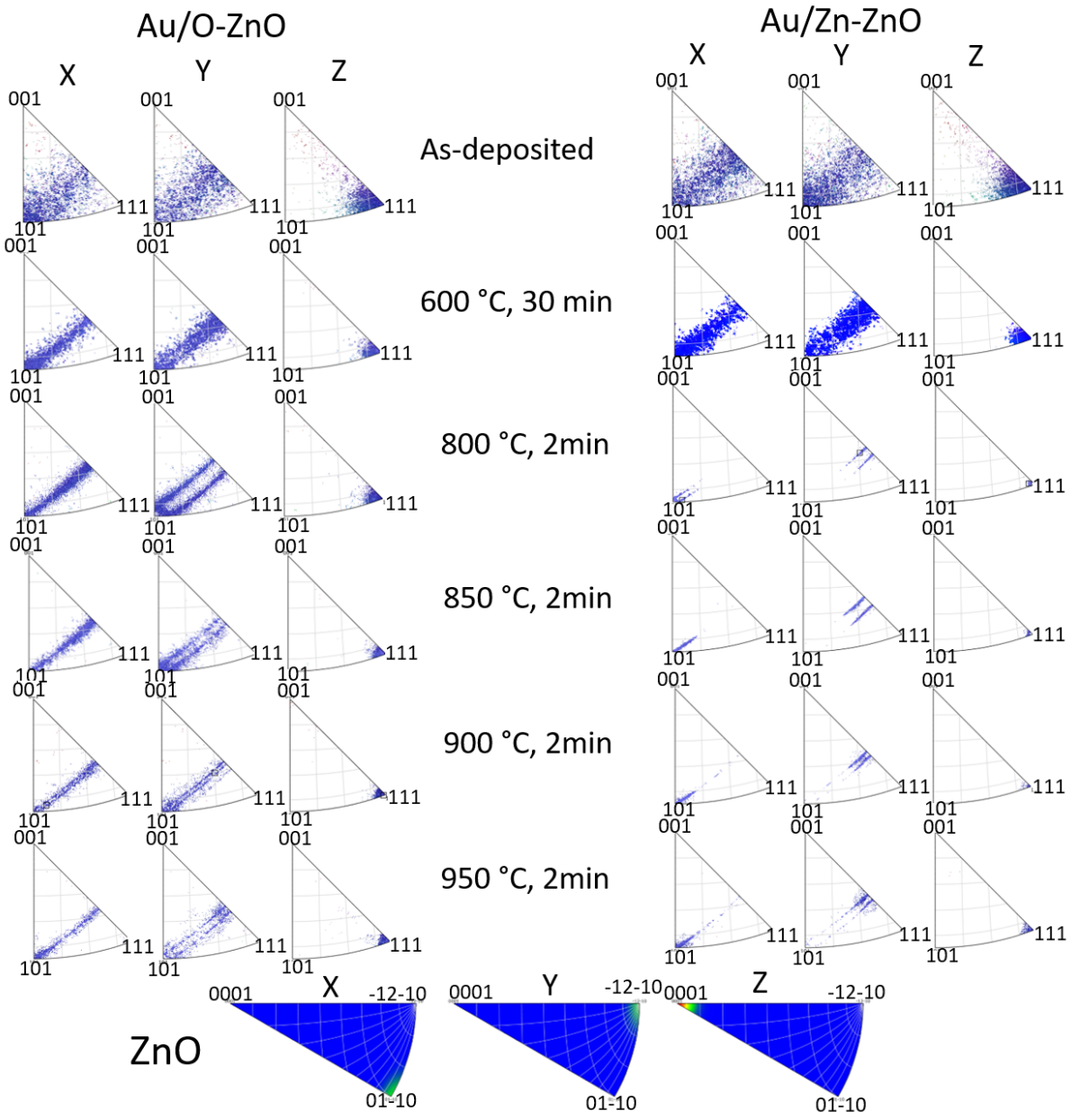

Figure 4.31: The inverse pole figures of Au on O-ZnO and Zn-ZnO from EBSD measurements. In the as-deposited state the (111) texture is visible, but has a high spread that vanishes at higher temperatures. At 800 °C and above a splitting in the y-direction IPF is obvious which correlates to a ±2° out-of-plane misorientation of twin grains. For the Zn-ZnO sample annealed at 800 °C an splitting is also observed in the x-direction.

4.5.2 Interface investigations of Au/Zn-ZnO and Au/O-ZnO

For imaging of the OR2 Au/O-ZnO interface (Figure 4.32) the FEI Titan Themis[3] 300 is used. Figure 4.32 shows a cross-section of the Au/O-ZnO interface of OR2 annealed in nitrogen atmosphere at 950 °C for 2 minutes. In the Fourier filtered image (Figure 4.32b) the misfit dislocations with a spacing of 2.33 nm are clearly visible after every 10 Au and 9 ZnO atoms. The Au atomic planes next to the dislocations are slightly bend, while those with the greatest distance remain straight throughout the interface area. A sample with a heat treatment of 800 °C, 2 minutes in vacuum was chosen for investigating the Zn-ZnO interface (Figure 4.33). In this cross-section in the $[10\bar{1}0]$ direction, the Zn and O atoms only show a very low spacing. Even when the HAADF detector would be able to provide a good enough contrast, the resolution would likely still be too low to image both atoms, the substrate atoms shown are therefore only Zn. In the Au film only the atoms directly adjacent to the Zn-ZnO surface are individually resolved, because the Au planes in the rest of the sample has an in-plane rotation of 2°. The Au layer at the interface has an oscillating contrast where some atoms appear brighter and larger than others. The spacing between the peaks of the high intensity areas is 4.75 nm or 19 Au and 29 ZnO atoms. Due to good resolution at the interface the distance between of the first layer of Au from the ZnO substrate are measured to be 2.6 Å in the high intensity and 2.7 Å in the low intensity areas. Further away the lattice distances of Au and ZnO (Table 4.1 quickly tend towards the bulk lattice spacing of Au(111)=2.4 Å and ZnO(0002)=2.6 Å. Misfit dislocations are not observed at this interface.

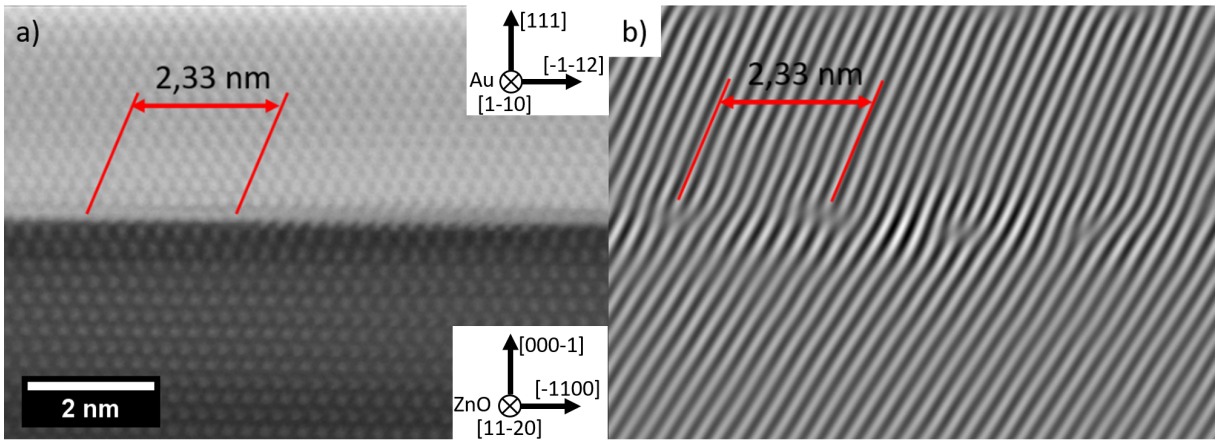

Figure 4.32: a) HRSTEM HAADF image of the Au/O-ZnO interface and b) with a Fourier filter applied that shows the misfit dislocations at a spacing of 2.33 nm

Table 4.1: Atomic layer spacing at the Au/Zn-ZnO interface measured from the HRSTEM image at the high intensity position

$Au^1 - ZnO^1$	$Au^1 - Au^2$	$Au^2 - Au^3$	$Au^3 - Au^4$	$Au^4 - Au^5$
2.6 Å	2.6 Å	2.6 Å	2.2 Å	2.4 Å
	$ZnO^1 - ZnO^2$	$ZnO^2 - ZnO^3$	$ZnO^3 - ZnO^4$	$ZnO^4 - ZnO^5$
	2.9 Å	2.9 Å	2.6 Å	2.6 Å

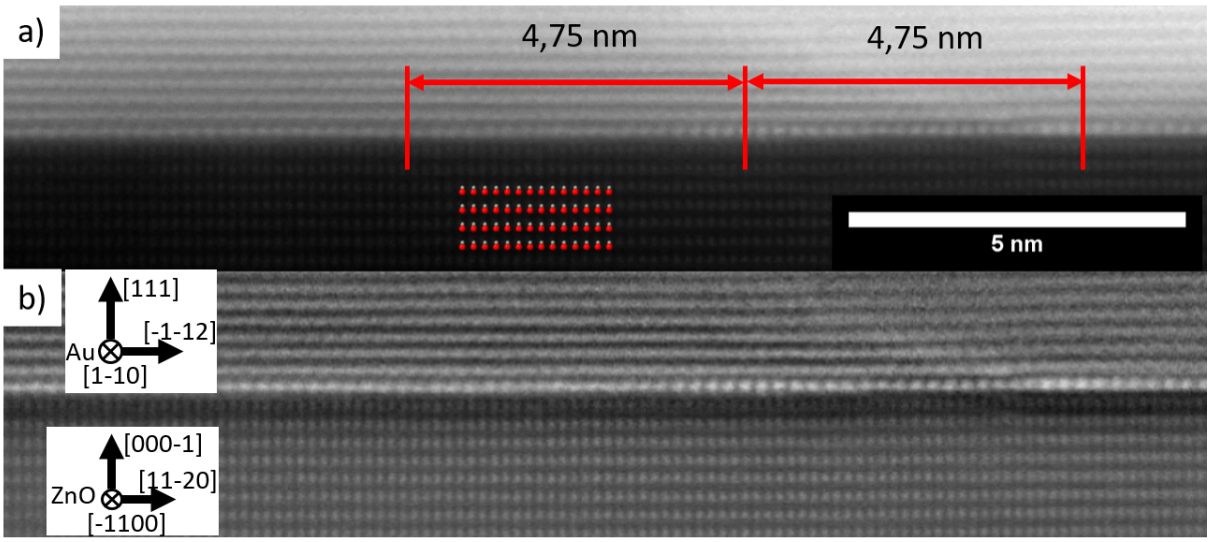

Figure 4.33: a) HAADF HRSTEM image of the Au/Zn-ZnO interface, b) the same image with a applied high pass filter. The first Au layer is in the zone axis and has a oscillating contrast with a spacing of 4.75 nm between the points of highest intensities. The following Au atoms layers have a $\sim 2^{\circ}$ in-plane rotation and therefore the individual atom columns are not resolved.

4.5.3 Grain growth on polar ZnO

The grain size is extracted from the EBSD data and shows that the growth rate is different for both ZnO substrates. Additionally a dependency on the orientation relation can be found (Figure 4.34). Until the temperature of 600 °C both ORs grow at roughly the same rate on both substrates. Starting somewhere between 600 °C and 800 °C, the OR1 grows much faster than OR2 on Zn-ZnO and at 850 °C the film exclusively consists of OR1. Here most of the OR1 grains are too large to fully fit into the scan area, the average grain size is therefore only a minimum value. For Au on O-ZnO the effect is similar. At 800 °C and 850 °C OR1 grows faster and has the larger grain size, but in contrast to Zn-ZnO the Au grains in OR2 continues to grow at 850 °C. Higher temperatures are not evaluated, because the dewetting of these samples turns the grains into particles. An issue with the grain size measurement stems from the limitations of the EBSD scan resolution. In the as-deposited samples many grains are smaller than the minimum spacing between scan points and are therefore not correctly detected which can be seen in the grain size distribution (Figure 4.35) that should be monomodal, but is cut of at.
The grain growth also comes with a change of the grain boundary types (Figure 4.36), because this is the main mechanism for the film to reduce energy at this stage [17]. In the faster growing Au grains on Zn-ZnO a substantial shift to more $\Sigma 3$ twin grain boundaries is obvious from 24 % at 600 °C to 92 % at 800 °C. For Au on O-ZnO the same effect is much less pronounced, with only a minimal shift from 19 % to 26 % towards more $\Sigma 3$ boundaries. The grain boundaries that are not $\Sigma 3$ are mainly between the twins of different ORs (Figure 4.37).

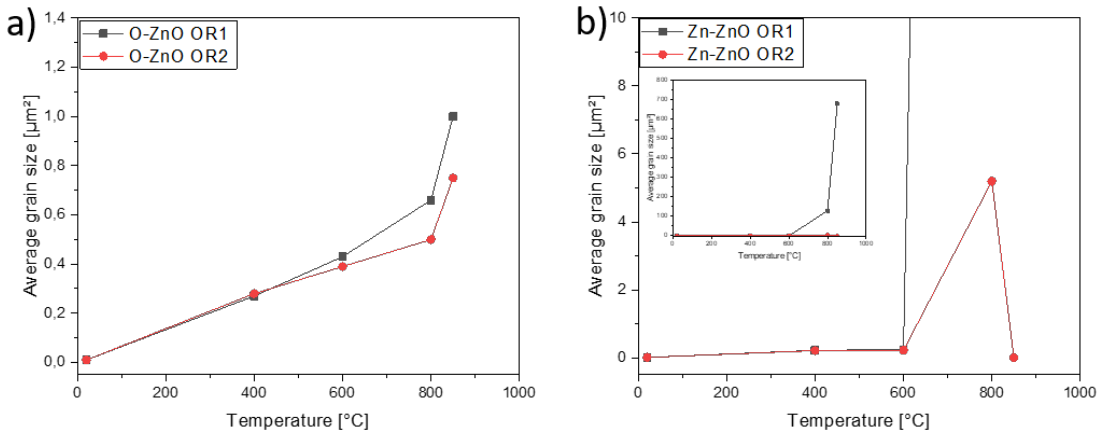

Figure 4.34: a) The grain size in the Au film on O-ZnO after annealing at 400 °C 2 hours, 600 °C 30 minutes, 800 °C and 850 °C for 2 minutes b) the same for Au on Zn-ZnO with an inset that shows a zoomed out version of the graph, in the 800 °C and 850 °C samples many grains are too large to fit into the scan area

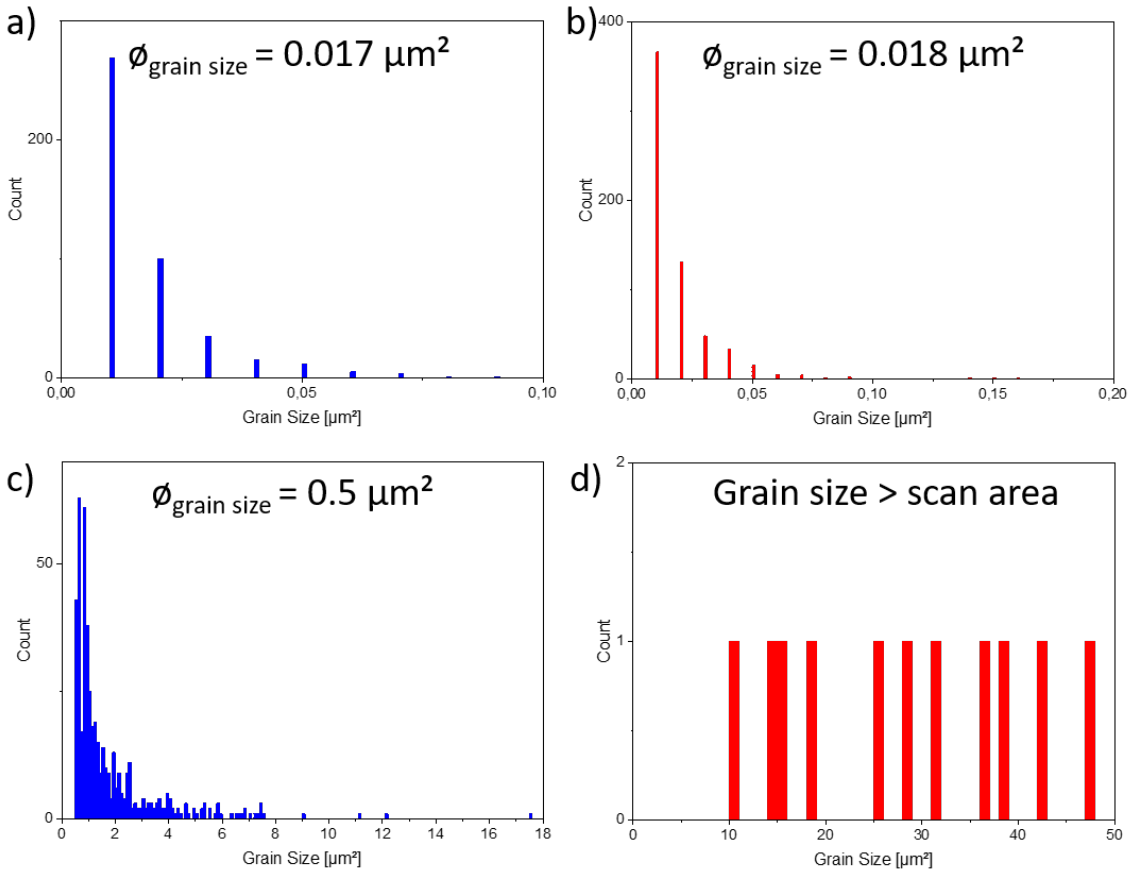

Figure 4.35: The grain size distribution from EBSD maps for a) as-deposited Au on O-ZnO b) as-deposited Au on Zn-ZnO c) Au on O-ZnO annealed at 800 °C for 2 minutes in nitrogen d) Au on Zn-ZnO annealed at 800 °C for 2 minutes in nitrogen

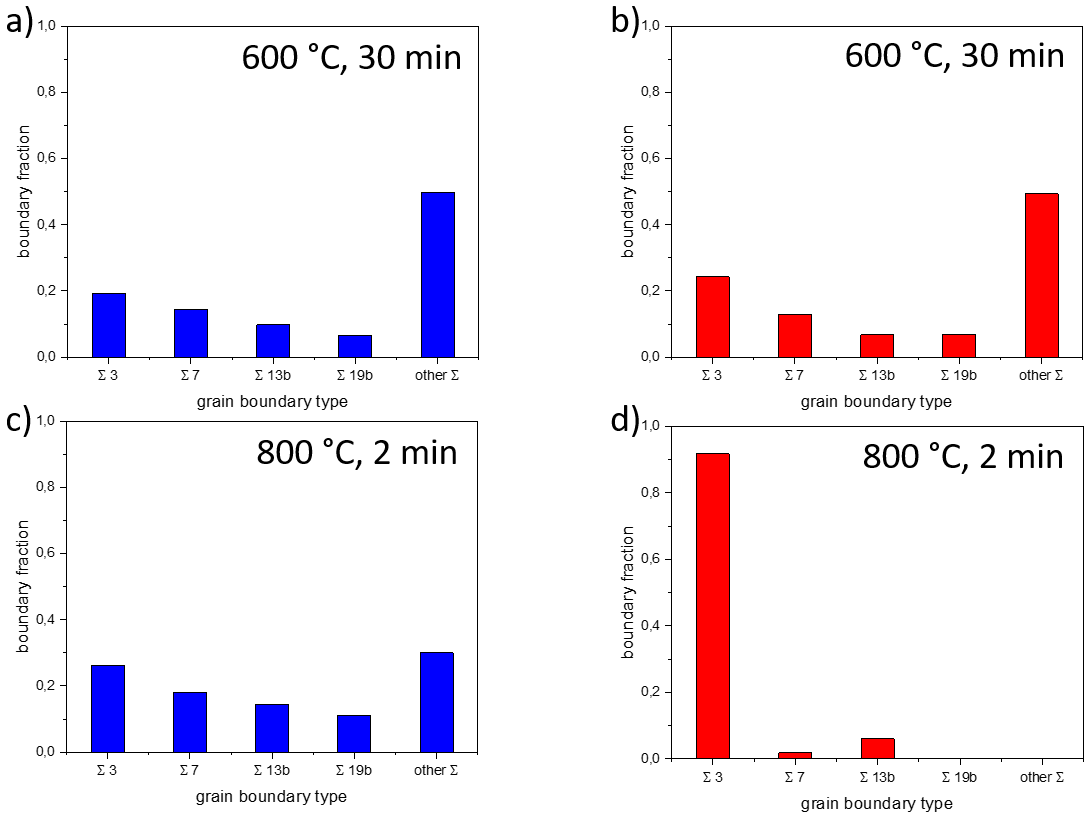

Figure 4.36: The grain boundary fraction calculated from the boundary length of Au on the two ZnO surfaces, after annealing at different times and temperatures a) O-ZnO 600 °C, 30 minutes b) Zn-ZnO 600 °C, 30 minutes c) O-ZnO 600 °C, 2 minutes d) Zn-ZnO 600 °C, 2 minutes

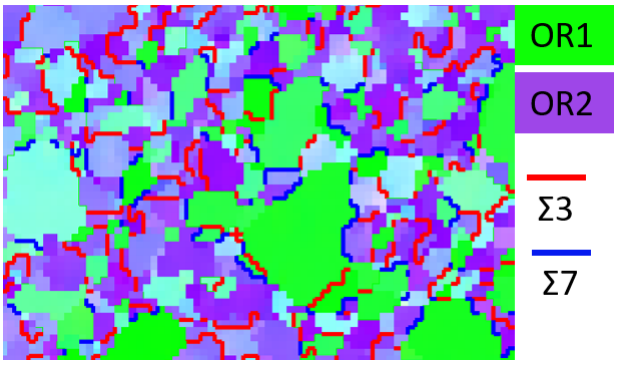

Figure 4.37: In the Au film on O-ZnO annealed at 800 °C the Σ3 grain boundaries (red) are only between twin grains of the same OR and the Σ7 grain boundaries (blue) are only between grains of different OR.

Chapter 5

Discussion

5.1 Dewetting on Sapphire

The dewetting series of Au on the c-plane of sapphire closely follows the descriptions of solid-state dewetting in the literature [2]. The films heated with constant nitrogen flow (Figure 4.1) show many holes at short times and temperatures. At longer annealing times the holes grow until the film completely transforms into wires and finally particles.
In the comparison of different atmospheres the results deviate from the literature, where Au dewetts faster in hydrogen and slower in nitrogen [55]. A reason for this could lie in the use of the RTA furnace instead of more conventional ovens. The heating in different atmospheres takes different amounts of energy in the RTA (Table 5.1), which is not directly given by the furnace but is calculated from the power usage in each 0.25 second time step individually and then added up. For finishing the recipe that heats with $100\,^{\circ}\mathrm{C\,s^{-1}}$ to $800\,^{\circ}\mathrm{C}$ and holds this temperature for 120 s, vacuum needs the least amount of energy. This is not surprising, because their is little atmosphere left to absorb the energy from the halogen lamps. The heat absorbency depends on the gases used. Hydrogen has a specific heat capacity of $28.836\,\mathrm{J\,mol^{-1}\,K^{-1}}$ (at 25 °C, 1 bar) [56] and argon is at $20.785\,\mathrm{J\,mol^{-1}\,K^{-1}}$ [56]. This brings the mixture of 5 vol% hydrogen and 95 vol% argon to a specific heat capacity of $21.188\,\mathrm{J\,mol^{-1}\,K^{-1}}$ which is lower than the $29.124\,\mathrm{J\,mol^{-1}\,K^{-1}}$ [56] of nitrogen. This explains the different energy usages in the RTA to reach the same temperature (Table 5.1), but can it also explain the dewetting behavior?

Table 5.1: Energy usage for heating a sample in different atmospheres in the RTA for 2 minutes with a temperature of 800 °C

Atmosphere	Energy (kWh)
Nitrogen	0.25
Hydrogen/Argon (5 %/95 %)	0.24
Vacuum (p <10^{-4} mbar)	0.22

All samples heated in vacuum show less advanced dewetting than samples heated in a gas at atmospheric pressure. The measured temperature is the same, so the difference must be a result of heat transfer to the sample. In principle there are three different modes of heat transfer: convection, diffusion and radiation. Convection is severely limited in a vacuum and the gold

film on top of the sample reflects more than 95 % of the electromagnetic waves in the infrared range [57]. A large part of the transferred heat must therefore come through diffusion from the SiNx wafer, that is used as an sample holder and reflects less than half of the incoming light [58]. At atmospheric pressure, convection plays a major roll because it can transport energy, both towards and away from the sample. The overall energy flow is hard to judge because the lamp, the wafer and the sample are hot and the chamber walls are actively cooled, but based on the dewetting of the samples it can be assumed that more heat reaches the sample compared to the vacuum. A difference in the hydrogen/argon and the nitrogen annealed samples can be explained by the heat capacities. The nitrogen atmosphere has more energy stored and when the molecules interact with the Au film, more energy gets transferred and therefore causes the faster dewetting. This effect likely depends on the furnace and the way of heating, if the sample is in direct contact with a heating element then a nitrogen atmosphere might remove energy the fastest and decrease the dewetting rate. That way vacuum could show the fastest dewetting. The transferred energy to the sample is difficult to measure so one possible workaround is to adjust the pressures of the used gases until the atmosphere has the same heat capacity and control it by the energy uptake of the RTA.
Another explanation for the difference in dewetting might be that the gases adsorbed to the sample surface change the surface energy γ_s and the surface diffusion, which then influences the dewetting [59].

The coexistence of small and large holes in the still mostly connected films (Figure 4.5) could happen because they appear later, grow slower or are below the critical hole radius R_c and therefore grow not at all. With equation 2.6 the last point can be excluded because the calculated R_c is only 25 nm for a gold film of this thickness, which is much smaller than the 100 nm radius observed here. Another point is that these dark spots were not observed in the AFM. In principle the holes might simply be too small for the AFM tip to fit in, whose radius was not measured. Another reason could be that these holes start growing from the substrate and a small film is still covering them. The electrons from the SEM might pass through the remaining Au film and into the substrate where they are then absorbed, therefore creating a dark spot.

5.2 Gold Orientation on Sapphire

The Au films and particles on sapphire all have the same (111) texture. This is expected for a fcc metal like gold, because this is the plane with the lowest surface energy [60]. From the EBSD PF (Figure 4.7) it is clear that the in-plane orientation is much more random and OR1 with a lattice misfit of 3.8 % and OR2 at 16.6 % are not preferred orientation relations for this material system. This fits to the findings of Sadan and Kaplan [22] who had annealing times up to 100 hours and also found no preferred in-plane orientation. In another publication of Fecht and Gleiter [8] they report a high X-ray intensity for OR1 and OR2, but don't report the signal strength for particles with other orientations rotated around the [111] axis. While incomplete, their data could also suggests a random in-plane orientation.
There still is one influence on the Au orientation by the sapphire substrate which can be seen

in the IPFs (Figure 4.8). For the vacuum samples, that showed slower dewetting, the IPF signal forms 2 distinct lines in the x- and y-directions. For the nitrogen and hydrogen/argon the x-direction, which is parallel to the sapphire $(10\bar{1}0)$ plane, further focuses into one single curve while the y-direction remains split. This means these particles, that received the most heat during annealing have a $\sim 2°$ deviation from [111], but only in the direction parallel to the sapphire $(11\bar{2}0)$ plane. A reason for this might be steps in the sapphire surface. Their edges go along the $[10\bar{1}0]$ direction [61] and might prevent the particles from tilting out of the [111] axis in this particular orientation. Heating experiments with longer annealing times might also show a focusing in the y-direction IPF, if the equilibrium structure has no out-of-plane tilt from the [111] axis. A tilt due to epitaxial strain as it appears for Au on Ge [62] can be mostly excluded, because their is nearly no in-plane epitaxy. Another factor is the surface reconstruction of Au and interface reconstruction of Au-sapphire, which might have an influence. Further experiments could help to get a deeper understanding of the mechanism behind this phenomenon.

5.3 Degradation of ZnO

The degradation of ZnO in combination with Ni can be attributed to the oxidation of nickel and the subsequent reduction of ZnO. The same destructive effect is observed with Al/ZnO [43] and Co/O-ZnO [44]. On the Zn-ZnO side it is probably made possible by missing Zn atoms on the surface, where Ni atoms can react easier with the O atoms below. In principle oxidation reactions can be stopped by applying a voltage potential, but this was not tested here. An influence of the Au on the ZnO substrate during dewetting was shown before in literature by Schaefer et al [54]. However they only looked at polycrystalline evaporated ZnO layers and had different temperature treatments, but they also found pitting of the ZnO around Au particles. ZnO is known to sublimate, but only at temperatures of more than 1300 °C. One possible explanation for this behavior could be a catalytic reaction that increases the reduction of ZnO. Then metallic Zn would stay behind and alloy with the Au particles, while the O atoms would mix with the atmosphere in the RTA chamber (Figure 5.1).

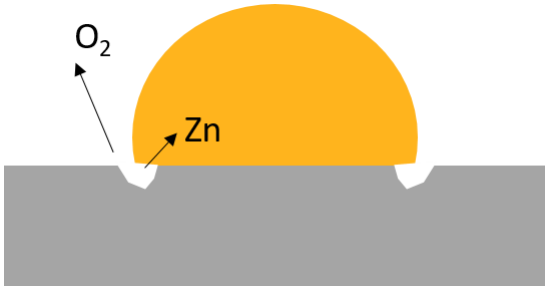

Figure 5.1: The proposed mechanism of ZnO degradation in combination with Au. Zn atoms alloy with the Au particles and oxygen evaporates into the furnace chamber

The lower reaction rate on the Zn-ZnO could be due to the binding energy of the first Zn atoms to the underlying O layer, which is stronger than the binding energy of the first oxygen atoms on O-ZnO. It is important to avoid this degradation, but it does not greatly influence the results of the samples in this thesis, based on the visible effect. Even the strongest degradation observed in

the 950 °C sample was only a few nanometers deep. The Arrhenius equation predicts a doubling of the reactions speed for every 10 °C increase of temperature [63], which means the sample heated at 900 °C should have less than a nanometer of degradation depth.

5.4 Influence of polarity on the dewetting behavior of Au on ZnO

In dewetting studies a typical comparison is the final particle size or density, but this is not done here because only the Au films on O-ZnO substrates reached a state with a full transformation into particles. When comparing the covered area on the ZnO substrates it is obvious that a Au thin-film on O-ZnO (Figure 4.21) dewetts significantly faster than on the Zn-ZnO side (Figure 4.23) especially at the 900 °C and 950 °C samples. This suggests that the interface energy of Au/O-ZnO is higher than that of Au/Zn-ZnO, which would explain the different behaviors. Sadly the literature data on the Au/ZnO interface is very sparse and our own attempt at determining the interface energy failed due to degradation of ZnO during long heating times. Instead of the interface energy the surface energy of ZnO can in principle be used to explain the results, because a higher surface energy should increase wetting and slow down dewetting. The surface energy of O-ZnO is indeed lower than that of Zn-ZnO at $0.96\,\mathrm{J\,m^{-2}}$ and $2.39\,\mathrm{J\,m^{-2}}$ respectively [64] which fits the experiments, but this is not really a viable strategy, because it neglects the interaction with the Au film. Another workaround is using the binding energy, where values from simulations are available [65]. The Zn-Au bond is stronger than O-Au, which makes sense as gold is not typically known to strongly react with oxygen. The binding energy is directly proportional to the adhesion energy γ_{adh}, which influences the interface energy γ_i through the equation:

$$\gamma_i = \gamma_{s,Au} + \gamma_{s,ZnO} - \gamma_{adh} \tag{5.1}$$

where $\gamma_{s,Au}$ and $\gamma_{s,ZnO}$ are the respective surface energies. The higher binding energy of Zn-Au results in a high adhesion energy which in turn lowers the interface energy and fits to the observed higher resistance to dewetting.
Another useful parameter is the activation energy E_a of dewetting (Figure 5.2), because it helps to draw conclusions on the dewetting mechanism. Some values for surface and volume diffusion were already collected by Müller et al. [66] although it should be kept in mind that the exact values are influenced by the substrate and the heating method. Volume diffusion has a higher activation energy at 1.71-18.3 eV than surface diffusion at 0.4-1.4 eV [66]. For Zn-ZnO E_a is 0.87 eV, which fits well to surface diffusion and is regarded as one of the main mechanism of solid-state dewetting [2]. The values for O-ZnO and sapphire could not be determined from the existing samples because their dewetting has progressed too far and the Arrhenius plot approach fails when the remaining Au is mostly in the form of particles.

For the influence of the annealing atmosphere the same reduced dewetting is observed on O-ZnO as on sapphire. The reason is probably the smaller amount of transferred energy in vacuum from the halogen lamps of the RTA furnance to the sample. Zn-ZnO on the other hand behaves

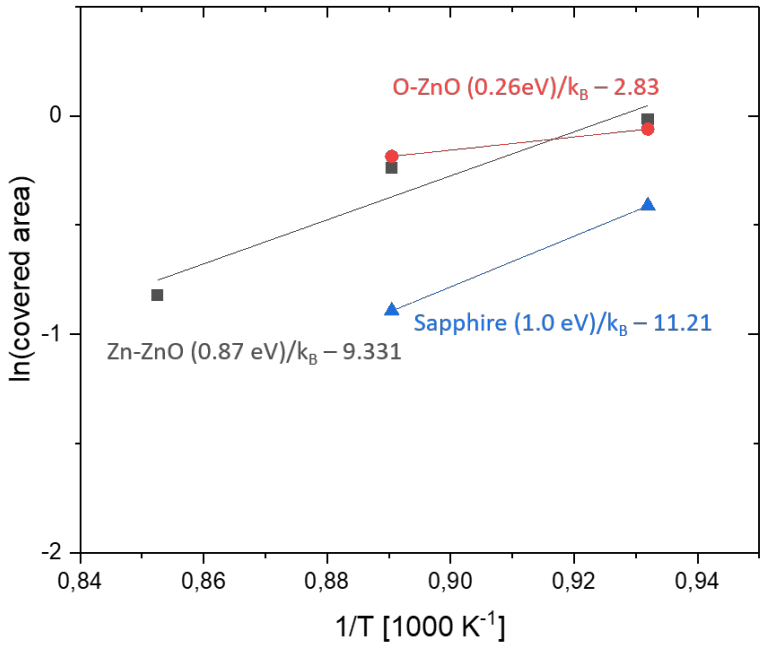

Figure 5.2: Arrhenius plot of the dewetting rate for 40 nm Au films heated in nitrogen, based on the covered area. For O-ZnO and sapphire only two suitable images were taken, which is not enough for accurately determining the activation energy

different with both dewetting rates being roughly equivalent (Figure 4.27) which might be caused by the anisotropic dewetting at high temperatures in nitrogen and in the whole vacuum series with the formation of triangular holes (Figure 4.19). Molecules can attach to the Au surface and change the surface energy and the surface diffusion, which is the driving factor for dewetting. An influence especially from hydrogen and oxygen was observed before in Au [67] and in Ni [59]. The anisotropic dewetting effect is not observed in Au on O-ZnO, which probably has little to do with the annealing ambient and more with the smaller grain size and their different orientation relations.

5.5 Influence of polarity on the texture evolution of Au on ZnO

All Au films and particles have a (111) out-of-plane texture on both ZnO sides in the same way as on sapphire. For this system the same explanation of the low energy (111) planes [60] causing an epitaxial growth of these planes applies here. Also a splitting in the y-direction IPF by $\pm 2°$ signal is observed for Au twins on O-ZnO and Zn-ZnO (Figure 4.31). The ZnO surface can also consist of steps with a monoatomic height [38] and this might have an effect here, but a conclusive answer is not possible at this point.
The epitaxial growth and the in-plane orientation of Au on ZnO (Figure 2.2) was studied before by Wassermann and Polacek [68, 69] and they observed only OR2 with (Au(110) $\parallel$ ZnO(11$\bar{2}$0)) on both Zn-ZnO and O-ZnO. In their experiments they cleaved a ZnO crystal in UHV to avoid

surface contamination and varied the temperature during deposition from −253 °C to 467 °C. The temperatures explain why they did not see a predominant OR1, which is in this thesis only observed at the sample annealed at 800 °C and above, but it confirms the as-deposited state close to room temperature with a preferred OR2. They also did not give an theoretical explanation for the occurrence of the Au orientation relative to ZnO so an attempt at this is made here. According to Equation 2.1 the calculated lattice misfit is +2.6 % for OR1 (Au(110) ∥ ZnO($10\bar{1}0$)) and -12.4 % for OR2 (Au(110) ∥ ZnO($11\bar{2}0$)). Based alone on the lower lattice misfit the preferred orientation should always be OR1, but the results from the EBSD mappings show the samples without heat treatment are in OR2 and they only switch when annealing at higher temperatures.

The low temperature, high misfit orientation can be explained with the CSL of Au and ZnO and Equation 2.4, where a super cell (Figure 5.3) with 10 Au atoms and 9 zinc or oxygen atoms and a side length of 28.8 Å has a remaining lattice misfit of only -1.1 %. The existence of a low misfit super cell is also used in literature to explain this orientation relation in the Pd/ZnO [9] and the Ag/ZnO [10] systems, which have a similar high lattice misfit. With this geometric approach two super cell (Figure 5.4) can be found for OR1, one with 9 Au and 14 Zn atoms at a length of 45.0 Å and the other with 29 Au and 15 Zn atoms at a length of 89.4 Å. The misfit of these super cells from Equation 2.4 is -0.0091 % for the smaller cell and -0.0066 % for the larger one. Based on the misfit of the super cell one would assume that OR1 is always preferred, however the CSL approach is usually only used for a lattice misfit above 10 % [11]. At high temperatures this explanation fails, because the results show a switch of the dominating orientation relation to OR1.
A similar change of the OR is observed for Au on a Si substrate. An explanation for this kind of OR switching is the change in lattice constants and lattice misfit during heating. The new OR is then the one with the lowest misfit at the specific temperature [70]. In the Au/ZnO system the different lattice expansion factors of Au (α_{Au}=1.40 × $10^{-6}\,K^{-1}$ [50]) and ZnO (α_{ZnO}=4.31 × $10^{-6}\,K^{-1}$ for the a-axis and α_{ZnO}=2.49 × $10^{-6}\,K^{-1}$ for the c-axis [71]) change the misfit when heating up. The new lattice distances d are calculated with:

$$d = d_0(1 + \alpha\Delta T) \tag{5.2}$$

where l_0 is the original lattice constant at room temperature, α is the thermal expansion factor and ΔT is the temperature change in Kelvin. The calculated lattice parameters and the spacing of relevant planes can be found in Table 5.2.
At 800 °C the lattice misfit in OR1 increases to +3.4 % and OR2 decreases to -11.6 %. With the CSL approach the new OR2 cell has the same atomic spacing at 10 Au atoms and 9 zinc or oxygen atoms and an even lower remaining misfit at -0.41 %. This should mean that the OR2 is even more favorable, but the experimental data obviously show OR1 as preferred despite its growing misfit. This means a simple geometrical approach to the orientation relation is not enough and the interaction of the atoms at the interface needs to be taken into account. The OR2 configuration might have on average more atoms in favorable positions than OR1. At high temperatures the interface reconstruction, could then change the atom position and lower the

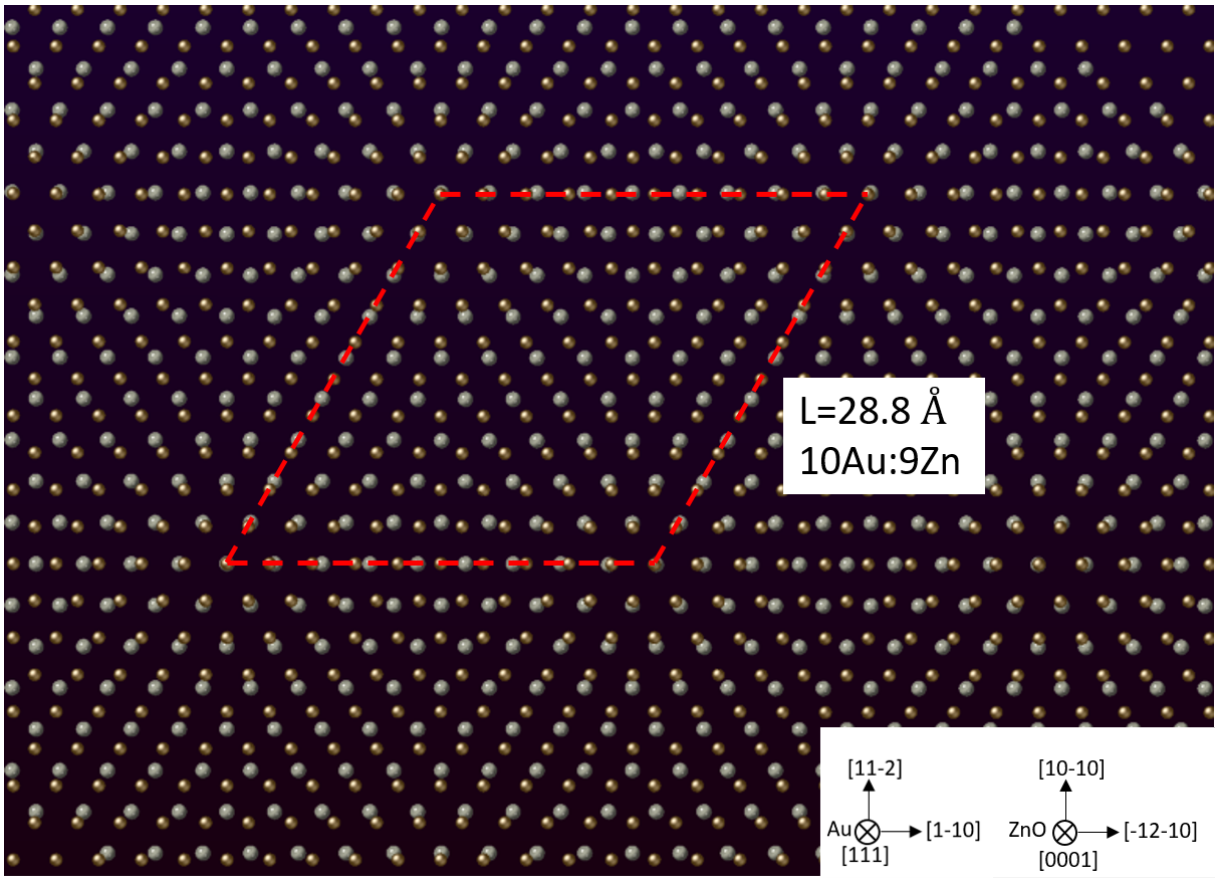

Figure 5.3: A layer of (111) Au on top of a layer (0001) Zn in OR2, with the super cell of 10Au:9Zn atoms marked in red. The O atoms are hidden for better comprehensibility. On the O-ZnO side the same super cell can be found.

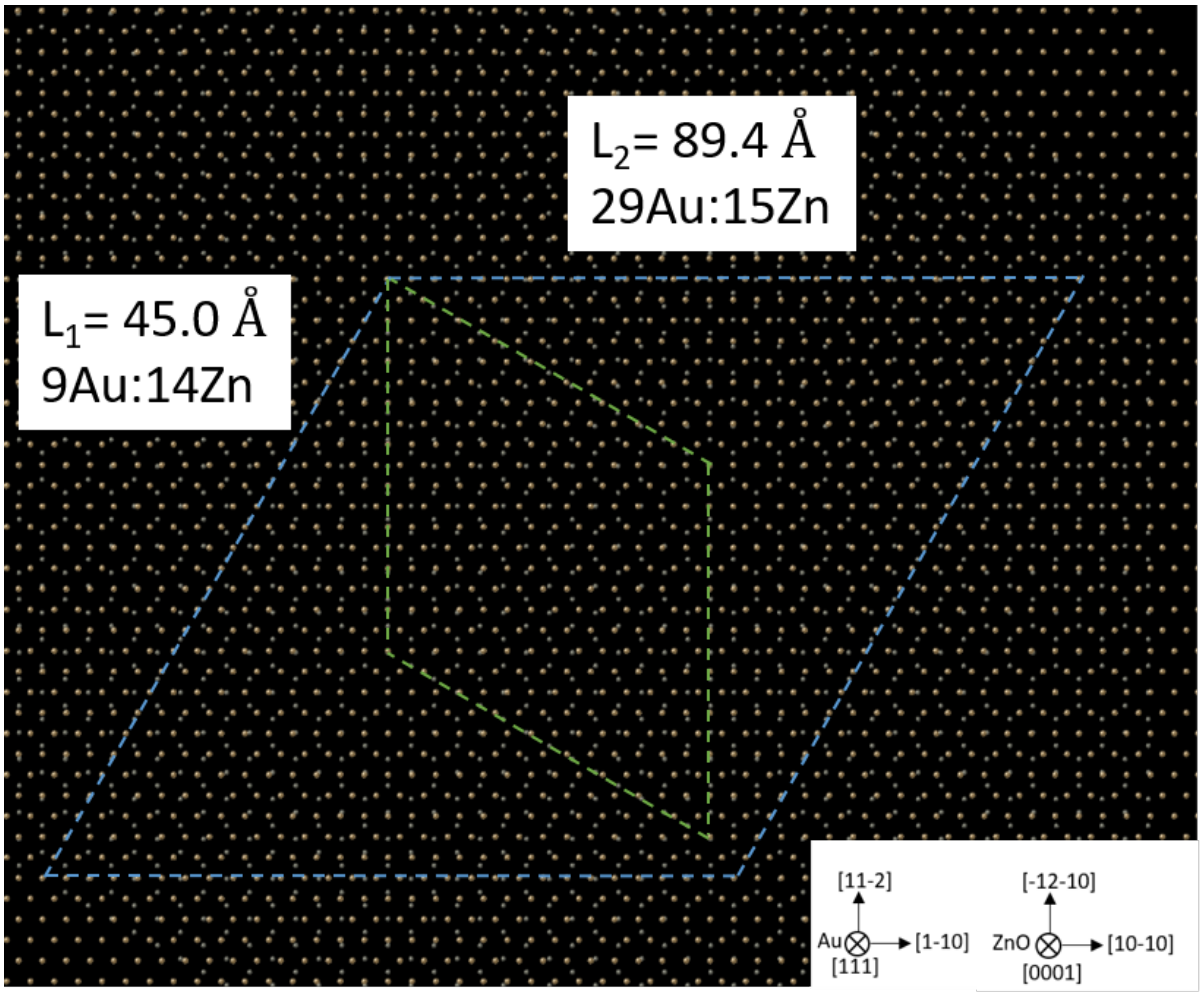

Figure 5.4: A layer of (111) Au on top of (0001) Zn with two CSL super cells L_1 (green) is small with 9Au:14Zn and L_2 (blue) is large with 29Au:15Zn. The O atoms are hidden for better comprehensibility. On the O-ZnO side the same super cell can be found.

Table 5.2: Lattice parameters and relevant spacing of Au and ZnO at room temperature and at 800 °C

Lattice plane	Room temperature	800 °C
a_{Au}	4.09 Å	4.13 Å
a_{ZnO}	3.25 Å	3.26 Å
c_{ZnO}	5.21 Å	5.22 Å
$d(110)_{Au}$	2.892 Å	2.922 Å
$d(112)_{Au}$	1.670 Å	1.688 Å
$d(10\bar{1}0)_{ZnO}$	2.814 Å	2.822 Å
$d(11\bar{2}0)_{ZnO}$	1.625 Å	1.630 Å

energy of OR1 enough to make it preferred. A simulation of both orientations on the two polar ZnO sides could compare the binding energies and therefore clarify if this is the reason for the switching or not.

5.6 Interface of gold and ZnO

On the OR2 Au/ZnO interface misfit dislocations can be found (Figure 4.32). To analyze these, a burgers circuit was carried out and shows a closing error of a/4⟨112⟩ (Figure 5.5) This would correspond to the projection of an inclined a/2⟨110⟩ Burgers vector into the image plane [72]. The [110] dislocations have a Burgers vector

$$b = (a/2)\sqrt{h^2 + k^2 + l^2} = 0.289\,nm \tag{5.3}$$

and with the misfit of -12.4 % equation 2.2 can be used to calculate the dislocation spacing of 2.33 nm, which fits perfectly to the measured value (Figure 4.32). The regular spacing of the dislocations should result in a dislocation network.

Interface reconstruction on ZnO is known to exist in Pd on Zn terminated ZnO [9], but was not yet described for Au on ZnO. For a complete description of the atom position at the interface of OR1 a second cross-section in the $[11\bar{2}0]$ orientation is necessary, but at the time of writing this is not yet completed. Some interesting results from the existing cross-section is that the spacing of high intensity areas (Figure 4.33) is very similar to the smaller CSL super cell (Figure 5.4), but with twice as many Au and ZnO atom columns visible due to the projection in this orientation. The lower intensity regions in the first layer likely comes from a slight shift of the Au atoms perpendicular to the viewing direction to find a energetically preferred position. In addition the Zn atoms could also show reconstruction in the terminating layer. The oxygen terminated substrates do not show the same reconstruction [73] which could explain why the OR1 is not observed on O-ZnO.
From simulations the distance between the first Au atoms and the ZnO are known to depend on the relative position. Despite not being the lowest energy configuration the position of Au directly on top of Zn has the best fitting distance (2.59 Å) [65] to the spacing in the HRSTEM image (2.6 Å). If the same is true for the O-ZnO surface could not be determined from the

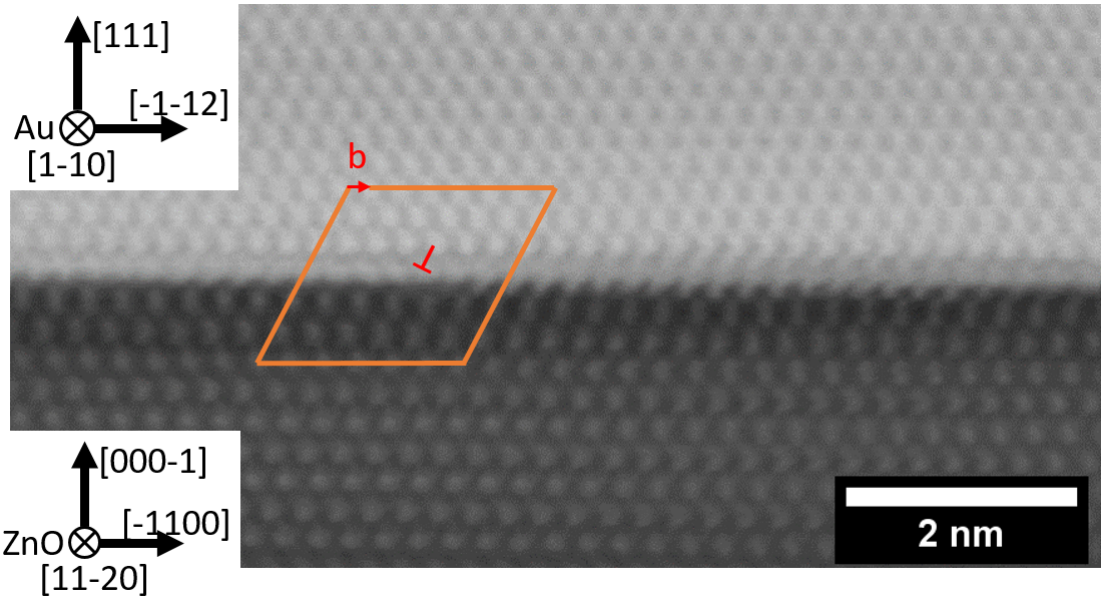

Figure 5.5: The Burgers circuit analysis reveals a projected $a/4\,\langle 112\rangle$ vectror, which coresponds to a perfect $a/2\,\langle 110\rangle$ Burgers vector.

poorly resolved interface.

5.7 Grain growth on ZnO

In the as-deposited films the theory of normal grain growth is already no longer applicable, because many of the Au grains are larger than the film thickness with diameters above 100 nm. This might be in part due to epitaxial grain growth during deposition of Au grains which are close to a preferred orientation relation [74]. During annealing at higher temperatures, the general trend of faster growing OR1 seems the same for both of the studied ZnO crystal planes, but the grain growth rate is different. This is likely in part caused by the earlier onset of dewetting on O-ZnO. Due to grain boundary grooving, grains are no longer touching and they don't have grain boundaries whose energy could be minimized. For the samples up to a temperature of 800 °C and short annealing times this should not be a great influence and grain growth is known to happen simultaneously to the early stages of dewetting [75]. Therefore it makes sense to also study Au grains on O-ZnO substrates.

For a correct calculation of the grain growth speed with Equation 2.5 precise material properties need to be used, but those are not available. This leaves a qualitative look at the process as the only option. The orientation of the grains with highest growth rate depends on the surface and the interface energy. In the Au films with a (111) texture the surface energy has no influence, because it is already in a low energy state. From the heating experiments at 400 °C and 600 °C it can be seen that the grain size for OR1 and OR2 is very similar (Figure 4.34). This stems either from a very similar interface energy for OR1 and OR2 or the energy barrier to switch from OR2 to OR1 is too high to overcome at this point. At 800 °C OR1 probably has the lower interface energy and the grains with this orientation could have an energy advantage and start growing faster. However the main driving force for grain growth on both ZnO surface is likely the minimization of the grain boundary energy [76]. The lowest possible energy that the poly crystalline Au film can reach is with 60° boundaries, which is about 5 times lower than the energy for the 30° boundaries between OR1 and OR2 [77]. A change to more $\Sigma 3$ grain boundaries is especially pronounced in the Au film on Zn-ZnO (Figure 4.36), therefore it can be concluded that the energy reduction is much more efficient on this ZnO side. This leaves the question if in addition to dewetting other factors slow down grain growth on the O-ZnO substrates. As mentioned before the main problem with giving conclusive answers is the lack of precise interface data. The difference of interface energies for OR2 and OR1 might be simply lower on O-ZnO and the incentive to grow one preferred grain orientation gets smaller or the energy barrier to switch between orientations is too high, this way the grains of both orientations could block each other from growing. Determining the interface energy, either experimentally or through simulations, is a good approach to answer some of the remaining questions.

Chapter 6

Summary and Outlook

The solid-state dewetting behavior, grain growth and texture evolution of gold on sapphire and the polar ZnO surfaces was studied with rapid thermal annealing and electron microscopy. In the nitrogen atmosphere the gold films on sapphire dewetted the fastest followed by O-ZnO and the slowest is Zn-ZnO. This can be attributed to the different binding strength of Au to the substrates. Annealing experiments in different atmospheres did not result in easily comparable data, because of the varying heat transfer in the RTA furnace, which dominates over any influences on dewetting. Only the Au films on Zn-ZnO showed an obvious difference from vacuum annealing in the form of anisotropic dewetted holes, which do not appear in nitrogen.
All examined Au films have a (111) texture independent of the substrate. However an epitaxial in-plane relation for Au on sapphire could not be determined in annealed samples. As-deposited Au films on ZnO already show a preferred Au(110) $\parallel$ ZnO($11\bar{2}0$) in-plane orientation relation. That changes during heat treatment for Zn-ZnO substrates. A clear epitaxial $Au[110](111) \| ZnO[10\bar{1}0](0001)$ orientation relation appear for sample heated at 800 °C and above. On O-ZnO the OR1 is present, but does not dominate over Au grains with OR2 even above 800 °C. The exact reason for the epitaxy of this orientation could not be determined in this thesis, but the results from HRSTEM imaging suggest that interface reconstruction likely plays a role.
The main issue in studying the dewetting of ZnO samples is the degradation at high temperatures and reactive elements, which lowers the number of possible parameters for these experiments. Avoiding this degradation would be necessary to experimentally find the interface energy for metals on ZnO through the equilibrium Winterbottom shape. For further research on the Au/ZnO interface the iDPC mode for high resolution STEM imaging is a promising technique. In principle iDPC can produce high resolution images with much better contrast for light elements like oxygen and show the bonds between atoms [78]. This needs high quality FIB cross-sections which will be produced in the future and could help develop the understanding of interfaces. Furthermore long-time annealing experiments can be conducted to study the texture evolution up to the point where a definitive equilibrium is reached.

Acknowledgment

I want to thank **Erdmann Spiecker** for giving me the opportunity to work as an Hiwi and to contribute to current research with my Master Thesis.

Furthermore I want to thank:
Martin Dierner for countless hours at the microscopes and supervising this thesis.

Johannes Will for valuable ideas and discussions.

Sabine Hübner for preparing TEM lamellas.

Johanna Schubert and **Mingjian Wu** for helping at the microscopes.

Bibliography

[1] M. Chmielewski and K. Pietrzak, "Metal-ceramic functionally graded materials–manufacturing, characterization, application," *Bulletin of the Polish Academy of Sciences. Technical Sciences*, vol. 64, no. 1, pp. 151–160, 2016 (cit. on p. 1).

[2] C. V. Thompson, "Solid-state dewetting of thin films," *Annual Review of Materials Research*, vol. 42, 2012, ISSN: 15317331. DOI: 10.1146/annurev-matsci-070511-155048 (cit. on pp. 1, 6, 48, 51).

[3] G. Stringfellow, "Epitaxy," *Reports on Progress in Physics*, vol. 45, no. 5, p. 469, 1982 (cit. on p. 1).

[4] F. Ernst, "Metal-oxide interfaces," *Materials Science and Engineering: R: Reports*, vol. 14, pp. 97–156, 3 Apr. 1995, ISSN: 0927796X. DOI: 10.1016/0927-796X(95)80001-8 (cit. on pp. 2, 3).

[5] H. Meltzman, D. Mordehai, and W. D. Kaplan, "Solid-solid interface reconstruction at equilibrated ni-al 2o 3 interfaces," *Acta Materialia*, vol. 60, pp. 4359–4369, 11 Jun. 2012, ISSN: 13596454. DOI: 10.1016/j.actamat.2012.04.037 (cit. on pp. 2, 3).

[6] Y. Ikuhara and P. Pirouz, "High resolution transmission electron microscopy studies of metal/ceramics interfaces," *Microscopy Research and Technique*, vol. 40, pp. 206–241, 3 Feb. 1998, ISSN: 1059-910X. DOI: 10.1002/(SICI)1097-0029(19980201)40:3<206::AID-JEMT4>3.0.CO;2-S (cit. on p. 2).

[7] K. Oura, M. Katayama, A. V. Zotov, V. G. Lifshits, and A. A. Saranin, *Surface Science*. Springer Berlin Heidelberg, 2003, ISBN: 978-3-642-05606-2. DOI: 10.1007/978-3-662-05179-5 (cit. on p. 3).

[8] H. J. Fechtt and H. Gleiter, "A lock-in model for the atomic structure of interphase boundaries between metals and ionic crystals," 1985, pp. 551–562. DOI: 10.1016/0001-6160(85)90019-7 (cit. on pp. 3, 49).

[9] H. Li, M. Saito, C. Chen, K. Inoue, K. Akagi, and Y. Ikuhara, "Strong metal–metal interaction and bonding nature in metal/oxide interfaces with large mismatches," *Acta Materialia*, vol. 179, pp. 237–246, Oct. 2019, ISSN: 13596454. DOI: 10.1016/j.actamat.2019.08.018 (cit. on pp. 3, 17, 53, 56).

[10] N. Jedrecy, G. Renaud, R. Lazzari, and J. Jupille, "Unstrained islands with interface coincidence sites versus strained islands: X-ray measurements on ag/zno," *Physical Review B - Condensed Matter and Materials Physics*, vol. 72, 19 Nov. 2005, ISSN: 10980121. DOI: 10.1103/PhysRevB.72.195404 (cit. on pp. 3, 53).

[11] A. Trampert and K. H. Ploog, "Heteroepitaxy of large-misfit systems: Role of coincidence lattice," *Crystal Research and Technology*, vol. 35, pp. 793–806, 6 2000, ISSN: 02321300. DOI: 10.1002/1521-4079(200007)35:6/7<793::AID-CRAT793>3.0.CO;2-3 (cit. on pp. 3, 4, 53).

[12] P. W. Tasker, "The stability of ionic crystal surfaces," *Journal of Physics C: Solid State Physics*, vol. 12, no. 22, pp. 4977–4984, Sep. 1979. DOI: 10.1088/0022-3719/12/22/036 (cit. on pp. 4, 17).

[13] V. Consonni and A. M. Lord, "Polarity in zno nanowires: A critical issue for piezotronic and piezoelectric devices," *Nano Energy*, vol. 83, p. 105 789, May 2021, ISSN: 22112855. DOI: 10.1016/j.nanoen.2021.105789 (cit. on p. 5).

[14] G. Heiland and P. Kunstmann, "Polar surfaces of zinc oxide crystals," *SURFACE SCIENCE*, vol. 13, 1969 (cit. on p. 4).

[15] H. Tampo *et al.*, "Determination of crystallographic polarity of zno layers," *Applied Physics Letters*, vol. 87, pp. 1–3, 14 Oct. 2005, ISSN: 00036951. DOI: 10.1063/1.2067689 (cit. on p. 4).

[16] Y. Li, Q. F. Xing, Y. Yan, and W. L. Zhou, "A large quantity synthesis of zno nanoneedles and their polarity determination," *Journal of Nanoscience and Nanotechnology*, vol. 10, pp. 2023–2027, 3 Mar. 2010, ISSN: 15334880. DOI: 10.1166/jnn.2010.2129 (cit. on p. 4).

[17] C. V. Thompson, "Grain growth in thin films," *Annual Review of Materials Science*, vol. 20, pp. 245–268, 1 Aug. 1990, ISSN: 0084-6600. DOI: 10.1146/annurev.ms.20.080190.001333 (cit. on pp. 6, 45).

[18] F. Niekiel, "Solid-state dewetting of metallic thin films studied by advanced in situ electron microscopy techniques," Friedrich-Alexander-Universität Erlangen-Nürnberg, 2017 (cit. on p. 6).

[19] D. J. Srolovitz and M. G. Goldiner, "The thermodynamics and kinetics of film agglomeration," *JOM*, vol. 47, pp. 31–36, 3 Mar. 1995, ISSN: 1047-4838. DOI: 10.1007/BF03221433 (cit. on p. 6).

[20] G. Wulff, "Xxv. zur frage der geschwindigkeit des wachsthums und der auflösung der krystallflächen," *Zeitschrift für Kristallographie - Crystalline Materials*, vol. 34, pp. 449–530, 1-6 Dec. 1901, ISSN: 2196-7105. DOI: 10.1524/zkri.1901.34.1.449 (cit. on p. 7).

[21] W. Winterbottom, "Equilibrium shape of a small particle in contact with a foreign substrate," *Acta Metallurgica*, vol. 15, pp. 303–310, 2 Feb. 1967, ISSN: 00016160. DOI: 10.1016/0001-6160(67)90206-4 (cit. on p. 7).

[22] H. Sadan and W. D. Kaplan, "Au-sapphire (0001) solid-solid interfacial energy," *Journal of Materials Science*, vol. 41, pp. 5099–5107, 16 Aug. 2006, ISSN: 00222461. DOI: 10.1007/s10853-006-0437-5 (cit. on pp. 7, 49).

[23] K. S. Harsha, *Principles of Vapor Deposition of Thin Films*, First. Elsevier, 2006, ISBN: 978-0-08-044699-8 (cit. on pp. 8, 9).

[24] G. Sauerbrey, "Verwendung von schwingquarzen zur wägung dünner schichten und zur mikrowägung," *Zeitschrift für Physik*, vol. 155, pp. 206–222, 2 Apr. 1959, ISSN: 1434-6001. DOI: 10.1007/BF01337937 (cit. on p. 8).

[25] J. I. Goldstein, D. E. Newbury, J. R. Michael, N. W. Ritchie, J. H. J. Scott, and D. C. Joy, *Scanning Electron Microscopy and X-Ray Microanalysis*. Springer New York, 2018, ISBN: 978-1-4939-6674-5. DOI: 10.1007/978-1-4939-6676-9 (cit. on pp. 9, 10, 13).

[26] D. B. Williams and C. B. Carter, *Transmission Electron Microscopy*. Springer US, 2009, ISBN: 978-0-387-76500-6. DOI: 10.1007/978-0-387-76501-3 (cit. on pp. 9, 12, 14–16).

[27] N. Yao, *Focused Ion Beam Systems*, N. Yao, Ed. Cambridge University Press, 2007, ISBN: 9780511600302. DOI: 10.1017/CBO9780511600302 (cit. on p. 10).

[28] S. Reyntjens and R. Puers, "A review of focused ion beam applications in microsystem technology," *Journal of Micromechanics and Microengineering*, vol. 11, no. 4, pp. 287–300, Jul. 2001. DOI: 10.1088/0960-1317/11/4/301 (cit. on p. 11).

[29] C. Kisielowski *et al.*, "Detection of single atoms and buried defects in three dimensions by aberration-corrected electron microscope with 0.5-å information limit," *Microscopy and Microanalysis*, vol. 14, pp. 469–477, 5 Oct. 2008, ISSN: 1431-9276. DOI: 10.1017/S1431927608080902 (cit. on p. 11).

[30] A. J. Wilkinson and T. B. Britton, "Strains, planes, and ebsd in materials science," *Materials Today*, vol. 15, pp. 366–376, 9 Sep. 2012, ISSN: 13697021. DOI: 10.1016/S1369-7021(12)70163-3 (cit. on p. 13).

[31] M. D. Graef, *Introduction to Conventional Transmission Electron Microscopy*. Cambridge University Press, Mar. 2003, ISBN: 9780521620062. DOI: 10.1017/CBO9780511615092 (cit. on p. 14).

[32] C. Suryanarayana and M. G. Norton, *X-Ray Diffraction*. Springer US, 1998, ISBN: 978-1-4899-0150-7. DOI: 10.1007/978-1-4899-0148-4 (cit. on p. 15).

[33] M. D. Graef and M. E. McHenry, *Structure of Materials An Introduction to Crystallography, Diffraction and Symmetry*, 2nd ed. Cambridge University Press, 2012, ISBN: 978-1-107-00587-7 (cit. on p. 16).

[34] M. Saito, T. Wagner, G. Richter, and M. Rühle, "High-resolution tem investigation of structure and composition of polar pd/zno interfaces," *Physical Review B - Condensed Matter and Materials Physics*, vol. 80, 13 Oct. 2009, ISSN: 10980121. DOI: 10.1103/PhysRevB.80.134110 (cit. on p. 17).

[35] N. Sakaguchi, Y. Suzuki, K. Watanabe, S. Iwama, S. Watanabe, and H. Ichinose, "A hrtem and eels study of pd/zno polar interfaces," *Philosophical Magazine*, vol. 88, pp. 1493–1509, 10 Apr. 2008, ISSN: 14786435. DOI: 10.1080/14786430802203406 (cit. on p. 17).

[36] K. Murakami, "Arhvtem of the pd/zno heterointerface chemical structure," *Journal of Electron Microscopy*, vol. 52, pp. 27–32, 1 Mar. 2003, ISSN: 00220744. DOI: 10.1093/jmicro/52.1.27 (cit. on p. 17).

[37] A. R. Lubinsky, C. B. Duke, S. C. Chang, B. W. Lee, and P. Mark, "Atomic geometry of the low-index surfaces of zno: Leed analysis," *Journal of Vacuum Science and Technology*, vol. 13, pp. 189–192, 1 Jan. 1976, ISSN: 0022-5355. DOI: 10.1116/1.568823 (cit. on p. 17).

[38] O. Dulub, L. A. Boatner, and U. Diebold, "Stm study of the geometric and electronic structure of zno()-zn, ()-o, (), and () surfaces," *Surface Science*, vol. 519, pp. 201–217, 3 Nov. 2002, ISSN: 00396028. DOI: 10.1016/S0039-6028(02)02211-2 (cit. on pp. 17, 52).

[39] F. Rahman, "Zinc oxide light-emitting diodes: A review," *Optical Engineering*, vol. 58, p. 1, 01 Jan. 2019, ISSN: 0091-3286. DOI: 10.1117/1.oe.58.1.010901 (cit. on p. 17).

[40] H. T. Wang *et al.*, "Hydrogen-selective sensing at room temperature with zno nanorods," *Applied Physics Letters*, vol. 86, p. 243 503, 24 Jun. 2005, ISSN: 0003-6951. DOI: 10.1063/1.1949707 (cit. on p. 17).

[41] A. C. Mofor *et al.*, "Magnetic property investigations on mn-doped zno layers on sapphire," *Applied Physics Letters*, vol. 87, 6 2005, ISSN: 00036951. DOI: 10.1063/1.2007864 (cit. on p. 17).

[42] V. A. Coleman and C. Jagadish, *Basic Properties and Applications of ZnO*. Elsevier Ltd, 2006, pp. 1–20, ISBN: 9780080447223. DOI: 10.1016/B978-008044722-3/50001-4 (cit. on p. 17).

[43] Y. Gao *et al.*, "Al interaction with zno surfaces," *Journal of Physical Chemistry C*, vol. 122, pp. 17 856–17 864, 31 Aug. 2018, ISSN: 19327455. DOI: 10.1021/acs.jpcc.8b04952 (cit. on pp. 17, 50).

[44] D. Chiba, N. Shibata, and A. Tsukazaki, "Co thin films deposited directly on zno polar surfaces," *Scientific Reports*, vol. 6, Nov. 2016, ISSN: 20452322. DOI: 10.1038/srep38005 (cit. on pp. 17, 50).

[45] E. R. Dobrovinskaya, L. A. Lytvynov, and V. Pishchik, "Application of sapphire," in *Sapphire*. Springer US, 2009, pp. 1–54. DOI: 10.1007/978-0-387-85695-7_1 (cit. on p. 18).

[46] C. GmbH. "Sapphire." (), [Online]. Available: http://www.crystec.de/daten/al2o3.pdf (cit. on p. 18).

[47] W. P. Davey, "Precision measurements of the lattice constants of twelve common metals," *Physical Review*, vol. 25, pp. 753–761, 6 Jun. 1925, ISSN: 0031-899X. DOI: 10.1103/PhysRev.25.753 (cit. on pp. 18, 19, 27).

[48] R. S. Wagner and W. C. Ellis, "Vapor-liquid mechanism of single crystal growth," *Applied Physics Letters*, vol. 4, pp. 89–90, 5 Mar. 1964, ISSN: 0003-6951. DOI: 10.1063/1.1753975 (cit. on p. 18).

[49] J. Dean, *Lange's Handbook of Chemistry*, 15th ed. McGraw-Hill, 1999 (cit. on p. 19).

[50] B. N. Dutta and B. Dayal, "Lattice constants and thermal expansion of gold up to 878 °c by x-ray method," *physica status solidi (b)*, vol. 3, pp. 473–477, 3 1963, ISSN: 03701972. DOI: 10.1002/pssb.19630030312 (cit. on pp. 19, 53).

[51] *Rapid thermal processor as-one 100 installation manual*, 2.16, ANNEAL SYS, Oct. 2017 (cit. on p. 20).

[52] G. Esteves and C. M. Fancher, "Lipras: Line-profile analysis software metrictens: Crystallography view project novel analytical techniques for electron backscatter diffraction patterns view project," 2017. DOI: 10.13140/RG.2.2.29970.25282/3 (cit. on p. 20).

[53] R. Kilaas, "Optimal and near-optimal filters in high-resolution electron microscopy," *Journal of Microscopy*, vol. 190, pp. 45–51, 1-2 Apr. 1998, ISSN: 0022-2720. DOI: 10.1046/j.1365-2818.1998.3070861.x (cit. on p. 27).

[54] B. T. Schaefer, J. Cheung, J. F. Ihlefeld, J. L. Jones, and V. Nagarajan, "Stability and dewetting kinetics of thin gold films on ti, tiox and zno adhesion layers," *Acta Materialia*, vol. 61, pp. 7841–7848, 20 Dec. 2013, ISSN: 13596454. DOI: 10.1016/j.actamat.2013.09.022 (cit. on pp. 30, 50).

[55] J.-Y. Kwon, T.-S. Yoon, K.-B. Kim, and S.-H. Min, "Comparison of the agglomeration behavior of au and cu films sputter deposited on silicon dioxide," *Journal of Applied Physics*, vol. 93, pp. 3270–3278, 6 Mar. 2003, ISSN: 0021-8979. DOI: 10.1063/1.1556178 (cit. on p. 48).

[56] D. R. Lide, "Section 4, properties of the elements and inorganic compounds; heat capacity of the elements at 25 °c," in *CRC Handbook of Chemistry and Physics*, 84th ed. CRC Press, 2003, ISBN: 0-8493-0484-9 (cit. on p. 48).

[57] J. M. Bennett and E. J. Ashley, "Infrared reflectance and emittance of silver and gold evaporated in ultrahigh vacuum," *Applied Optics*, vol. 4, p. 221, 2 Feb. 1965, ISSN: 0003-6935. DOI: 10.1364/AO.4.000221 (cit. on p. 49).

[58] M. D. Kelzenberg *et al.*, "High-performance si microwire photovoltaics," *Energy and Environmental Science*, vol. 4, p. 866, 3 2011, ISSN: 1754-5692. DOI: 10.1039/c0ee00549e (cit. on p. 49).

[59] G. H. Kim, W. Ma, B. Yildiz, and C. V. Thompson, "Effect of annealing ambient on anisotropic retraction of film edges during solid-state dewetting of thin single crystal films," *Journal of Applied Physics*, vol. 120, 7 Aug. 2016, ISSN: 10897550. DOI: 10.1063/1.4961205 (cit. on pp. 49, 52).

[60] Y. N. Wen and J. M. Zhang, "Surface energy calculation of the fcc metals by using the maeam," *Solid State Communications*, vol. 144, pp. 163–167, 3-4 Oct. 2007, ISSN: 00381098. DOI: 10.1016/j.ssc.2007.07.012 (cit. on pp. 49, 52).

[61] O. Kurnosikov, L. P. Van, and J. Cousty, "High-temperature transformation of vicinal (0001) al 2 o 3-a surfaces: An afm study †," 2000, pp. 608–613 (cit. on p. 50).

[62] J. Wang, M. Li, and E. I. Altman, "Scanning tunneling microscopy study of au growth on ge(0 0 1): Bulk migration, self-organization, and clustering," *Surface Science*, vol. 596, pp. 126–143, 1-3 Dec. 2005, ISSN: 00396028. DOI: 10.1016/j.susc.2005.09.009 (cit. on p. 50).

[63] M. Binnewies, M. Finze, M. Jäckel, P. Schmidt, H. Willner, and G. Rayner-Canham, *Allgemeine und Anorganische Chemie*. Springer Berlin Heidelberg, 2016, ISBN: 978-3-662-45066-6. DOI: 10.1007/978-3-662-45067-3 (cit. on p. 51).

[64] C. Tang, M. J. Spencer, and A. S. Barnard, "Activity of zno polar surfaces: An insight from surface energies," *Physical Chemistry Chemical Physics*, vol. 16, pp. 22 139–22 144, 40 Sep. 2014, ISSN: 14639076. DOI: 10.1039/c4cp03221g (cit. on p. 51).

[65] S. Wei, Z. Wang, and Z. Yang, "First-principles studies on the au surfactant on polar zno surfaces," *Physics Letters, Section A: General, Atomic and Solid State Physics*, vol. 363, pp. 327–331, 4 Apr. 2007, ISSN: 03759601. DOI: 10.1016/j.physleta.2006.12.028 (cit. on pp. 51, 56).

[66] C. M. Müller and R. Spolenak, "Dewetting of au and aupt alloy films: A dewetting zone model," *Journal of Applied Physics*, vol. 113, p. 094 301, 9 Mar. 2013, ISSN: 0021-8979. DOI: 10.1063/1.4794028 (cit. on p. 51).

[67] A. Kosinova, O. Kovalenko, L. Klinger, and E. Rabkin, "Mechanisms of solid-state dewetting of thin au films in different annealing atmospheres," *Acta Materialia*, vol. 83, pp. 91–101, Jan. 2015, ISSN: 13596454. DOI: 10.1016/j.actamat.2014.09.049 (cit. on p. 52).

[68] E. F. Wassermann and K. Polacek, "Epitaxy of gold evaporated onto polar surfaces of zno at 20°k," *Applied Physics Letters*, vol. 16, pp. 259–260, 7 1970, ISSN: 00036951. DOI: 10.1063/1.1653186 (cit. on p. 52).

[69] E. Wassermann and K. Polacek, "Low temperature epitaxy of au on zno," *Surface Science*, vol. 28, pp. 77–83, 1 Nov. 1971, ISSN: 00396028. DOI: 10.1016/0039-6028(71)90086-0 (cit. on p. 52).

[70] R. Daudin, T. Nogaret, T. U. Schülli, N. Jakse, A. Pasturel, and G. Renaud, "Epitaxial orientation changes in a dewetting gold film on si(111)," *Physical Review B*, vol. 86, p. 094 103, 9 Sep. 2012, ISSN: 1098-0121. DOI: 10.1103/PhysRevB.86.094103 (cit. on p. 53).

[71] H. Iwanaga, A. Kunishige, and S. Takeuchi, "Anisotropic thermal expansion in wurtzite-type crystals," *Journal of Materials Science*, pp. 2451–2454, 35 2000. DOI: https://doi.org/10.1023/A:1004709500331 (cit. on p. 53).

[72] P. Herre *et al.*, "Rapid fabrication and interface structure of highly faceted epitaxial ni-au solid solution nanoparticles on sapphire," *Acta Materialia*, vol. 220, p. 117 318, Nov. 2021, ISSN: 13596454. DOI: 10.1016/j.actamat.2021.117318 (cit. on p. 56).

[73] M. Saito, "Hrtem investigations of structure and composition of polar pd/zno heterophase interfaces," Max-Planck-Institut für Metallforschung, 2005 (cit. on p. 56).

[74] C. V. Thompson, J. Floro, and H. I. Smith, "Epitaxial grain growth in thin metal films," *Journal of Applied Physics*, vol. 67, pp. 4099–4104, 9 1990, ISSN: 00218979. DOI: 10.1063/1.344969 (cit. on p. 58).

[75] F. Niekiel, S. M. Kraschewski, P. Schweizer, B. Butz, and E. Spiecker, "Texture evolution and microstructural changes during solid-state dewetting: A correlative study by complementary in situ tem techniques," *Acta Materialia*, vol. 115, pp. 230–241, Aug. 2016, ISSN: 13596454. DOI: 10.1016/j.actamat.2016.05.026 (cit. on p. 58).

[76] S. W. Hieke, B. Breitbach, G. Dehm, and C. Scheu, "Microstructural evolution and solid state dewetting of epitaxial al thin films on sapphire (alpha-al2o3)," *Acta Materialia*, vol. 133, pp. 356–366, Jul. 2017, ISSN: 13596454. DOI: 10.1016/j.actamat.2017.05.026 (cit. on p. 58).

[77] V. V. Bulatov, B. W. Reed, and M. Kumar, "Grain boundary energy function for fcc metals," *Acta Materialia*, vol. 65, pp. 161–175, Feb. 2014, ISSN: 13596454. DOI: 10.1016/j.actamat.2013.10.057 (cit. on p. 58).

[78] H. Nahor, Y. Kauffmann, S. Lazar, D. Shilo, and W. D. Kaplan, "Discerning interface atomistic structure by phase contrast in stem: The equilibrated ni-ysz interface," *Acta Materialia*, vol. 154, pp. 71–78, Aug. 2018, ISSN: 13596454. DOI: 10.1016/j.actamat.2018.05.011 (cit. on p. 59).

Appendix A

Lattice parameters from SAED

The lattice parameter for gold is calculated by measuring the g-vector of a lattice plane in the SAED image (Figure A.1), converting it into the reciprocal, which is the real space lattice spacing and then using Equation 3.3. The ZnO lattice parameter c is simply half the reciprocal distance of the g(0002) vector and a is determined from Equation 3.4 and the SAED image (Figure A.2) in the same way as Au.

Table A.1: Lattice parameters of Au and ZnO from the corresponding g vectors from SAED

Lattice constant	g vector	Measured distance
a_{Au}=3.93 Å	g(333)	13.23 $Å^{-1}$
a_{ZnO}=4.98 Å	g(0008)	12.91 $Å^{-1}$
c_{ZnO}=3.36 Å	g(2-420)	16.07 $Å^{-1}$

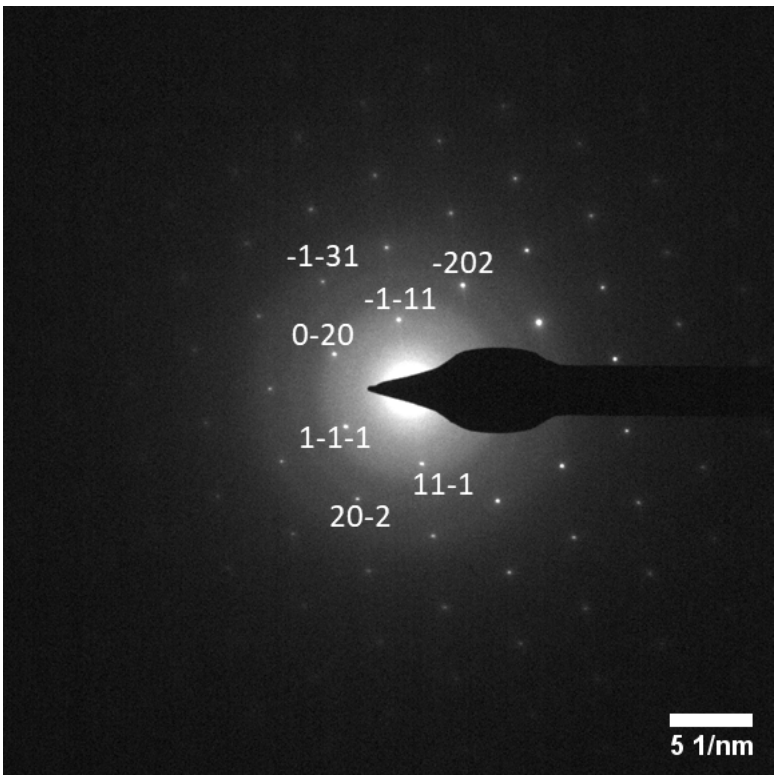

Figure A.1: SAED image of Au in the [110] zone axis

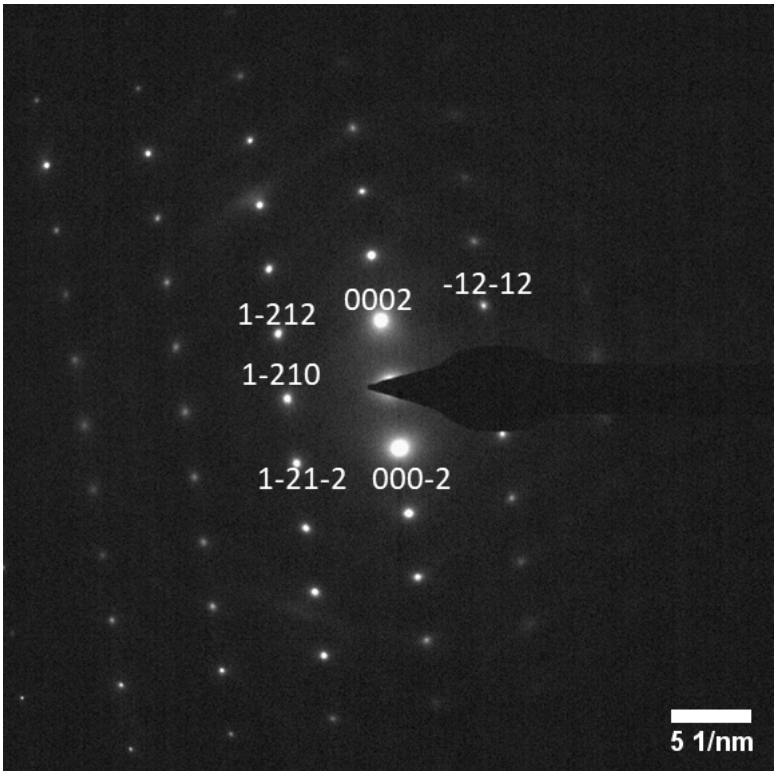

Figure A.2: SAED image of Au in the $[10\bar{1}0]$ zone axis

Appendix B

EDX of Au on ZnO

The HAADF and EDX maps show a sharp interface between Au and ZnO without signs of mixing. The carbon signal is increased on areas which where previously imaged due to carbon deposition and the hole in the right side of the image is likely caused by the FIB preparation.

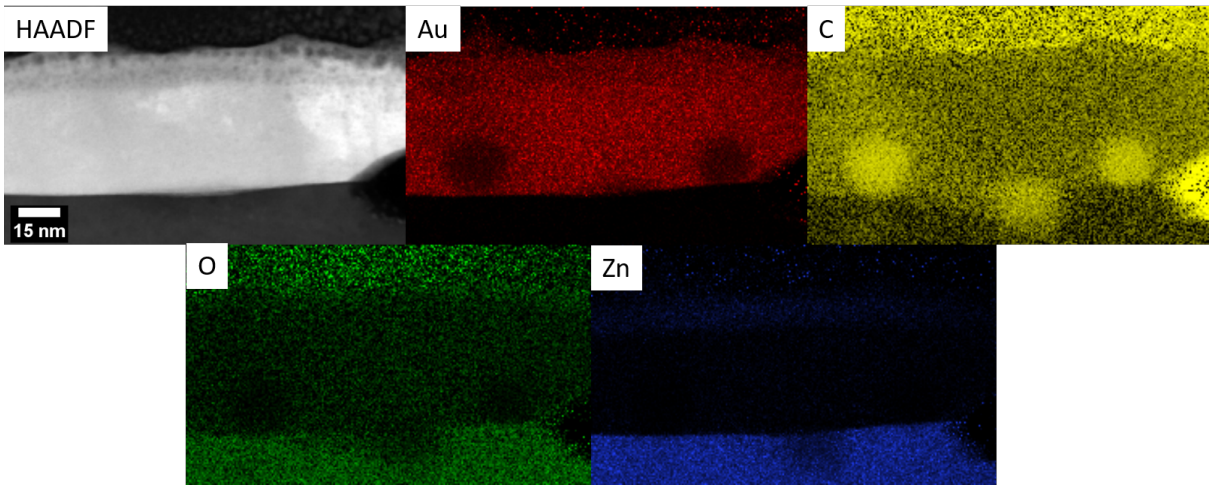

Figure B.1: TEM EDX of the cross-section of Au on O-ZnO, there is no mixing of Au and Zn detected the carbon deposits stem from earlier imaging

Appendix C

EBSD Pole figures

Scatter plot pole figures

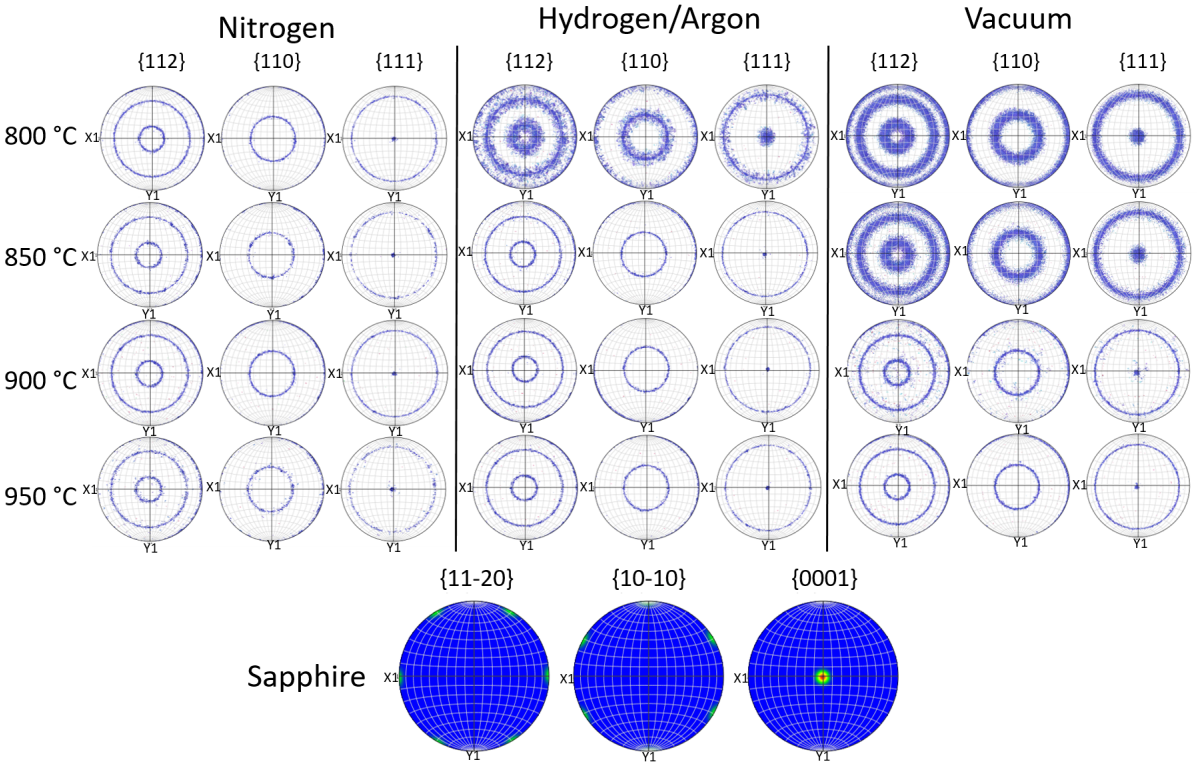

Figure C.1: Scatter plot pole figure of Au on sapphire annealed in different atmospheres

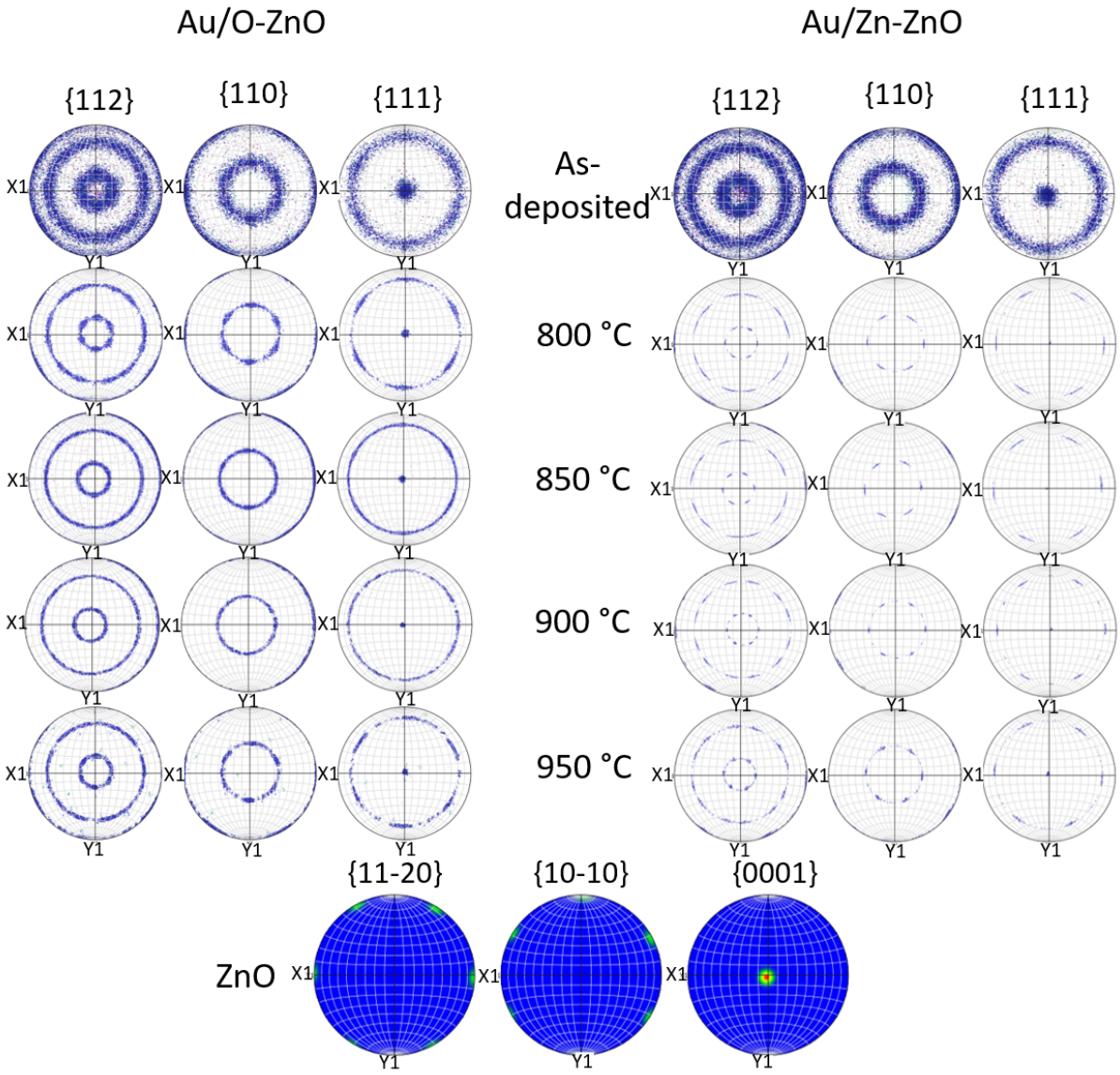

Figure C.2: Scatter plot pole figures of Au on O-ZnO and Zn-ZnO annealed in nitrogen for 30 seconds

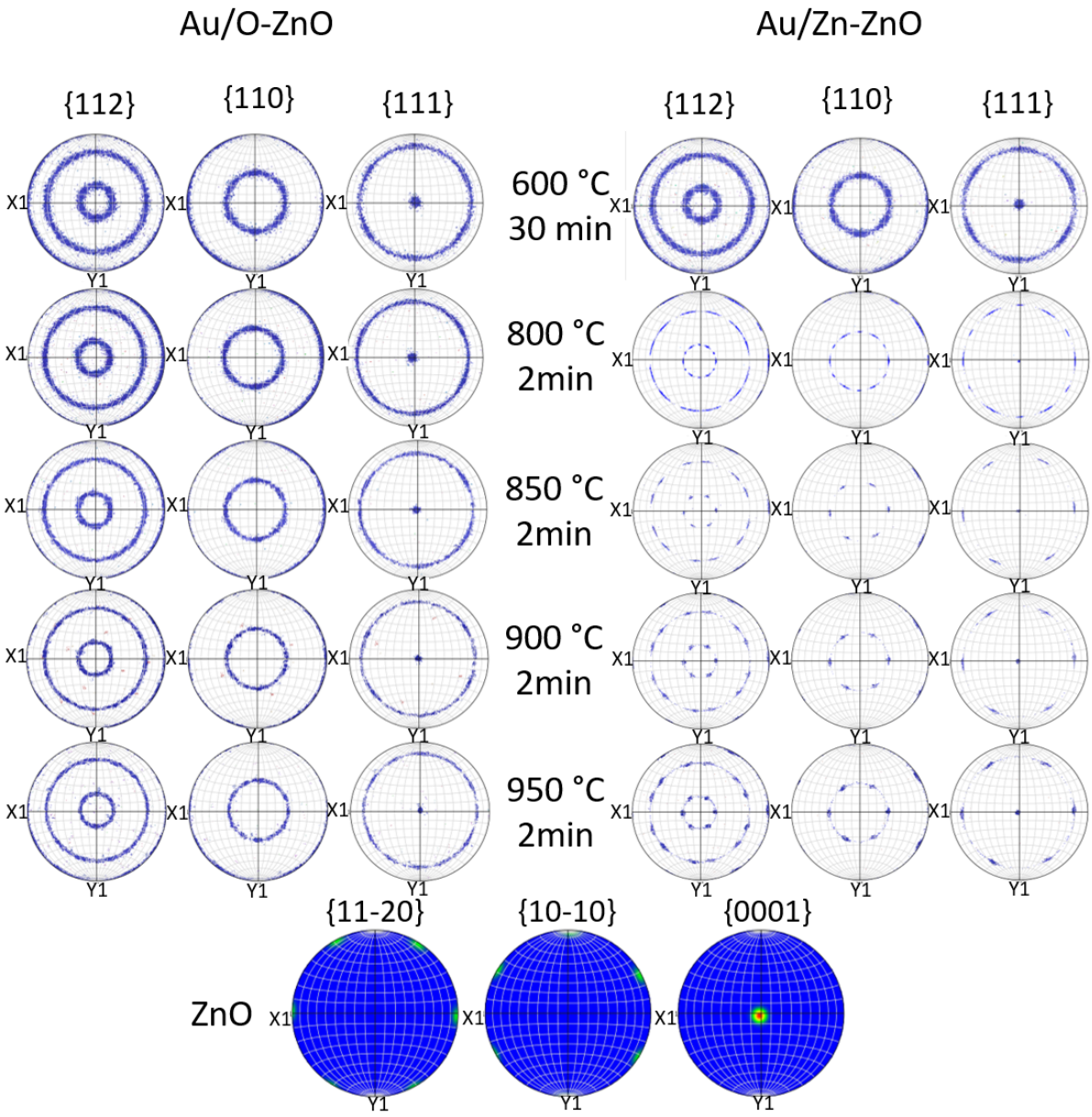

Figure C.3: Scatter plot pole figures of Au on O-ZnO and Zn-ZnO annealed in nitrogen for 2 minutes

Contour pole figure

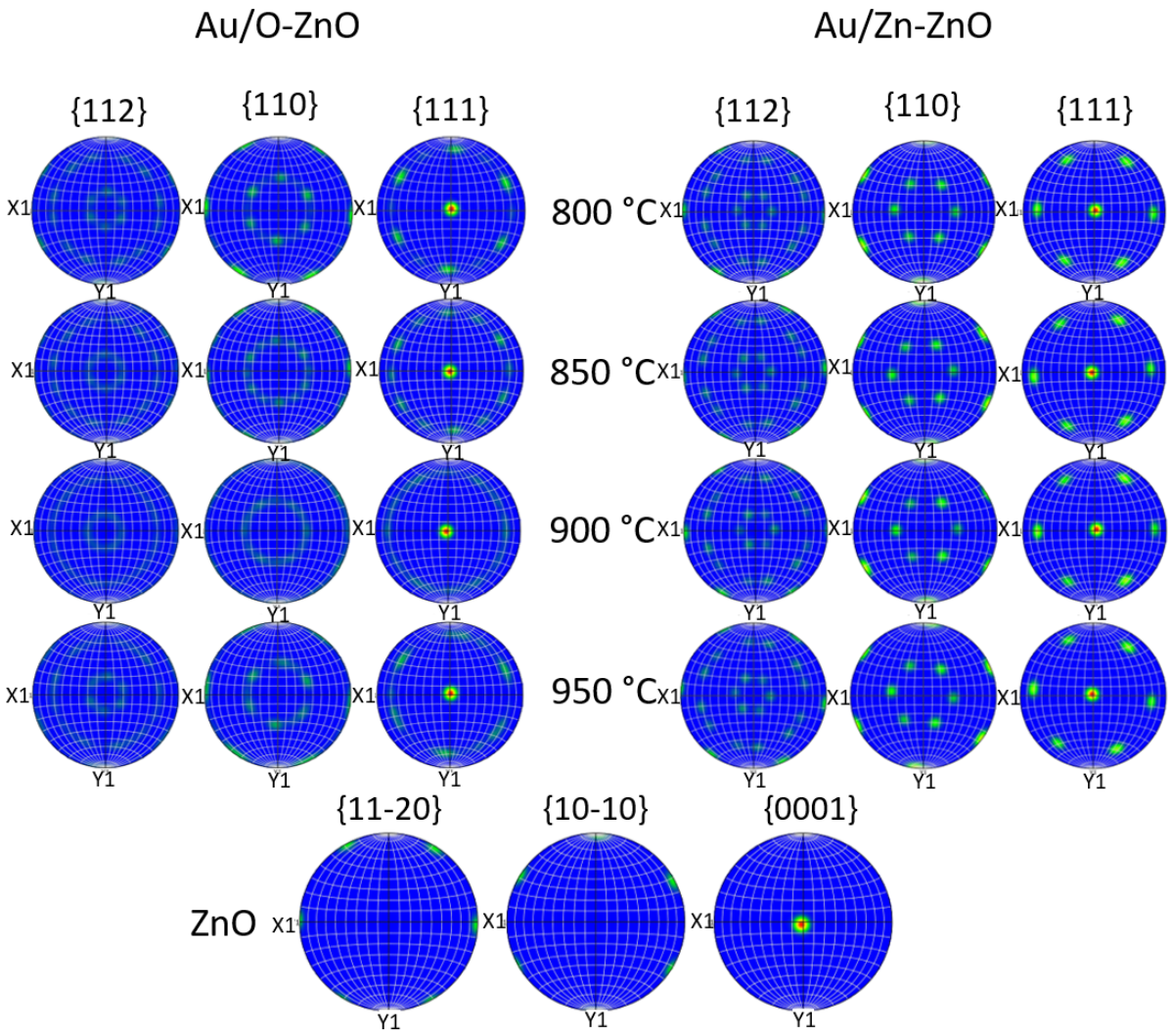

Figure C.4: Pole figures of Au on O-ZnO and Zn-ZnO annealed at temperatures from 800 °C to 950 °C for 30 seconds, all Au PF fit to the bottom ZnO PF

Eidesstatliche Erklärung

Ich versichere, dass ich die Arbeit ohne fremde Hilfe und ohne Benutzung anderer als der angegebenen Quellen angefertigt habe und dass die Arbeit in gleicher oder ähnlicher Form noch keiner anderen Prüfungsbehörde vorgelegen hat und von dieser als Teil einer Prüfungsleistung angenommen wurde. Alle Ausführungen, die wörtlich oder sinngemäß übernommen wurden, sind als solche gekennzeichnet.

_____ Erlangen, den 28. März 2022

Michael Landes